Star formation in the Auriga-California Giant Molecular Cloud and its circumstellar disk population

by

Hannah Broekhoven-Fiene
B.Sc., Queen's University, 2009
M.Sc., University of Victoria, 2011

A Dissertation Submitted in Partial Fulfillment of the
Requirements for the Degree of

DOCTOR OF PHILOSOPHY

in the Department of Physics & Astronomy

Star formation in the Auriga-California Giant Molecular Cloud and its circumstellar disk population

by

Hannah Broekhoven-Fiene
B.Sc., Queen's University, 2009
M.Sc., University of Victoria, 2011

Supervisory Committee

Dr. Brenda Matthews, Co-Supervisor
(Department of Physics & Astronomy)

Dr. Kim Venn, Co-Supervisor
(Department of Physics & Astronomy)

Dr. James Di Francesco, Departmental Member
(Department of Physics & Astronomy)

Dr. Dennis Hore, Outside Member
(Department of Chemistry)

Supervisory Committee

Dr. Brenda Matthews, Co-Supervisor
(Department of Physics & Astronomy)

Dr. Kim Venn, Co-Supervisor
(Department of Physics & Astronomy)

Dr. James Di Francesco, Departmental Member
(Department of Physics & Astronomy)

Dr. Dennis Hore, Outside Member
(Department of Chemistry)

ABSTRACT

This thesis presents a multiwavelength analysis, from the infrared to the microwave, of the young, forming stars in the Auriga-California Molecular Cloud and a first look at the disks they host and their potential for forming planetary systems. At the beginning of this thesis, Auriga-Cal had only recently been identified as one contiguous cloud with its distance placing it within the Gould Belt of nearby star-forming regions (Lada et al., 2009). This thesis presents the largest body of work to date on Auriga-Cal's star formation and disk population. Auriga-Cal is one of two nearby giant molecular clouds (GMCs) in the Gould Belt, the other being the Orion A molecular cloud. These two GMCs have similar mass ($\sim 10^5$ $M_\odot$), spatial scale ($\sim$ 80 pc), distance ($\sim$450 pc), and filamentary morphology, yet the two clouds present very different star formation qualities and quantities. Namely, Auriga-Cal is forming far fewer stars and does not exhibit the high-mass star formation seen in Orion A. In this thesis, I present a census of the star forming objects in the infrared with the *Spitzer Space Telescope* showing that Auriga-Cal contains at least 166

young stellar objects (YSOs), 15–20× fewer stars than Orion A, the majority of which are located in the cluster around LkHα 101, NGC 1529, and the filament extending from it. I find the submillimetre census with the James Clerk Maxwell Telescope, sensitive to the youngest objects, arrives at a similar result showing the disparity between the two clouds observed in the infrared continues to the submillimetre. Therefore the relative star formation rate between the two clouds has remained constant in recent times. The final chapter introduces the first study targeted at the disk population to measure the formation potential of planetary systems around the young stars in Auriga-Cal. The dust thermal emission at cm wavelengths is observed to measure the relative amounts of cm-sized grains, indicative of the grain growth processes that take place in disks and are necessary for planet formation. For a subsample of our targets, we are able to measure the spectral slope in the cm to confirm the thermal nature of the observed emission that we detect and characterize the signature of grain growth. The sensitivity of our observations probes masses greater than the minimum mass solar nebula (MMSN), the disk mass required to form the Solar System. We detect 19 disks, representing almost a third of our sample, comparable to the numbers of disks in other nearby star-forming regions with disks masses exceeding the MMSN, suggesting that the disk population in Auriga-Cal possesses similar planet formation potential as populations in other clouds. Confirmation of this result requires future observations with mm interferometry, the wavelength regime where the majority of statistics of disks has been measured.

Contents

List of Tables

List of Figures

Acknowledgements

There are many aspects to graduate school and finishing a degree. In the individual papers that are produced from the research described in this work, the funding bodies and resources are acknowledged. Here, I would like to acknowledge those who have been essential inspiration and support, regardless of whether or not they directly contributed to the research.

I would like to thank:

Brenda Matthews, for your mentorship, support, and encouragement. Thank you for being my advocate in countless ways related to the graduate school experience, going above and beyond support with my research.

Queen's University and the Marty-Royce-Bader selection committee, for funding my research and investing in me.

Hokiat Lim, for encouraging me to apply to graduate school and recommending UVic for an astronomy program. Our discussions helped me realize that it was within my grasp.

Carter William, Wilhelm David, Mason McKenzie, Levi Thomas, and Helena Maureen for the visits we share when opportunity allows and for brightening every day with the photos and videos your parents send. And to your parents, thank you for always providing a home and a haven for me.

Harjit, for being there over the years. I will miss our regular check-ins.

the post-doctoral ladies Rita Mann, Sam Lawler, Helen Kirk, and Michele Bannister for discussions, encouragement, and inspiration. You provide a powerful spectrum of young women in science.

Florian Glass, for your impeccable timing and sharing in the ups and downs of this degree.

João Shannon Sterrett, Susan Kim, and Karl Marx, for providing a happy and safe household.

Charli Sakari, for all your personal and professional support in times I felt neurotico, when things were chaotico. I'm so glad that we were more than just down-the-hall-mates and became friends almost automatico. I enjoy our time together a lot-ico.

my supervisory committee, for being a fantastic group that I am proud to have been directly included in the progress of my degree.

Vikes Recreation, in particular Andrew Pitre and Jason Wright, for supporting the start-up and running of my classes and workshops over the years. This opportunity has helped me contribute to the UVic community in diverse ways and grow as a Martial Artist. And thank you to the students, particularly those whose involvement spanned many semesters, for their active participation and enthusiasm.

the Stuff Around Stars (SAS) Club, for the interesting discussions of their own work, trials, and presentations of articles in our diverse fields of research.

James Di Francesco, Helen Kirk, Rosemary Pike, Wes Fraser, Konstantin Fedotov, Charli Sakari, Chelsea Spengler, Trystyn Berg and many others for drives to and from the observatory.

Susan Gnucci, for keeping the Physics & Astronomy department running.

Jillian Scudder, Lisa Glass, Andy Pon, Konstantin Fedotov, for being extra special, long standing office mates and providing instantaneous sanity checks.

Sasha Kovalchuk and sofija vrbaški, for being an inspiration through your endless efforts to improve the lives of the people in the communities around you, and for being a part of the positive change in my life.

and to the many others that have constructively contributed to my education and life in Victoria.

Dedication

To Eric and Grace,

thank you for teaching me how to take care of myself – a skill I had overlooked and will now take with me wherever I go.

Co-Authorship

The results in this thesis is the yield of a large collaborative effort. Modern astronomy is performed in this way with researchers collaborating to obtain, process, and analyze scientific data, regardless of who has taken the lead on a specific aspect of the research.

The research presented here is that that I have taken the lead on as part of larger collaborations. For each chapter, I have listed the contributing authors to the work. These are people who were involved in any or many stages of the project, such as the original proposal and acquisition of data, processing of the raw data, developing analysis routines, performing some analysis directly, or contributing to developing the manuscript.

In the list of co-authors and co-investigators, I have highlighted the names of the people who I have worked directly with on the project. I have also joined these projects at various levels and stages.

Chapter 1

Introduction

Planets form in disks of gas and dust around young stars. An early indication of this setting was that the Solar System itself is arranged in a disk-like structure. The planets, the Asteroid Belt, and the Kuiper Belt all more or less lie in the plane of the Solar System, the Ecliptic, within $\sim 30^{\circ}$. Observations of massive disks around young stars provide further evidence of the environment and structure needed to form the disk-like geometry of our planetary system. These planet-forming disks are dubbed protoplanetary disks (PPDs).

It is an exciting time to study planet formation and protoplanetary disks. The field of extrasolar planets[1] (or exoplanets) has exploded with over 2000 planets detected around other stars.[2] The Kepler mission has added hundreds to the ranks and thousands more candidates for future study. These discoveries highlight the wide variety of planetary systems that are formed in PPDs giving planet formation theorists much to explain. Furthermore, planetary systems can host belts of dust called debris disks, so named because the observed dust is produced in collisions of asteroid and planetesimal bodies. Both planets and debris disks must be considered to explain the dynamics of the bodies in a planetary system. Observed planetary systems provide examples of a variety of outcomes of planet formation processes.

Molecular clouds are the sites of star formation. Stars form when clumps of material in this cloud collapse. Molecular clouds provide an opportunity to study a population of YSOs with a given age, environment, and composition. Studying YSOs in different molecular clouds is a means of comparing populations with potentially shared characteristics, allowing the impact of environment to be examined.

[1] Planets outside the Solar System.

[2] An up-to-date database of detected exoplanets and their properties is at exoplanet.eu.

Within our Galaxy, the closest YSO populations are in the Gould Belt of star-forming regions. These present the optimal targets for understanding the current star formation in the Galaxy.[3] Consequently, the clouds within the Gould Belt are the most thoroughly studied star-forming regions in the Galaxy and present a variety of star formation qualities. The clouds within the Gould Belt have different relative ages, physical conditions, and YSO populations.

The Auriga-California Molecular Cloud (AMC) is a star-forming region within the Gould Belt. It was only recently recognized that its previously studied regions (Lynds, 1962) are indeed all part of one contiguous giant cloud (Lada et al., 2009). Consequently, the AMC is relatively unstudied in comparison to its other Gould Belt companions.

The AMC is one of two nearby (within 500 pc) giant molecular clouds (GMCs), the other being the Orion A Molecular Cloud (OMC), also in the Gould Belt. The two GMCs have a similar mass, size and distance but the AMC is forming 10-20 times fewer stars than the OMC (Broekhoven-Fiene et al. 2014: Chapter 2). Furthermore, the AMC only has one B-star, LkHα 101 (Herbig et al., 2004), whereas the OMC contains dozens of O and B stars[4]. The majority of YSOs surrounding LkHα 101 are late-type stars (K5 and later; Wolk et al. 2010). This highlights the variation in star formation potential within GMCs. The star formation in the AMC more closely resembles that in Taurus and Ophiuchus, which also show a relative paucity of high mass stars. Studies of the AMC are of particular importance because GMCs like it at further distances would be difficult to detect or even identify as GMCs due to the relatively limited star formation.

Both the AMC and the OMC have total masses of $\sim 10^5$ $M_\odot$, however, the AMC has $\sim$10 times less mass at higher ($A_V > 1$) extinction, a proxy for density, than the OMC (Lada et al., 2009). This difference in the mass of high density material between these two clouds is considered to be the reason for the difference in star formation. Despite their differences in star formation density, the AMC and the OMC have morphologically similar features, as shown in Figure 1.1. They both have an overall filamentary shape with the richest area of star formation on one extremity that hosts the most massive stars. In the AMC, the densest region of star formation is around the B star LkHα 101. In the OMC, it coincides with the O-star θ^1 Ori C.

[3]The proper noun Galaxy refers to our own galaxy, the Milky Way.

[4]Stars are classified according to their spectral type. O and B stars are the most massive and most luminous spectral type. (The spectral types in order of most to least luminous are O, B, A, F, G, K, and M)

There are some outstanding questions regarding the star and planet formation in the AMC because it is an atypical example of star formation relative to the Gould Belt clouds that have been well-studied over the last few decades. This thesis aims to address these and examine the star and planet formation potential in the AMC. The star formation potential is characterized by creating a census of star-forming objects across multiple wavelength regimes. I study the planet formation potential of the AMC by targeting the brightest star-forming objects, measuring the amount of material available for planet formation in their circumstellar disks, and looking for evidence of the earliest stages of planet formation.

In this first chapter, I give an overview of the stages of star formation and how protoplanetary disks are identified. I then discuss protoplanetary disks in more detail and the observations used to measure their properties. In particular, I assess how they reveal the amount of material available for planet formation and the evidence for growth of pebble-sized objects – the building blocks of planetary embryos.

1.1 Star formation

1.1.1 Stages of star formation

The protoplanetary disk phase of a star's lifetime is one of the final stages of star formation. It is therefore natural to use star formation as a starting point to provide the context of planet formation and describe the environment within and surrounding the protoplanetary disk.

Figure 1.2 shows a cartoon depicting each stage of star formation along with a diagram of the typical spectral energy distribution (SED[5]) that is associated with it (Shu et al. 1987). The formation of a star is initiated when a clump of the molecular cloud collapses under its own gravity to form a central object. To conserve angular momentum, an accretion disk forms to transport material from the surrounding envelope of material onto this young stellar object (YSO). At this stage, Stage I, the circumstellar material, located both in the disk and the envelope, is much brighter than the central object and dominates the observed emission. This stage is also referred to as an 'active disk' due to the high accretion rate of material onto the star. The spherical circumstellar envelope, the reservoir of gas and dust from which the accretion disk draws its material, is eroded and dissipates as stellar winds and outflows clear away

[5]This is the measurement of an object's flux across multiple wavelengths.

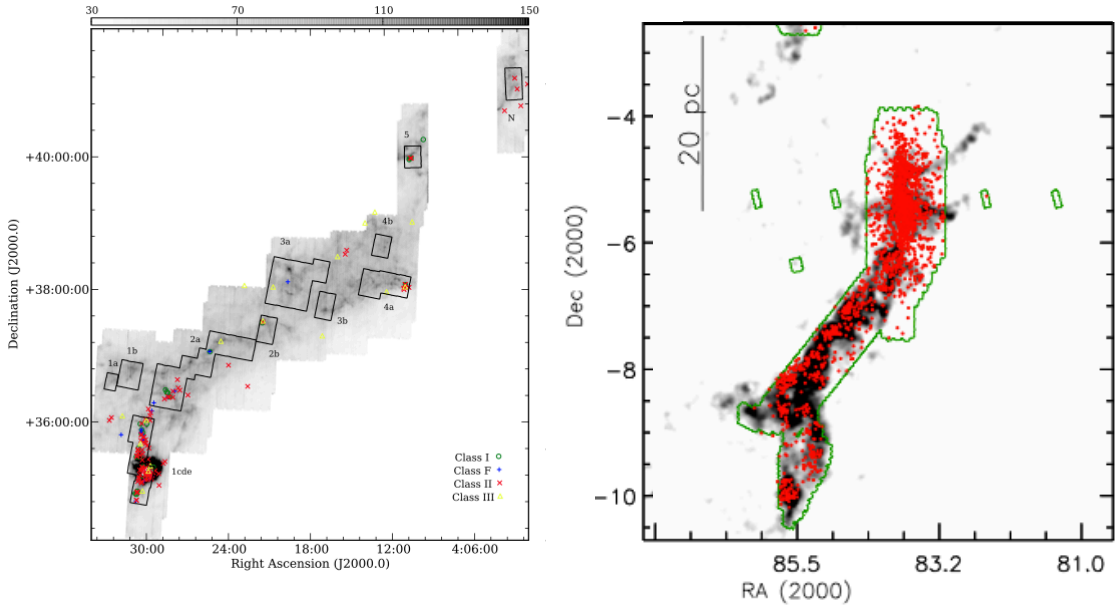

Figure 1.1 The AMC (left, Broekhoven-Fiene et al. 2014) and OMC (right, adapted from Megeath et al. 2012). The multicolour markers show the location of YSOs in each of the clouds. LkHα 101 is located in the lower (southern) end of the filament as shown. The Orion Nebula Cluster, host to θ^1 Ori C, is at the upper end of the OMC filament as shown. These are the richest areas of star formation. (In the left panel, the black boxes outline the area observed with *Spitzer*/IRAC and the greyscale image is the area observed with *Spitzer*/MIPS. In the right panel, the green line traces the field observed by IRAC and MIPS with *Spitzer*.)

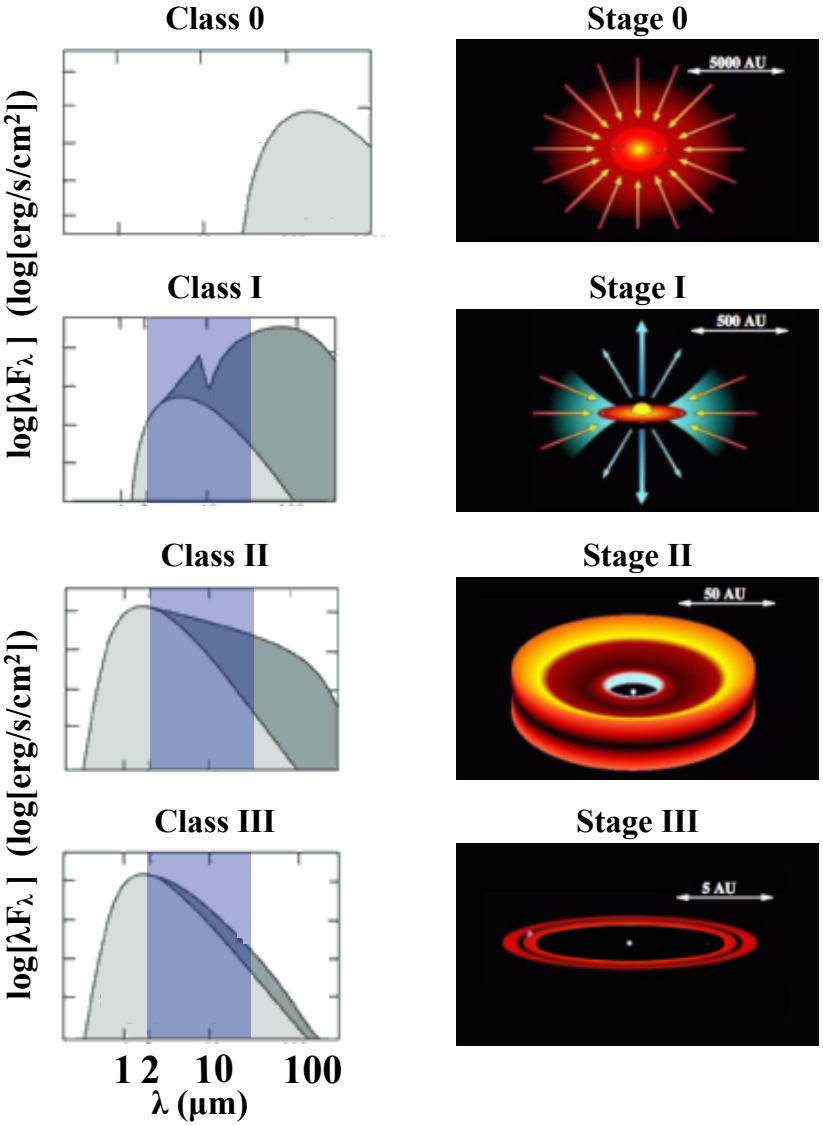

Figure 1.2 *Left panels* show the SED Class associated with each Stage. (Values of the observed flux, λF_λ, are not shown because they scale with the distance to the object.) The light grey area shows the emission that originates from the stellar object and the dark grey shows the emission originating from the circumstellar material. The shaded purple areas highlight the wavelength region used to classify the SEDs of YSOs based on their slope. (*Image credit: André 1994.*) *Right panels* show cartoons of the different Stages of star formation (from top to bottom): the initial collapse of clump of cloud material (Stage 0: $<$ 30 000 yr); the protostellar disk phase with surrounding circumstellar envelope (Stage I: $\sim$ 200 000 yr); the protoplanetary disk phase (Stage II: $\sim$ 1 000 000 yr); and the final stage which may have a remant disk (Stage III: $\sim$ 10 000 000 yr). (*Image credit: Isella 2006.)*

material. The circumstellar disk remains and eventually the accretion onto the star slows. It is this stage, Stage II (also known as a 'passive disk'), that we refer to as the protoplanetary disk phase. There is no remnant envelope and only mild accretion of mass onto the star. During this time, planet formation processes occur within the disk, forming rocks, asteroids/planetesimals, and planets. Later, the material in the disk is cleared away and the formed planetary system is revealed. There may be a remnant disk at this stage, Stage III, and objects at this Stage are typically more difficult to detect given the relatively lower levels of dust around the young star. The physical extent of the material around the YSO depends on the physical Stage it is in. The outer envelope has a size of ∼10,000 AU (22″ at Auriga-Cal's distance) and the protoplanetary disks have sizes more typically of ∼100 AU (0.22″ at Auriga-Cal's distance). Therefore younger objects with an envelope will have much larger sizes than older ones with only a disk.

1.1.2 Identifying protoplanetary disk hosts

YSOs are typically identified and classified by analyzing their SEDs. This process is especially efficient when dealing with a large population. The YSOs are classified according to the slope of their SEDs in the 2 μm to 24 μm infrared range (highlighted in the example SEDs of Figure 1.2) which depends on the evolutionary stage of the object. This slope is positive in the earlier stages where the circumstellar material dominates the emission and decreases as the object evolves and the amounts of circumstellar dust decline. In the protoplanetary disk phase, the SED decreases towards longer wavelengths. Eventually in the final phase, when very little disk remains, the slope approaches that expected for a stellar photosphere. This evolution in the slope of the emission for a given object is the basis for the Lada classification system (Lada, 1987) for YSOs, later refined by Greene et al. (1994).

This infrared spectral slope, $\alpha_{\rm IR}$, determines the spectral Class of the object where $\alpha_{\rm IR} \equiv {\rm d}\log(\lambda F_\lambda)/{\rm d}\log(\lambda)$ between 2 μm and 24 μm. The Classes are divided as follows

Class I: $\alpha_{\rm IR} \leqslant 0.3$;

Class F: -0.3 $\leqslant \alpha_{\rm IR} <$ 0.3;

Class II: -1.6 $\leqslant \alpha_{\rm IR} <$ -0.3;

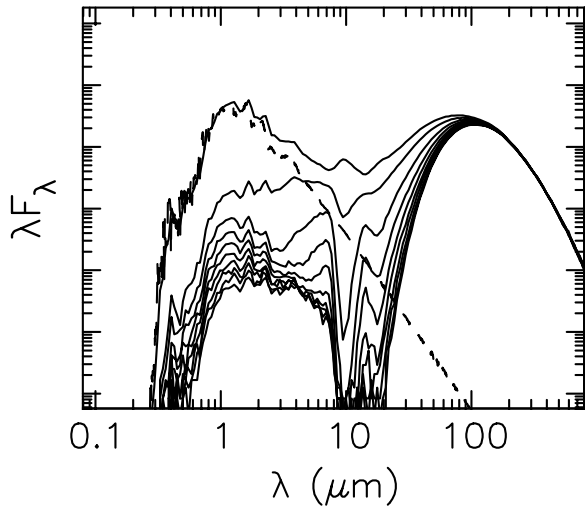

Figure 1.3 A figure by Robitaille et al. (2006) of a ∼0.2 $M_\odot$ Stage I YSO showing the observed SED for different viewing angles. The brightest to faintest SED curves correspond to inclination angles from pole-on to edge-on. (The disk plane is perpendicular to the poles.) The majority of the curves result in a Class I SED, however, the most inclined geometry (pole-on) results in a Class II SED.

Class III: $\alpha_{\rm IR} <$ -1.6.

Class I, II, and III are associated with Stage I, II, and III described in § 1.1.1 and shown in Figure 1.2. Class F denotes a 'flat spectrum' source, so named according to their $\alpha_{IR} \sim 0$. These sources are associated with the transition between Class I and Class II objects. Note that although the Class of an object suggests the actual physical stage of the object, confirming the Stage requires other diagnostics such as resolved imaging, measurements of mass, and dynamical features such as outflows. The observed SED of an object in a given Stage is also dependent on the viewing geometry. As an example, consider Figure 1.3 which shows the observed SED of a Stage I object for various inclinations. Although the majority of inclinations of a Stage I object will produce a Class I SED, a Stage I object viewed pole-on has a Class II SED because it is viewed through the opening of the circumstellar envelope (at the pole) and the central object and hotter dust are viewed directly, increasing the flux observed at shorter wavelengths. This complication, however, only affects a small fraction of the total sources and so although the Class does not determine the physical stage, the majority of objects of a certain Class are in the associated Stage. (See discussion in Evans et al. 2009.)

In this thesis, I aim to study the protoplanetary disks in the Auriga-California

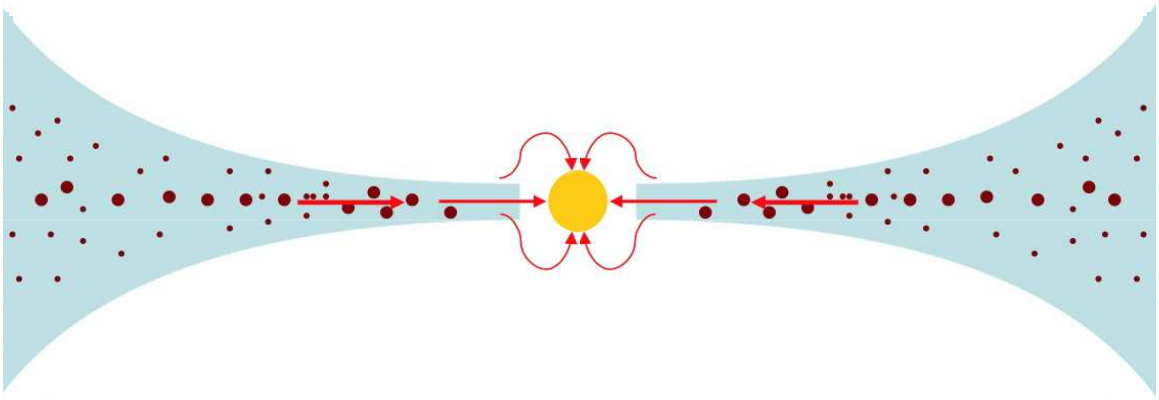

Figure 1.4 Figure adapted from Williams & Cieza 2011 showing the structure of a settled protoplanetary disk. The blue area represents the gas in the disk and the brown circles represent dust grains, scaled according to their relative sizes. Material is still being accreted on to the star (yellow circle) as shown by the arrows. The larger dust grains settle to the midplane of the disk resulting in a stratified disk.

Molecular Cloud. My target sample is drawn from the Class II objects identified in via their infrared characteristics. These objects represent the candidate protoplanetary disk hosts.

1.2 Protoplanetary disk structure and composition

Protoplanetary disks, like the surrounding molecular cloud, are composed of gas and dust. The gas compromises most of the mass with only 1% of the mass in dust grains. Observations of each of these materials can be used to target different aspects of the disk. Molecular line observations of the gas are very beneficial for tracing dynamics within the disk. The dust emits thermal radiation and therefore can be used to trace material with different temperatures within the disk.

There is a lot of material in the disk in a range of locations. This variety sets the stage for the distribution of temperature, velocities, and material within the disk. This thesis is based on continuum observations of the dust, and so I will focus on the dust's structure. Protoplanetary disks have a flared geometry (Figure 1.4) and so the various regions within the disk must be considered. The upper layers of the disk, the parts mostly irradiated by the star, have a different environment from the midplane of the disk. Furthermore, there is a distribution in sizes of dust grains. Larger dust

grains effectively sink to the midplane of the disk. This process is referred to as dust settling and results in a stratified disk.

1.3 Thermal emission of dust

Continuum observations at infrared (2 μm – 250 μm), submm (250 μm – 1 mm), and radio (> cm) wavelengths target the thermal emission of the circumstellar dust. Incident stellar radiation heats the dust which then emits thermal radiation according to its temperature, T_d, and given by the Planck function:

$$B_\nu(T_d) = \frac{2h\nu^3}{c^2} \frac{1}{e^{\frac{h\nu}{k_B T_d}} - 1} \tag{1.1}$$

where T_d is the temperature of the dust, h is the Planck constant, ν is the frequency of the observations, c is the speed of light in a vacuum, and k_B is the Boltzmann constant.

The temperature of the dust determines its emission. The observed flux of the dust, F_ν, is given by

$$F_\nu \approx \kappa_\nu M_d B_\nu(T_d) d^{-2} \tag{1.2}$$

where κ_ν is the opacity of the dust (the absorption cross-section per unit mass), M_d, is the mass of the dust, and d is the distance to the source from the Sun.

Dust exists at range of locations throughout the disk in terms of both its distance from the star and its height above the midplane (see § 1.2). This spatial distribution gives rise to a distribution of dust temperatures. Figure 1.5 shows a figure by Dullemond et al. (2007) showing how the temperature of dust depends on its physical location within the disk. The hottest dust temperatures arise from dust closest to the star at the inner radius of the disk. The surface layers of the flared disk are warmed by the star and effectively shield the cool midplane from stellar radiation. Observations at a given wavelength are therefore sensitive to a given temperature, and can target a different dust population.

1.3.1 Disk masses

To relate the observed flux from thermal dust emission to the total amount of material in a disk, one must consider the optical depth of the emission which characterizes the cross-sectional area of the particles observed and also varies with wavelength regime.

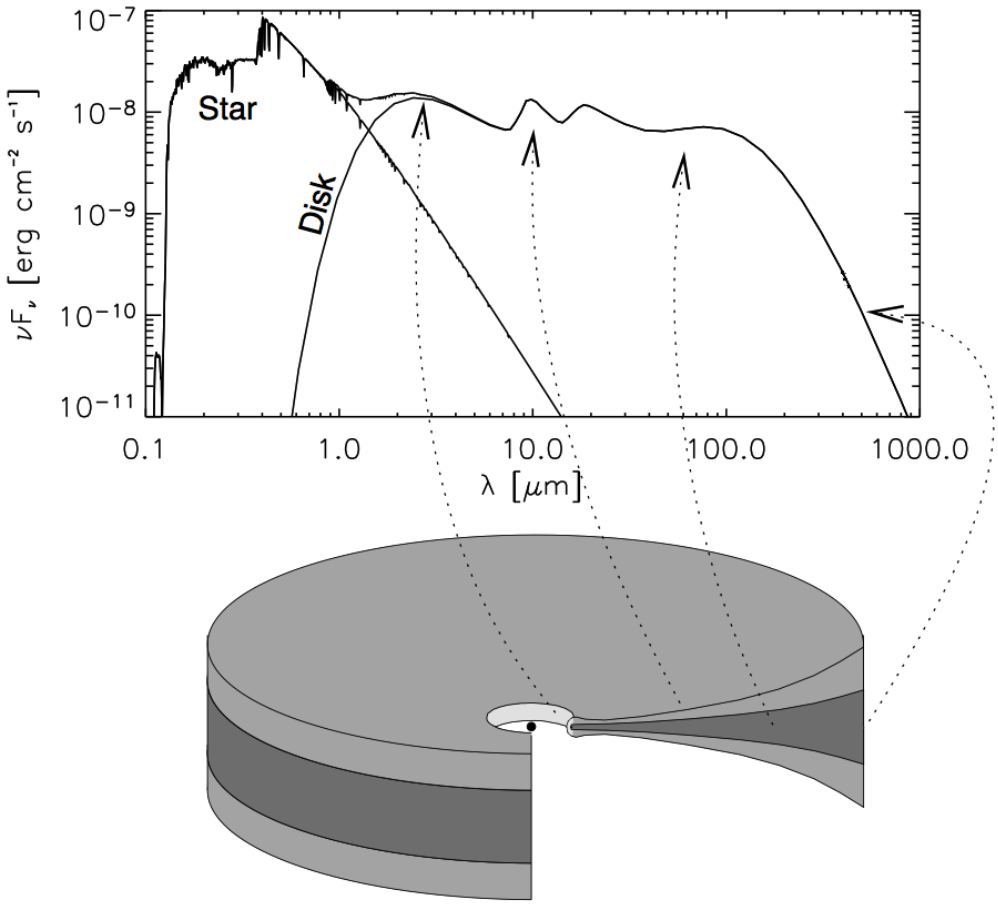

Figure 1.5 An example SED of a protoplanetary disk from Dullemond et al. (2007). The plot distinguishes between the observed emission that originates from the star and from the disk. The 'excess' over stellar emission is attributed to the dust. The excess at the shortest wavelengths (near infrared) traces the hottest dust temperatures and therefore the material closest to the star at the disk's inner radius. The mid-infrared excess traces the warm dust in the upper layers of the disk and the excess at submm (and longer) wavelengths corresponds to the coolest dust temperatures found in the midplane of the disk.

An object is said to be optically thin, for example, when we can "see" all the particles, i.e., the cross-sectional area of individual particles coupled with the total number of particles distributed throughout the volume does not produce an overlap of particles as seen by the observer. If an object is optically thick, this means only the emission from the particles closest to the surface is observed and particles deeper in the volume are invisible.

At submm and longer wavelengths, we enter the regime sensitive to the larger dust grains which have settled to the cooler midplane of the disk. These dust grains have a higher ratio of mass to surface area per grain and also cover a lower total surface area in the disk than smaller grains do. That is, more mass is locked up in the larger grains and the submm observations are optically thin. For this reason, in this thesis I use long wavelength (submm/mm/cm) observations of disks to sample the optically thin, cool dust in the midplane that is more sensitive to the total dust mass in the system. Emission observed at shorter wavelengths, such as in the infrared, is optically thick and therefore only carries information from the upper layers and inner edge of the disk.

To estimate the total disk mass (recall that the disk is mostly gas), a standard opacity, κ_ν, is assumed that includes an assumed gas-to-dust mass ratio of 100:1. This ratio is adopted from measurements of the total gas mass and total dust mass in the interstellar medium. In protoplanetary disks, both the gaseous component and the dust components can be observed but the total gas mass is difficult to measure. Consequently, the standard approach is to assume the gas-to-dust mass ratio measured from the interstellar medium. This assumption no doubt has its flaws but it provides a standard value to use and allows for a consistent comparison between measurements. Efforts to measure the gas-to-dust mass ratio in protoplanetary disks (e.g., Williams & Best 2014) continue in the meantime.

Rearranging Equation 1.2, the disk mass is measured using (e.g., Beckwith et al., 1990)

$$M_{disk} = \frac{F_{dust} d^2}{\kappa_\nu B_\nu(T)}. \tag{1.3}$$

(Note that the equation is for the total disk mass, M_{disk}, rather than the dust mass, M_d, used in Equation 1.2.)

The total disk mass characterizes the planet formation potential of the system because it indicates how much material is available for the process. For example, the minimum mass solar nebula (MMSN: 0.01 $M_\odot$) is the the minimum amount of

material needed to form the Solar System. It is common to compare disk masses to this value since it immediately puts the disk in the context of the type of planetary system that can form.

Measuring the distribution of disk masses is a straightforward way to compare populations of protoplanetary disks and determine the influence of high-mass, luminous stars, such as LkHα 101, on disk evolution. One aim of this thesis is to investigate such effects by comparing disks within and beyond the environment of LkHα 101 to determine differences. For example, θ^1 Ori C, an O-star in the OMC, has been shown to truncate the disk mass distribution in its vicinity (Mann & Williams, 2009b). Measuring the disk mass distribution for the AMC will be directly comparable to other clouds as this comparison has also been done for Taurus (Andrews & Williams, 2005), ρ Ophiuchus (Andrews & Williams, 2007), and Orion (Mann & Williams, 2010).

1.3.2 Grain growth

Observations at submm and longer wavelengths of the optically thin emission originating from the midplane of the disk are sensitive to the grain size distribution as well as the total dust mass. We revisit Equation 1.2 in the context of the long wavelength observations. At submm wavelengths, we make the Rayleigh approximation to the Planck function to show

$$F_\nu \approx \frac{2k}{c^2}\nu^2\kappa_\nu(\nu)\frac{M_d T_d}{d^2}. \tag{1.4}$$

The opacity itself is a function of frequency and described by $\kappa_\nu \propto \nu^2$. We see from this and Equation 1.4 that $F_\nu \propto \nu^2\nu^\beta \propto \nu^\alpha$, where $\alpha = 2+\beta$. Therefore by measuring the shape of the SED, one can determine α, and consequently β.

Observations of dust grains in the interstellar medium (ISM) suggest $\beta_{\rm ISM} \approx 1.7$ (e.g., Goldsmith et al., 1997; Hunter, 1998; Friesen et al., 2005). Much lower values of β, such as ≈ 1 or even ≈ 0.5, are measured in PPDs (Beckwith & Sargent, 1991; Calvet et al., 2002; Testi et al., 2003; Natta et al., 2004). This variation suggested an evolution in the value of β from when the dust grains are in the greater cloud to when they are in PPDs.

The interpretation for the evolution in β is the evolution in dust grain sizes. Although the opacity is a complex function of both composition and dust grain size distribution, to achieve β values of ~ 1 and less at submm wavelengths requires an increase in the maximum grain size, $a_{\rm max}$, to at least mm/cm sizes (Draine, 2006). Such shallow spectral slopes at an observed wavelength, λ, require $a_{\rm max} \gtrsim 3\lambda$. In

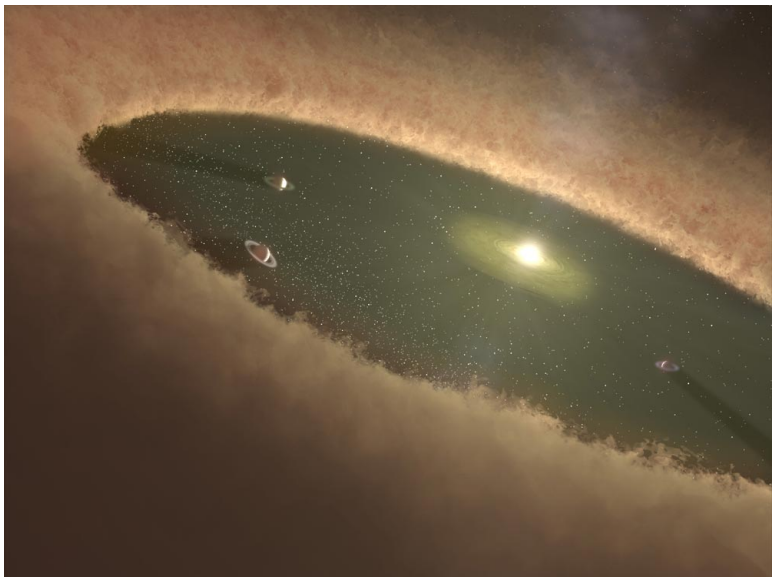

Figure 1.6 An artist's impression of a transition disk. There is an inner hole in the disk which contains newly formed planets but a substantial disk in the outer regions still remains. The material is in the process of being cleared from the inside out.*Image credit: NASA/JPL-Caltech/T. Pyle (SSC)*

this way, observations at a given wavelength probe the population of dust grains of comparable size to λ. Therefore, the evolution in β at submm/mm wavelengths measured from ISM grains to PPD grains is attributed to the growth of dust grains from submicron sizes to mm/cm sizes.

The formation of larger dust grains is one of the earliest stages of planet formation (e.g., Pollack et al., 1996). It precedes the growth to larger bodies to eventually form asteroids/planetesimals, terrestrial planets, and the cores of gas giant planets. The opacity dependance on dust grain size is also applicable to tracing the locations of different dust populations within the disk. Determining the evolution of dust grains in the disk is intimately connected to understanding the evolution of the disk itself and the physical conditions necessary for further growth.

1.4 Disk lifetimes and transition disks

Disk lifetimes set a time limit on the planet formation processes in a disk before the bulk of the material is cleared out. The median disk lifetime is found to be 2-3 Myr, with a maximum age of 10 Myr (e.g., Evans et al., 2009). As they summarize, this can be measured from the infrared excess incidence (indicating a circumstellar

disk) around young stars with ages determined from Hertzprung-Russell diagrams. Such an analysis requires young stars in the later stages of star formation when their photospheres are not completely obscured by dust. This evaluation results in a measurement of the half-life of the Class II lifetime. The relative lifetimes of the other classes is determined from the ratios of objects in each class assuming a constant star formation rate over recent history (the Class II lifetime).

One signature that a disk is in transition between Stage II and Stage III is a deficit of material close to the star with a substantial disk remaining in outer regions (Figure 1.6). Such disks, called 'transition disks', are identified by their SED (e.g., Strom et al. 1989; Brown et al. 2007; Cieza et al. 2012) or by directly imaging a gap in the disk close to the star (e.g., Hughes et al. 2010; Andrews et al. 2011). Once a hole is formed in the disk, this halts the accretion and the disk is eroded from the inside out. There are several mechanisms which have been suggested to produce the initial inner hole in the disk, such as photoevaporation from stellar radiation (Alexander et al., 2006), agglomeration of dust grains (Cieza et al., 2010; Sicilia-Aguilar et al., 2010), or the formation of a planet (Artymowicz & Lubow, 1994).

Transition disks mark the end of the protoplanetary disk phase and therefore are important targets to understand the final conditions and mechanisms within the disk. They are also interesting targets in which to search for newly formed planets, especially in disks found to have a inner holes with sharp edges.

1.5 Facilities and wavelength regimes observed

Recent instrumental advances have provided stunning resolved images of PPDs, which has been heretofore difficult given the relatively small size scales in the disks, their distances, and the long wavelengths required for observations.[6] Radio interferometers are particularly important to achieve high resolution observations at the sensitivity required for distant objects. Most notably, the Atacama Large Millimeter/Submillimeter Array (ALMA) and the Janksy Very Large Array (VLA) have reached the capabilities required to resolve the nearest PPDs in the last couple of years. ALMA, recently constructed in Chile, is the first billion-dollar ground based observatory. Early science results have already demonstrated ALMA's leading capabilities. The VLA was recent upgraded and has 10× more sensitivity than before.

[6]For a given telescope of fixed size, resolution decreases as wavelength increases.

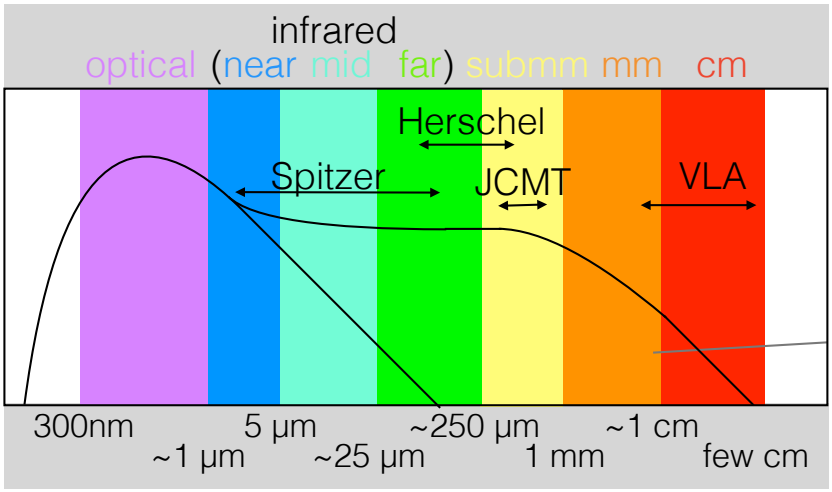

Figure 1.7 A cartoon SED of a protoplanetary disk summarizing the different pertinent wavelength regimes (top axis) and their wavelength limits (bottom axis). The black curves trace the emission from the star and the disk. The grey line represents non-thermal free-free emission from ionized protostellar winds (not disks) observed at cm wavelengths. The approximate wavelength ranges of the observatories used in this thesis are shown.

These observatories are particularly important as they have the sensitivities required to study the large sample of disks targeted in this thesis.

In this thesis, I use data across multiple wavelength regimes and from various observatories. Figure 1.7 summarizes these different regimes, their wavelength ranges, and where the facilities discussed in this thesis observe. I summarize here the facilities and their main observational qualities as a reference for comparing the observations discussed in the different chapters.

1.5.1 The Spitzer Space Telescope (*Spitzer*) - mid-infrared to far-infrared

Spitzer is a single-dish space observatory with a mirror size of 0.85 m (where mirror size is limited by the feasibility what can be transported on the spacecraft). *Spitzer* operated[7] across near-infrared to far-infrared wavelengths at 3 μm – 180 μm. The two instruments used in this thesis are the Infrared Array Camera (IRAC; Fazio et al. 2004) operating from 3.6 μm – 8 μm and the Mid-Infrared Photometer for Spitzer (MIPS; Rieke et al. 2004) operating from 24 μm – 160 μm. The observations of Auriga-Cal with *Spitzer* are discussed in Chapter 2.

1.5.2 The Herschel Space Observatory (*Herschel*) - far-infrared to submm

Herschel is also a single-dish space observatory with a mirror size of 3.5 m that operated at 50 μm – 600 μm. *Herschel* made continuum observations of Auriga-Cal with the Photoconductor Array Camera and Spectrometer (PACS: Poglitsch et al. 2010) at 70 μm and 160 μm and the Spectral and Photometric Imaging REceiver (SPIRE: Griffin et al. 2010) at 250 μm, 350 μm, and 500 μm. These observations are discussed in Harvey et al. (2013). In this thesis, we adopt Harvey et al's PACS measurements and process the SPIRE data to measure YSO qualities in Chapter 3.

1.5.3 The James Clerk Maxwell Telescope (JCMT) - submm

The JCMT is a single-dish ground-based observatory. As such, it has a much larger mirror size of 15 m, in contrast to space-based observatories. The continuum instrument used for this dissertation is the Submillimetre Common-User Bolometer Array 2 (SCUBA-2) operates at 450 μm and 850 μm. Since the JCMT's mirror size is larger than *Herschel*'s, 450 μm JCMT observations are $\sim 5\times$ higher resolution than the 500 μm *Herschel* observations. Since the observations are taken from the ground, the atmosphere must be subtracted from the observations resulting in more filtering of large-scale structure in the SCUBA-2 maps than in the *Herschel* maps, which are taken above the atmosphere. The observations of Auriga-Cal with the JCMT are discussed in Chapter 3.

[7] *Spitzer* is still observing in "warm mission" since 2009 when it ran out of the cryogen, necessary to cool its instruments to observe at the longest wavelengths.

1.5.4 The Jansky Very Large Array (VLA) - radio

The VLA is ground-based observatory composed of an array of radio dishes referred to as an interferometer. As an array, the resolution depends on the spacings between the individual dishes, rather than being limited by the size of one individual dish.[8] The interferometer works as a spatial filter with the spatial scales sampled corresponding to the array spacings. The largest distance between two antennas in an array determines the highest spatial resolution and the minimum distance determines the largest angular scale of recovered emission. All the baselines in between sample emission on discrete spatial scales between the highest resolution and the largest angular scale. As all other spatial scales are filtered out, the flux measured with an interferometer will be lower than that measured with a single-dish at the same wavelength. Interferometry has been a very powerful tool for long wavelength astronomy since we are no longer limited by the sizes of radio dishes that are physically possible to construct and operate. The observations of Auriga-Cal with the VLA are discussed in Chapter 4.

[8] I use the terminology of "dish" rather than mirror as radio dishes have very different surfaces than telescopes observing at shorter wavelengths. The surface of a dish must be smooth on scales finer than the order of wavelength observed. Therefore, radio dishes can be quite rough in comparison to mirrors. Radio observatories operating at much longer wavelengths, for example, are composed of an array of antennas rather than a single "dish" structure.

Chapter 2

The *Spitzer* Survey of Interstellar Clouds in the Gould Belt. VI. The Auriga-California Molecular Cloud observed with IRAC and MIPS

Originally published in The Astrophysical Journal, Volume 786, Issue 1, article id. 37, 18 pp. (2014).

Authors: Hannah Broekhoven-Fiene, **Brenda C. Matthews**, **Paul M. Harvey**, **Robert A. Gutermuth**, **Tracy L. Huard**, **Nicholas F. H. Tothill**, **David Nutter**, **Tyler L. Bourke**, **James Di Francesco**, **Jes K. Jørgensen**, Lori E. Allen, Nicholas L. Chapman, Michael M. Dunham, Bruno Merín, Jennifer F. Miller, Susan Terebey, Dawn E. Peterson, Karl R. Stapelfeldt,

ABSTRACT

We present observations of the Auriga-California Molecular Cloud (AMC) at 3.6, 4.5, 5.8, 8.0, 24, 70 and 160 μm observed with the IRAC and MIPS detectors as part of the *Spitzer* Gould Belt Legacy Survey. The total mapped areas are 2.5 deg^2 with IRAC and 10.47 deg^2 with MIPS. This giant molecular cloud is one of two in the nearby Gould Belt of star-forming regions, the other being the Orion A Molecular Cloud (OMC). We compare source counts, colors and magnitudes in our observed region to a subset of the SWIRE data that was processed through our pipeline. Using color-magnitude and color-color diagrams, we find evidence for a substantial population of 166 young stellar objects (YSOs) in the cloud, many of which were previously

unknown. Most of this population is concentrated around the LkHα 101 cluster and the filament extending from it. We present a quantitative description of the degree of clustering and discuss the fraction of YSOs in the region with disks relative to an estimate of the diskless YSO population. Although the AMC is similar in mass, size and distance to the OMC, it is forming about 15 – 20 times fewer stars.

2.1 Introduction

The cycle 4 *Spitzer Space Telescope* Legacy project "The Gould Belt: Star Formation in the Solar Neighborhood" (PID: 30574; PI: L.E. Allen) completed the *Spitzer* survey of the large, nearby star-forming regions begun by the c2d Legacy Project (Evans et al., 2003, 2009). The cloud with the least prior study included in the survey is the cloud we have designated as "Auriga" which lies on the Perseus-Auriga border. This cloud has also been designated the California Molecular Cloud by Lada et al. (2009) since it extends from the California Nebula in the west to the LkHα 101 region and associated NGC 1529 cloud in the east. We adopt the name Auriga-California Molecular Cloud (AMC) to encompass both nomenclatures.

Despite the AMC's proximity to two of the most well-examined star-forming clouds, Taurus-Auriga and Perseus, it is a relatively unstudied region. Several dark nebulae were noted along its length by Lynds (1962), and CO associated with many Lynds objects was measured by Ungerechts & Thaddeus (1987), who note the presence of a CO "cloud extending from the California nebula (NGC 1499) in Perseus along NGC 1579 and LkHα 101 well into Auriga" (their cloud 12). Only very recently has a giant molecular cloud been unambiguously associated with the series of Lynds nebulae through high resolution extinction maps by Lada et al. (2009) who placed its distance firmly within the Gould Belt (GB) at 450 ± 23 pc. At this distance, the cloud's extent of 80 pc and mass of $\sim 10^5$ $M_\odot$ rivals that of the Orion Molecular Cloud (L1641) for the most massive in the Gould Belt. For the remainder of this paper, we adopt this distance of 450 pc for the entire AMC. This is consistent with the distance of 510^{+100}_{-40} pc found by (Wolk et al., 2010) on their study of LkHα 101 with Chandra. We note that this distance differs from that adopted by Gutermuth et al. (2009) for LkHα 101 of 700 pc.

We have mapped a significant fraction of the AMC with the Infrared Array Camera (IRAC; Fazio et al. 2004) and the Mid-Infrared Photometer for *Spitzer* (MIPS; Rieke et al. 2004) on board the *Spitzer Space Telescope* (Werner et al., 2004), with a total

overlapping coverage of 2.5 deg^2 in the four IRAC bands (3.6, 4.5, 5.8 and 8.0 μm) and 10.47 deg^2 in the three MIPS bands (24, 70, and 160 μm). The mapped areas are not all contiguous and were chosen to include the areas with $A_V > 3$, as given by the Dobashi et al. (2005) extinction maps. The goal of these observations is to identify and characterize the young stellar object (YSO) and substellar object populations. The data presented here are the first mid-IR census of the YSO population in this region. The area around LkHα 101 and its associated cluster was observed as part of a survey of 36 clusters within 1 kpc of the Sun with *Spitzer* by Gutermuth et al. (2009) and those data have been incorporated into our dataset through the c2d pipeline.

More recently, the AMC has been observed by the *Herschel Space Observatory* at 70 – 500 μm, and by the Caltech Submillimeter Observatory with the Bolocam 1.1 mm camera (Harvey et al., 2013). These observations characterize the diffuse dust emission and the cooler Class 0 and Class I objects which can be bright in the far-IR. We do not analyze the large scale structure of the cloud in this paper as Harvey et al. (2013) present such an analysis with the *Herschel* observations, which are more contiguous and have a higher resolution than our MIPS observations. Harvey et al. (2013) also include a comparison to these MIPS data and so further analysis is not required here.

We describe the observations and data reduction (briefly as it is well-documented elsewhere) in § 3.2. In § 2.3, we describe the source statistics, the criteria for identifying and classifying YSO candidates and we compare the YSO population to other clouds. The SEDs and disk properties of YSOs are modeled in § 2.4. We characterize the spatial distribution of YSOs in § 2.5 and summarize our findings in § 3.4.

2.2 Observations and Data Reduction

The areas mapped are shown in Figure 2.1. The MIPS coverage is more contiguous than the IRAC coverage due to the mapping modes of the two instruments. Observations were designed to cover regions with $A_V > 3$ within the extinction maps of Dobashi et al. (2005). All areas were observed twice with IRAC and MIPS cameras with the AORs and dates of the observations compiled in Tables 2.1 and 2.2. The two epochs were compared to remove transient asteroids that are numerous at the low ecliptic latitude of these observations.

The GBS survey data and the LkHα 101 data from Gutermuth et al. (2009) were processed through the c2d pipeline. Details of the data processing are available in

IRAC Sub-region	Size (sq. deg.)	AOR Sub-region ID	AOR Key (1st epoch, 2nd epoch)
AUR_1a	0.3 × 0.2	auri_irac6b	19972096, 19971584
AUR_1b	0.4 × 0.3	auri_irac6	20014336, 20014080
AUR_1c	0.9 × 0.3	auri_irac7	19980544, 19980288
		auri_irac7b	19984384, 19984128
AUR_1d	0.3 × 0.2	non-GB data	03654144
AUR_1e	0.3 × 0.3	auri_irac8	20013312, 20013056
AUR_2a	1.3 × 1.4	auri_irac3	19983360, 19983104
		auri_irac4	20016640, 20016384
		auri_irac5	19981824, 19981568
		auri_irac5b	19956480, 19956224
AUR_2b	0.4 × 0.3	auri_irac2	20018432, 20017920
AUR_3a	0.8 × 0.9	auri_irac1	19984640, 19967744
		auri_irac9	19978240, 19977984
AUR_3b	0.4 × 0.3	auri_irac9b	20012288, 20011776
		auri_irac9c	19976960, 19976192
AUR_4a	0.4 × 0.7	auri_irac10	19993344, 19993088
		auri_irac10b	19988992, 19988736
AUR_4b	0.3 × 0.3	auri_irac11	19961088, 19960832
AUR_5	0.3 × 0.3	auri_irac12	19992576, 19992064
AUR_NORTH	0.5 × 0.3	auri_irac13	19960320, 19959808

Table 2.1 Summary of IRAC Observations

MIPS Sub-region	Size (sq. deg)	AOR Key
AUR_1	1.2 × 3.2	20019712,19983872,20019456,19983616
AUR_2	1.6 × 2.6	20017152,19982336,20016896,19982080
AUR_3	1.0 × 2.0	20015360,20014848
AUR_4	1.4 × 2.2	19981312,19979520,19981056,19979008
AUR_5	0.5 × 1.9	20013824,20013568
AUR_NORTH	0.5 × 1.9	20011520

Table 2.2 Summary of MIPS Observations

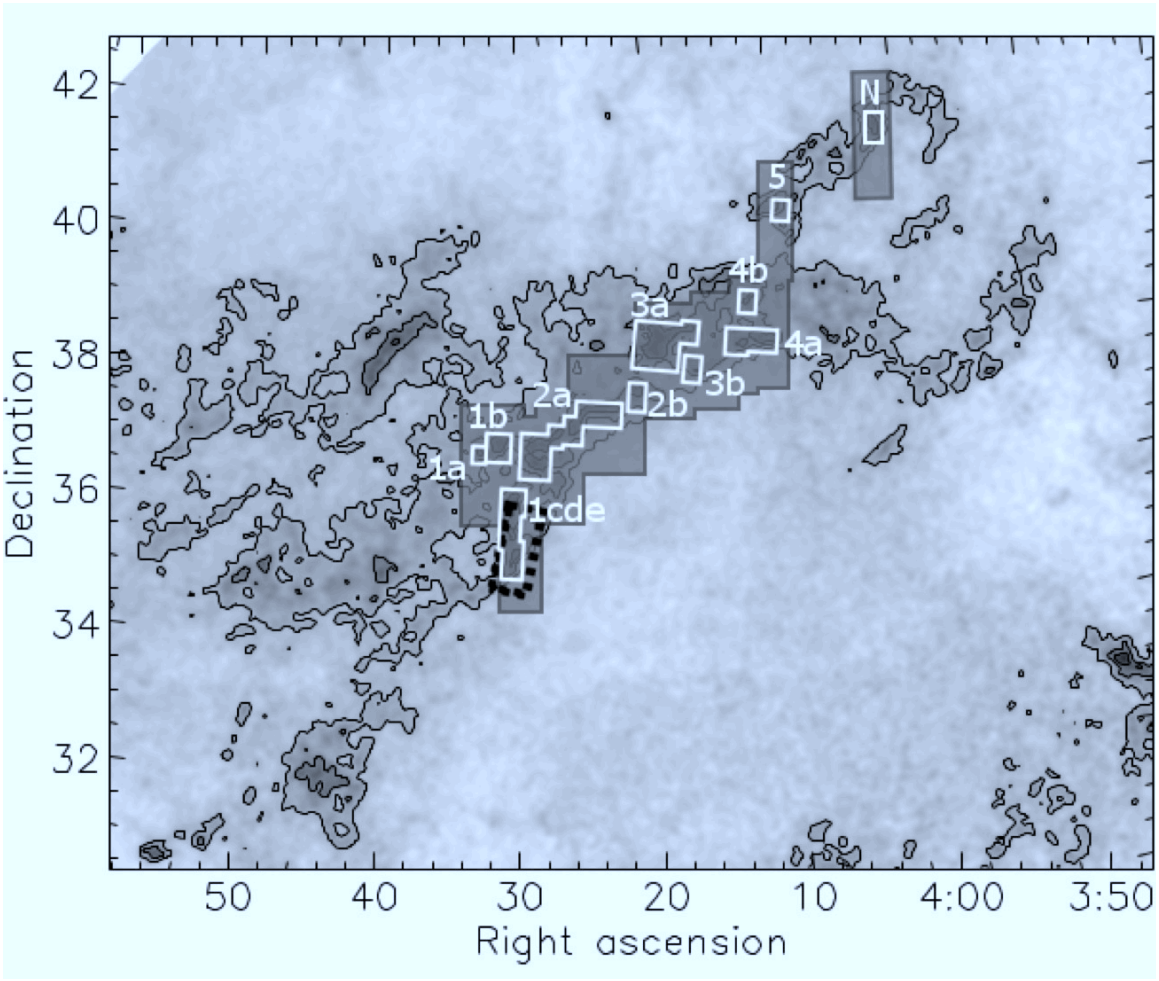

Figure 2.1 Integrated *Spitzer* mapped areas from the Gould Belt Survey and other projects. The grey boxed area shows the MIPS coverage; the white boxes show the IRAC coverage (with the sub-regions labelled); and the hatched black box shows the non-GBS survey data in the field from Gutermuth et al. (2009). These regions are schematic to give a general picture of the layout of the coverage and to identify the subregions. The greyscale is the extinction map of Dobashi et al. (2005). Contours show the A_V levels of 1, 3 and 5 mag.

Evans et al. (2007). Briefly, the data processing starts with a check of the images whereupon image corrections are made for obvious problems. Mask files are created to remove problematic pixels. The individual frames are then mosaicked together, with one mosaic created for each epoch and one joint mosaic as well. Sources are detected in each mosaic and then re-extracted from the stack of individual images which include the source position. Finally, the source lists for each wavelength are band-merged, and sources not detected at some wavelengths are "band-filled" to find appropriate fluxes or upper limits at the positions which had clear detections at other wavelengths.

As noted by Harvey et al. (2008), the details of this data reduction are essentially the same as that of the original c2d datasets except that the input to the c2d pipeline are products of later versions of the *Spitzer* BCD pipeline. The c2d processing of IRAC data was described by Harvey et al. (2006), and the MIPS data processing was described by Young et al. (2005) and Rebull et al. (2007). Harvey et al. (2007) describe additional reduction processes which we have used for the AMC data.

2.3 Star-forming Objects in the AMC

Figures 2.2 – 2.5 show RGB mosaics for the IRAC covered regions using 4.5 μm (blue), 8.0 μm (green) and 24 μm (red) data with the positions of YSOs overlaid. The diffuse 8.0 μm emission is strongly concentrated at the eastern edge of the cloud, near the well-known object LkHα 101. The LkHα 101 data are taken from and have been discussed by Gutermuth et al. (2009).

2.3.1 YSO Selection

The majority of objects in our fields are not YSOs. The maps are contaminated by background/foreground stars and background galaxies. We have selected our YSO candidates (YSOcs) by various methods, augmenting the list where possible based on data outside the *Spitzer* IRAC/MIPS wavelength bands. The fundamental criteria use IRAC, MIPS and 2MASS data (Cutri et al., 2003) and are based on identification of infrared excess and brightness limits below which the probability of detection of external galaxies becomes high. The total number of sources is 704,045. In regions observed by both IRAC and MIPS, the YSOc selection follows that of Harvey et al. (2008). We refer to these as IRAC+MIPS YSOcs. For objects with upper limits on

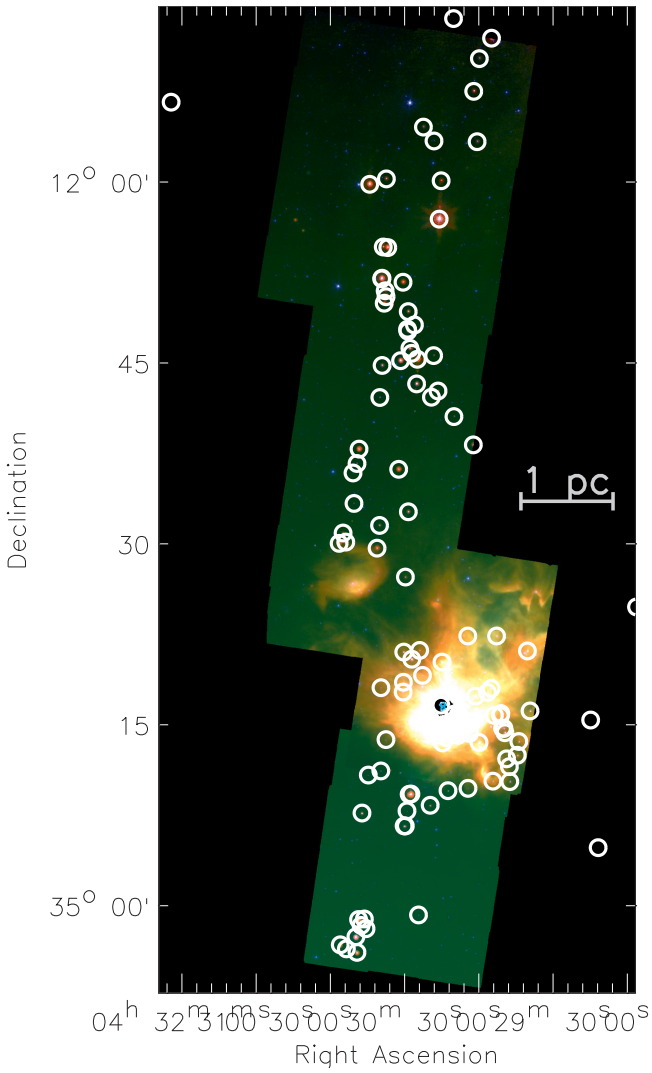

Figure 2.2 False colour image with 4.5 μm (blue), 8 μm (green), and 24 μm (red) of the IRAC 1cde fields with YSO positions are overlaid. (Similar figures for other IRAC regions are shown in Figures 2.3 – 2.5.)

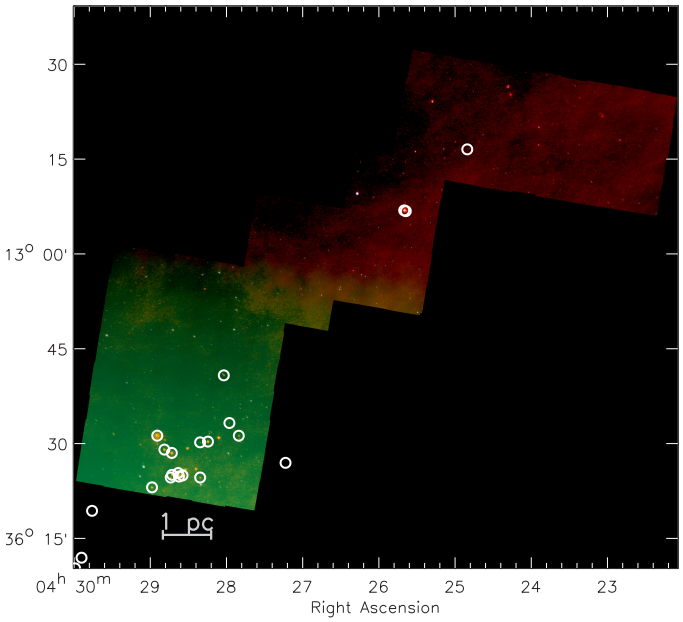

Figure 2.3 False colour image with 4.5 μm (blue), 8 μm (green), and 24 μm (red) of the IRAC 2a field with YSO positions are overlaid. (Similar figures for other IRAC regions are shown in Figures 2.2, 2.4, and 2.5.)

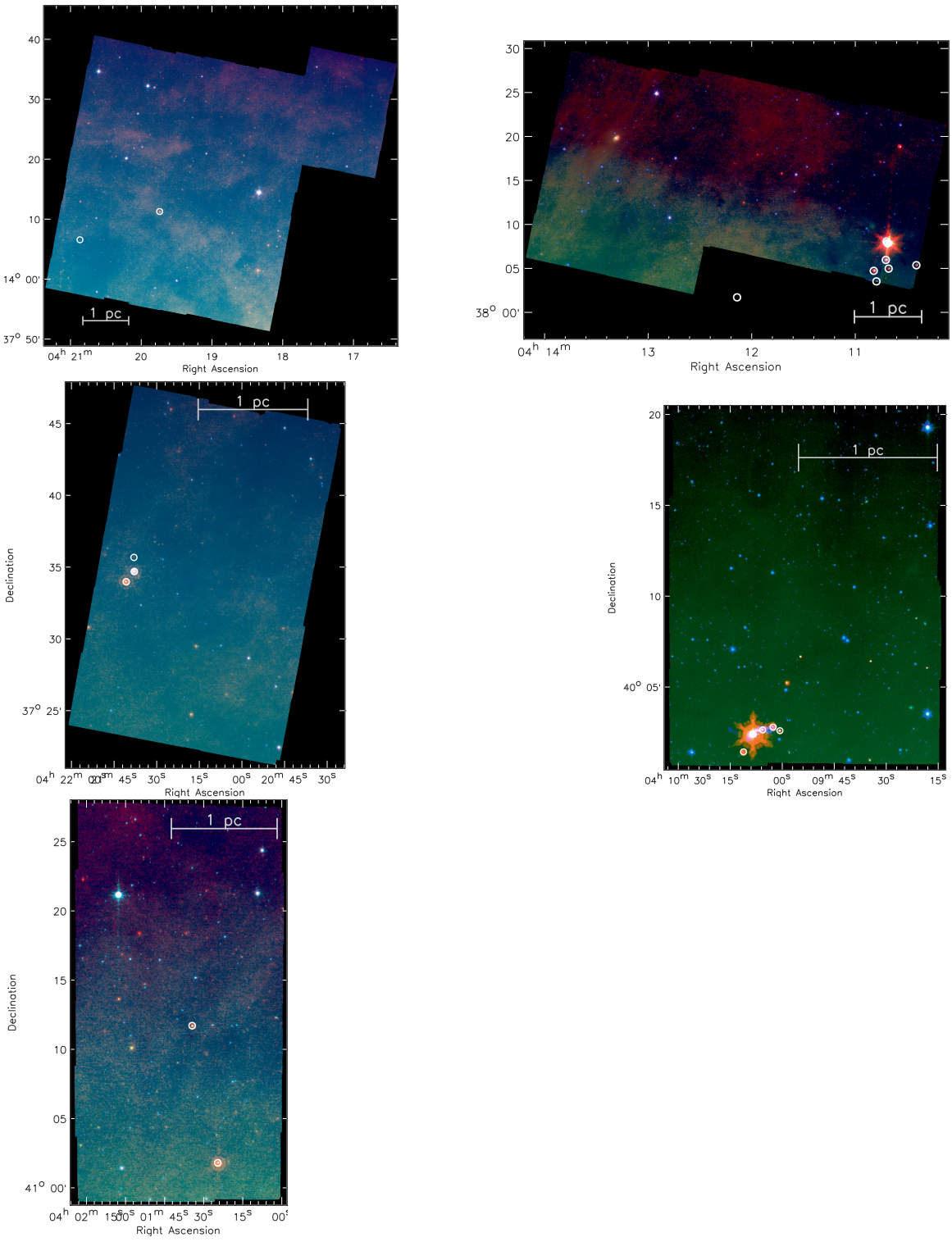

Figure 2.4 False colour image with 4.5 μm (blue), 8 μm (green), and 24 μm (red) of the IRAC fields 3a, 4a, 2b, 5, and North (left to right, top to bottom) with YSO positions are overlaid. These regions contain only a few YSOs each. (Similar figures for other IRAC regions are shown in Figures 2.2, 2.3, and 2.5.)

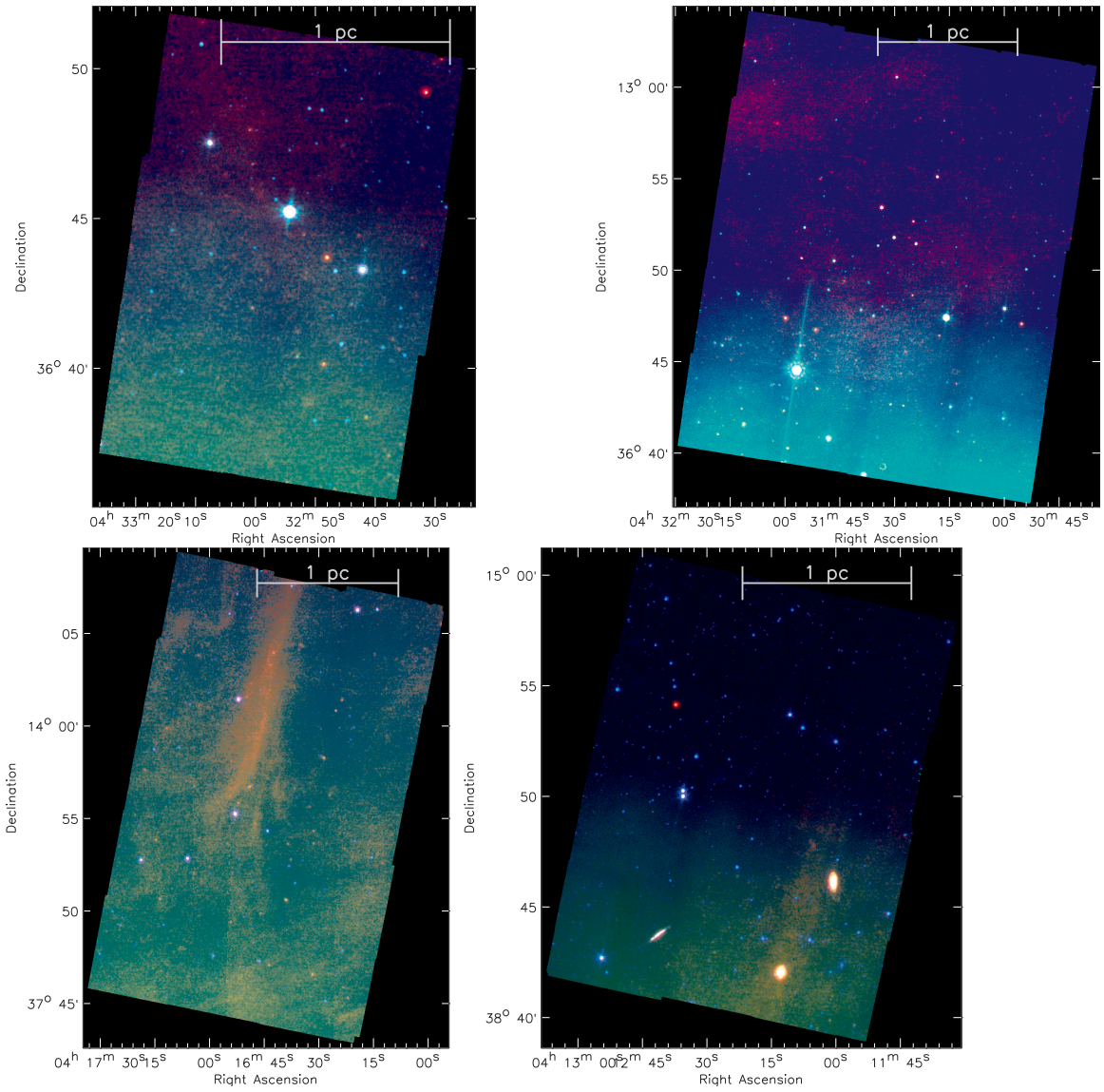

Figure 2.5 False colour image with 4.5 μm (blue), 8 μm (green), and 24 μm (red) of the IRAC fields 1a, 1b, 3b, and 4b (left to right, top to bottom) with YSO positions are overlaid. These regions do not contain YSOs. (Similar figures for other IRAC regions are shown in Figures 2.2 – 2.4.)

Sources	Number
Total	704045
YSO	166
Galc	322
Stellar	32579
2MASS	87745
Zero [a]	247257
Something else	335976

Table 2.3 Sources in the AMC Field

[a]Sources that do not have detections in the combined epochs data in any of the 2MASS, IRAC or MIPS bands. (It may have been detected in one or both of the epochs at different bands.)

the MIPS 24 μm flux, we follow the method outlined by Harvey et al. (2006). We refer to these as IRAC-only YSOcs. In regions observed only by MIPS and not IRAC, we have used the formalism of Rebull et al. (2007), except we use a tighter 2MASS K_S cut of $[K_S] < 13.5$. This tighter magnitude cut removed objects that were similar in color and magnitude to others that had already been eliminated. We further remove galaxies from the MIPS-only source list by including photometry from the Wide-field Infrared Survey Explorer (WISE; Wright et al. 2010) and applying color cuts suggested by Koenig et al. (2012) (see their Figure 7) and requiring the WISE Band 2 magnitude criterion of $[4.6] < 12$. We refer to these as MIPS-only YSOcs. Note that the MIPS-only YSOcs were not observed with IRAC, as opposed to the IRAC-only YSOcs which were observed, but not detected, with MIPS.

Figure 2.6 shows the IRAC color-magnitude and color-color diagrams relevant for classifying IRAC-only sources. The different domains occupied by stars, YSOcs, and other (e.g., extragalactic) sources are are shown.

For sources in regions observed by both IRAC and MIPS, Figure 2.7 shows the color and magnitude boundaries used to remove sources that are likely extragalactic. This identification is done by comparing the observed fluxes and colors to results from the SWIRE extragalactic survey (Surace et al., 2004). The sources in the AMC field are compared to a control catalogue from the SWIRE dataset that is resampled to match our sensitivity limits and the extinction level derived for the AMC. (See Evans et al. 2007 for a complete description.)

Finally, we vetted the YSOcs through individual inspection of the *Spitzer* maps (and optical images where available), and determined that 24 of the original 159 IRAC+MIPS YSOcs, 14 of the original 17 IRAC-only YSOcs, and 56 (26 based

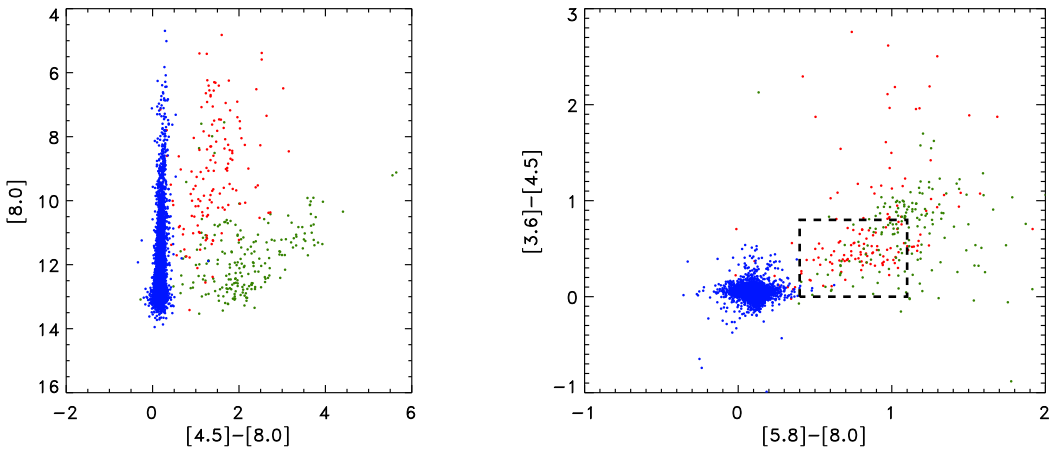

Figure 2.6 IRAC colors of the sources in the the regions observed with IRAC. Stars are in blue; YSOs are in red; and "other sources" (e.g., galaxies) are in green. The boxed region on the right panel marks the approximate domain of Class II sources identified by Allen et al. (2004).

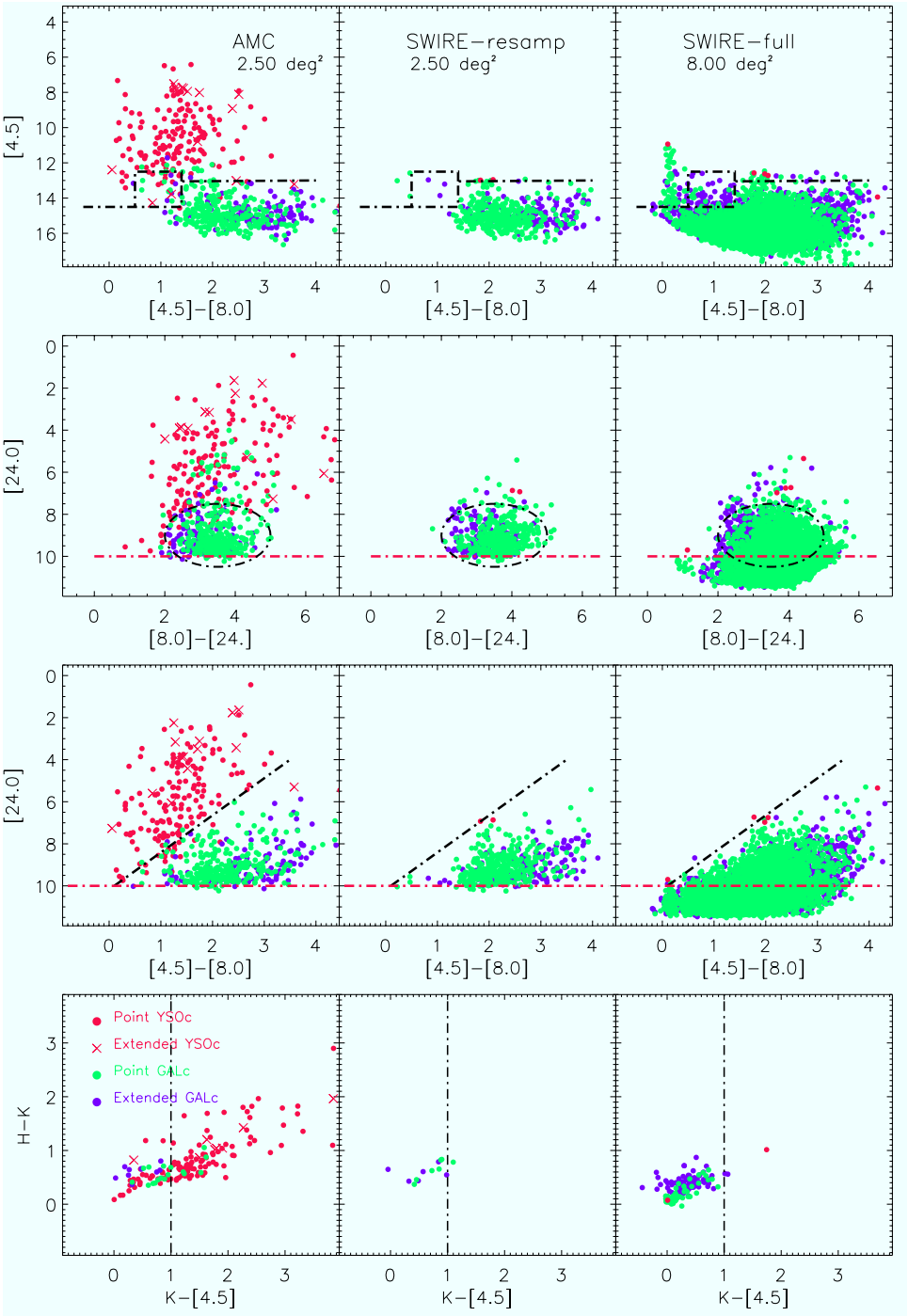

Figure 2.7 Color-magnitude and color-color diagrams for the AMC (left), the SWIRE dataset resampled to match our sensitivities and measured extinction (middle), and the full SWIRE dataset (right). The black dash-dot lines show soft boundaries for YSO candidates whereas the red dash-dot lines show hard limits, fainter than which objects are not included as YSO candidates.

ID	Name	Class	α	3.6 μm (mJy)	4.5 μm (mJy)	5.8 μm (mJy)	8.0 μm (mJy)	24.0 μm (mJy)	70.0 μm (mJy)
1[N]	04012455+4101490	I	2.04	0.50±0.03	4.06±0.20	7.94±0.38	8.49±0.41	352± 32	8410± 965
2[N]	04013436+4111430	II	-1.00	10.5± 0.5	9.66±0.46	8.99±0.44	7.65±0.36	14.7± 1.4	288± 30
3	04100064+4002361	II	-0.31	2.64±0.13	3.63±0.18	4.50±0.22	5.16±0.25	9.66±0.93	···
				...					
136	04295017+3514445	II	-0.90	2.82±0.14	2.38±0.12	2.35±0.15	3.14±0.20	< 7.75	···
137	04300986+3514163	II	-0.47	27.6± 1.4	30.2± 1.5	25.7± 1.5	28.6± 2.5	< 40.4	···
138	04301521+3516398	F	-0.22	131± 12	85.4±13.2	198± 28	368± 52	< 196	···

Table 2.4 YSOs in the AMC Based on IRAC and MIPS

*The YSO is in a region of low column density ($N_{\rm H2} < 5\times10^{21}$ cm^{-2}) and so is a possible contaminant.

[N]The YSO lies beyond the $N_{\rm H2}$ column density map from Harvey et al. (2013) and so $N_{\rm H2}$ at its position is unknown.

Note. — The names of the YSOs give their J2000 positions. Note that YSOs with 24 μm upper limits are identified according to the IRAC-only criteria. Table 2.4 is published in its entirety in the electronic edition of the *Astrophysical Journal*. A portion is shown here for guidance regarding its form and content.

on WISE and other photometric criteria) of the original 84 MIPS-only YSOcs were unlikely to be YSOs. Henceforth we refer to the list of vetted YSOcs, totalling 166, as YSOs to distinguish them from the raw unvetted list. While we have undergone an extensive process to construct a list of sources that are very likely to be YSOs, we stress that these YSOs have not been confirmed spectroscopically. Table 2.3 lists the final source counts for objects in the observed fields. The IRAC and MIPS fluxes of the IRAC+MIPS and IRAC-only YSOs are listed in Table 2.4. The 70 μm fluxes have been listed where available. (There are fewer YSOs with fluxes at 70 μm because of the lower sensitivity and, in some cases, the bright background.) The fluxes of MIPS-only vetted YSOs are listed in Table 2.5 with their WISE and MIPS fluxes (and IRAC fluxes where available). In Tables 2.4 and 2.5, we have noted which YSOs are in regions of low column density ($N_{\rm H2} < 5 \times 10^{21}$ cm^{-2}) according to the column density maps by Harvey et al. (2013), as these are more likely to be contaminants than YSOs in regions of high column density.

ID	Name	Class	α	IRAC 3.6 μm mJy	IRAC 4.5 μm mJy	IRAC 5.8 μm mJy	IRAC 8.0 μm mJy	WISE 3.4 μm (mJy)	WISE 4.6 μm (mJy)	WISE 12 μm (mJy)	WISE 22 μm (mJy)	MIPS 24.0 μm (mJy)	MIPS 70.0 μm (mJy)
139[N]	04022975+4042419	II	-1.25	···	···	···	···	1631± 84	2646± 99	964± 13	350± 8	259± 24	···
140	04090200+4019131	I	0.95	···	···	···	···	12.3± 0.3	58.8± 1.1	165± 2	977± 18	980± 91	3730± 434
141*	04100343+3904495	III	-1.85	···	···	···	···	1576± 81	1072± 24	865± 12	667± 13	418± 43	···
142	04102441+3805227	II	-0.81	···	15.5± 0.8	···	21.3± 1.1	15.0± 0.3	17.0± 0.3	20.7± 0.4	26.5± 1.4	25.0± 2.3	···
143*	04120847+3801466	III	-2.08	50.7± 2.5	···	22.6± 1.1	···	59.7± 1.2	33.4± 0.6	10.5± 0.3	21.9± 1.6	8.49±0.82	···
144*	04125764+3914183	III	-1.97	···	···	···	···	4653± 342	3817± 162	1118± 17	930± 17	809± 76	90.7±10.2
145*	04134457+3904357	III	-2.02	···	···	···	···	21.3± 0.4	11.8± 0.2	2.26±0.22	5.64±1.71	3.48±0.46	246± 28
146*	04151120+3839571	II	-1.49	···	···	···	···	160± 3	133± 2	73.9± 1.0	79.1± 2.3	64.9± 6.0	···
147*	04155405+3834131	III	-1.96	···	···	···	···	20.3± 0.4	11.5± 0.2	2.89±0.18	8.14±1.00	3.93±0.41	···
148*	04170593+3722187	III	-2.07	···	···	···	···	1927± 107	1381± 40	479± 6	329± 8	250± 23	···
149*	04230546+3807369	III	-1.93	···	···	···	···	55.5± 1.2	31.6± 0.6	12.1± 0.3	22.7± 1.3	11.5± 1.2	···
150*	04271374+3627107	II	-1.56	···	···	···	···	4.28±0.20	2.39±0.11	1.01±0.16	< 12.6	1.81±0.29	···
151*	04285556+3524460	II	-1.16	···	···	···	···	3.51±0.08	2.52±0.06	1.94±0.21	4.02±1.22	3.42±0.37	···
152*	04291153+3504495	II	-1.30	···	···	···	···	9.03±0.20	7.20±0.14	5.59±0.20	9.73±1.08	7.39±0.73	···
153*	04291438+3515245	II	-1.28	···	···	···	···	129± 2	106± 1	90.3± 1.5	129± 4	85.9± 8.0	109± 21
154*	04294628+3619235	F	-0.21	23.7± 1.2	···	29.9± 1.4	···	20.5± 0.4	26.3± 0.4	33.8± 0.5	123± 3	123± 11	290± 30
155*	04295254+3522236	III	-1.89	···	29.4± 1.4	···	12.8± 0.7	53.3± 1.2	32.5± 0.7	53.5± 1.3	45.2±12.2	14.3± 1.6	···
156	04295418+3611573	F	-0.15	···	···	···	···	78.4± 1.6	87.1± 1.4	149± 1	582± 7	534± 50	721± 75
157	04295919+3610161	II	-1.22	···	16.3± 0.8	···	17.6± 0.8	18.5± 0.4	18.8± 0.4	15.3± 0.3	10.8± 1.6	10.6± 1.0	88.1±11.3
158*	04300152+3607333	II	-0.67	···	37.2± 1.8	···	36.4± 1.7	30.6± 0.6	34.7± 0.7	35.7± 0.6	61.7± 1.9	60.0± 5.6	98.6±14.7
159*	04300188+3538147	II	-0.39	···	26.7± 3.2	···	···	66.5± 1.4	95.2± 1.7	121± 1	191± 4	103± 9	115± 15
160*	04300980+3613354	II	-1.12	···	···	···	···	30.4± 0.6	26.5± 0.5	27.8± 0.5	33.1± 1.4	29.5± 2.7	···
161	04304933+3450460	II	-0.87	5.52±0.27	···	5.95±0.29	···	3.67±0.08	5.02±0.10	3.65±0.18	5.16±1.12	5.40±0.58	···
162	04304948+3450562	II	-0.81	8.02±0.38	···	5.12±0.25	···	8.03±0.18	6.40±0.14	4.02±0.20	21.1± 1.4	19.2± 1.8	···
163	04305208+3450089	F	-0.15	20.2± 1.0	···	23.5± 1.1	···	22.9± 0.7	28.9± 0.8	53.1± 1.0	136± 5	114± 10	···
164*	04320577+3606375	III	-1.95	···	···	···	···	4827± 402	3258± 129	715± 9	992± 16	874± 82	···
165*	04325431+3604440	II	-1.12	···	···	···	···	2.51±0.06	1.83±0.05	1.36±0.13	5.26±0.89	3.39±0.40	···
166*	04330315+3602045	II	-1.02	···	···	···	···	2.14±0.06	1.98±0.05	1.74±0.14	2.74±0.98	2.71±0.32	···

Table 2.5 YSO Candidates in the AMC Based on WISE and MIPS

Table 2.5 *Continued:* YSO Candidates in the AMC Based on WISE and MIPS (table notes)

---

*The YSO is in a region of low column density ($N_{H2} < 5\times10^{21}$ cm^{-2}) and so is a possible contaminant.

^{N}The YSO lies beyond the N_{H2} column density map from Harvey et al. (2013) and so N_{H2} at its position is unknown.

Note. — The names of the YSOs give their J2000 positions. These YSOs are outside the 4 band IRAC coverage area and so are identified based on their WISE and MIPS fluxes. The coverage of individual IRAC bands are slightly offset from each other. Therefore some YSOs at the edges of the IRAC coverage have fluxes at some IRAC wavelengths. Table 2.5 is also published in the electronic edition of the *Astrophysical Journal*.

We compare our final YSO source list to those found for LkHα 101 in Gutermuth et al. (2009). All 103 YSOs in Gutermuth et al. (2009) are identified as sources in our catalogue with positions that are within a couple tenths of an arcsecond agreement. Where this work and Gutermuth et al. (2009) provide fluxes, they agree at the shorter IRAC bands (IRAC1-3) typically within 0.05 – 0.1 mag. At IRAC4 and MIPS1, the agreement is typically within 0.2 mag. These differences are what one might expect for PSF-fitting (used here) versus aperture fluxes (used by Gutermuth et al. 2009) at wavelengths where there is substantial diffuse emission. (Recall that we have incorporated their dataset into our own.) Therefore no previously identified sources have been missed in this study, and our measurements agree well with those of Gutermuth et al. (2009). Note, however, that the different classification methods used in this work and by Gutermuth et al. (2009) each yield a different total number of YSOs in this region; we have identified 42 YSOs whereas Gutermuth et al. (2009) identified 103. Our total breaks down into 7 YSOs identified here that were not identified by Gutermuth et al. (2009) and 35 YSOs shared between the two lists. (The c2d pipeline identified 47 YSOcs that were listed as YSOs by Gutermuth et al. (2009), but 12 were removed during the vetting process.) The major source of this discrepancy is that we require 4 (or 5) band photometry with S/N $\geq$ 3 in IRAC (and MIPS 24 μm bands) to identify YSO candidates. Such criteria are especially difficult to satisfy in the region of bright and diffuse emission around LkHα 101. Therefore, our results do not contradict those in Gutermuth et al. (2009), rather we believe that the stringent criteria used here have excluded some YSOs. We keep these criteria for consistency with other c2d and *Spitzer* GBS observations and analyses, but note the limitations in such a bright region.

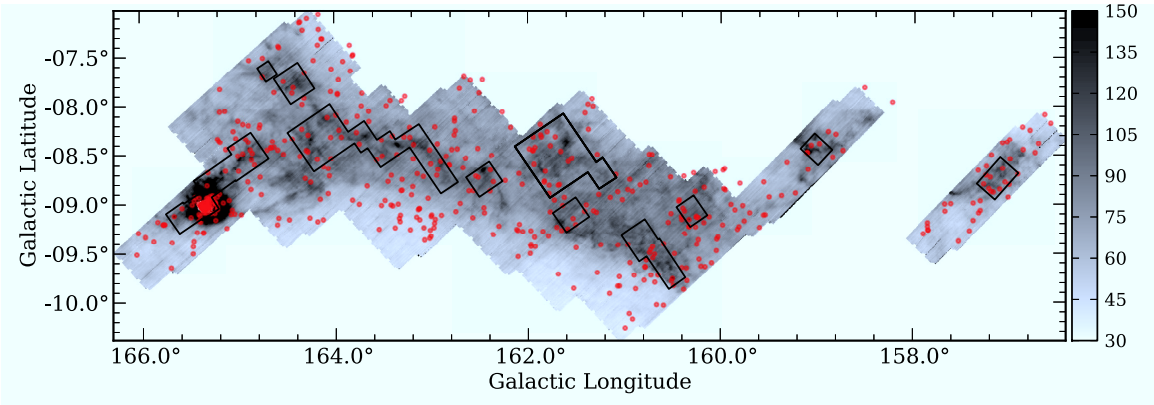

Figure 2.8 Sources with SEDs consistent with a reddened stellar photosphere and a dust component (IR excess) but for which detections with S/N $\geq$ 3 across all 4 IRAC bands, required to considered a YSOc, did not exist (see text). The positions of these sources are plotted against the 160 μm greyscale (colorbar units are MJy sr^{-1}). The striking over-density at the center of LkHα 101 compared to other IRAC+MIPS regions (marked by black lines) suggests that we are missing veritable YSOs in this region. The robust set of measurements required to identify whether a source is a likely YSO or background galaxy is difficult to attain in this region of very bright emission.

The diffuse emission problem is isolated to the immediate vicinity of LkHα 101. To demonstrate this point, in Figure 2.8 we have plotted the location of all the sources having an SED consistent with being a reddened stellar photosphere and an associated dust component, which do not have S/N $\geq$ 3 at all IRAC bands. The SEDs of these sources are classified as 'star+dust' in our catalogue. Of the 56 YSOs listed by Gutermuth et al. (2009) that were not identified as YSOs in this work, the majority of them (34 of 56) have a 'star+dust' SED. There is a total of 465 'star+dust' sources without robust 4-band IRAC fluxes in the AMC field. These sources are relatively evenly distributed throughout the field, with the exception of a striking over-density at the center of LkHα 101 compared to other IRAC regions. Therefore, we believe this over-density is an effect of the difficulty in getting detections with S/N $\geq$ 3 across 4 bands in the bright LkHα 101 region and not that there are significantly fewer YSOs than suggested by Gutermuth et al. (2009).

Harvey et al. (2013) identified 60 YSOs in the AMC with *Herschel*/PACS, 49 of which are also identified in this work. Four of these *Spitzer*-identified YSOs are members of pairs of YSOs that are blended in the *Herschel* images. *Herschel* is more sensitive to the rising- and flat-spectrum sources, i.e., of the other 45 *Spitzer*-identified YSOs that are also detected in the *Herschel* maps, most (76%) are Class I/F objects, and the remaining 24% are Class IIs.

2.3.2 YSO classification

The YSOs are classified according to the slope of their SED in the infrared (see Evans et al. 2009 for a description). The spectral index, α, is given by

$$\alpha \equiv \frac{\mathrm{d}\log(\lambda S(\lambda))}{\mathrm{d}\log(\lambda)} \tag{2.1}$$

and determined by fitting the photometry between 2 μm and 24 μm. The distribution of α values is shown in Figure 2.9 along with the relative number of YSOs in each SED class. The majority of YSOs identified in the cloud are Class II objects (55%). The percentage of sources in each SED class for the AMC is strikingly similar to that of Perseus (23%, 11%, 58%, and 8% for Class Is, Fs, IIs and IIIs, respectively; Evans et al. 2009).

Table 2.6 lists the breakdown of Class Is, Fs, and IIs for the AMC and other clouds in the GB and c2d surveys to estimate their relative ages. We did not include Class

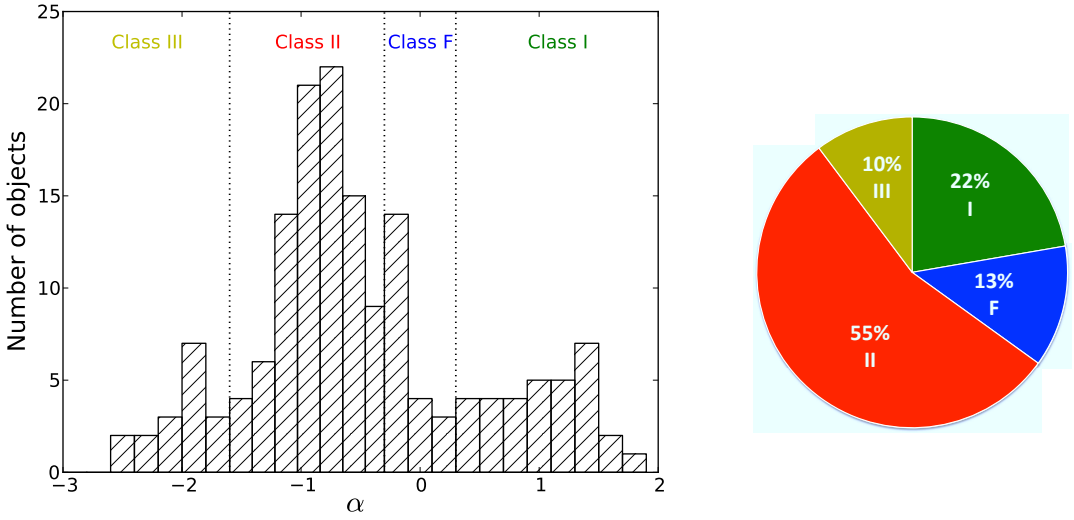

Figure 2.9 Left: Distribution of α values (the slope of the SED in the IR) used to determine the 'class' of the YSOs in the AMC. The vertical dotted lines mark the boundaries between the different classes as defined by Greene et al. (1994). Right: Pie chart for the AMC showing the percentage of sources in each SED class. Green is Class I; blue is Flat; red is Class II; and yellow is Class III (colors are the same as in Figure 2.18).

Region	$N_{\rm YSO}$	$N_{\rm I}$	$N_{\rm F}$	$N_{\rm II}$	$N_{\rm I+F}/N_{\rm II}$
AMC	149	37	21	91	0.64
OMC	3330	668	467	2195	0.52
Perseus	368	54	71	243	0.51
Serpens	196	39	25	132	0.49
Ophiuchus	258	35	47	176	0.47
IC 5146	128	29	12	87	0.47
Cepheus Flare	122	21	14	87	0.40
Corona Australis	37	7	2	28	0.32
Lupus	95	8	12	75	0.27
Chameleon II	22	2	1	19	0.16

Table 2.6 Relative ages

References. — AMC: this work, OMC: Megeath et al. (2012), Perseus: Jørgensen et al. (2006), Serpens: Harvey et al. (2007), Ophiuchus: L. Allen, in preparation (see Evans et al. 2009), IC 5146: Harvey et al. (2008), Cepheus Flare: Kirk et al. (2009), Corona Australis: Peterson et al. (2011), Lupus: Merín et al. (2008), Chameleon II: Alcalá et al. (2008)

IIIs in this analysis since this population is typically incomplete in *Spitzer* surveys (e.g., see discussions in Harvey et al. 2008; Evans et al. 2009; Gutermuth et al. 2009) due to their weak IR excess. This simplifies the comparison to other clouds where the completeness limits may vary. We compared the ratio of Class Is and Fs to Class IIs, $N_{\rm I+F}/N_{\rm II}$, for the different cloud populations in other GB and c2d surveys which use the same classification scheme. We also include YSOs in the OMC identified with *Spitzer* by Megeath et al. (2012); since they use a different classification scheme however, we have re-calculated the α values for their sample. The Class I/F lifetime is relatively short compared to the Class II lifetime, and therefore a higher ratio indicates a younger population (see discussion in Evans et al. 2009). The high number of Class Is and Fs suggests that the AMC is relatively young compared to other clouds.

Finally, we also compared the number of YSOs per square degree in the AMC (11.5 deg^2)[1] to that in the OMC (14 deg^2). The OMC is forming vastly larger amounts of stars. It has 237 YSOs per deg^2 whereas the AMC only has 13 YSOs per deg^2, a factor of about 20 fewer. Even if we only compare the number of YSOs in the OMC with 4 band photometry (as this was the source of the discrepancy between the total number of YSOs around LkHα 101 identified in this work and by Gutermuth et al. 2009, who use a similar identification method to Megeath et al. 2012), this still suggests that there is at least a factor 15 more YSOs in the OMC than in the AMC. Despite the differences in identification methods used for the OMC and for the AMC, it is clear that the OMC is forming far more stars than the AMC is. The YSOs in the OMC are also concentrated much more strongly than the AMC, despite both clouds having comparable sizes and masses. We note that Lada et al. (2009) attribute the difference between the amount of star formation to the different amounts of material at high A_V/column density.

2.4 Spectral Energy Distribution Modeling

Optical data of the YSOs were downloaded from the USNO NOMAD catalogue (Zacharias et al. 2004). SEDs of the YSOs are shown in Figures 2.10 and 2.11 (Class Is and Class Fs), 2.12 – 2.14 (Class IIs) and 2.15 (Class IIIs). We were able to perform relatively detailed modelling of the stellar and dust components of the

[1]Here we use the total coverage of IRAC + MIPS1, the five bands used to identify YSOs. This differs from the overlapping MIPS1, MIPS2 and MIPS3 coverage of 10.47 deg^2 described in Section 3.1.

Class II and Class III sources (YSOs which are not heavily obscured by dust). The luminosities of sources in the earlier classes are presented in Dunham et al. (2013). The majority of the Class II and Class III sources are likely in the physical stage where the stellar source and circumstellar disk are no longer enshrouded by a circumstellar envelope. We note that the observed "class" does not always correspond to the associated physical stage of the YSO (see discussion in Evans et al. 2009) and that some Class IIs may be sources, viewed pole-on, with circumstellar envelopes that are only beginning to dissipate. Conversely, an edge-on disk without an envelope could look like a Class I object.

Our SED modelling methods follow those used by Harvey et al. (2007) (and similar works since, e.g., Merín et al. 2008, Kirk et al. 2009) to model the SEDs. The stellar spectrum of a K7 star was fit to the SEDs by normalizing it to the de-reddened fluxes in the shortest available IR band of J, K or IRAC1. We use the extinction law of Weingartner & Draine (2001) with $R_V = 5.5$ to calculate the de-reddened fluxes. The A_V value was estimated by matching the de-reddened fluxes with the stellar spectrum. In eight cases, we used an A0 spectrum when the K7 spectrum was unable to produce a reasonable fit. The use of only two stellar spectra is of course over-simplified to represent the range of stellar spectra possible; however, it produces adequate results for the purposes of this study. More exact spectral typing is difficult with only the photometric data presented here and the uncertainties in A_V. We nevertheless obtain a broad overview of the disk population with the applied assumptions. Tables 2.7 and 2.8 list the stellar spectrum, the A_V value, and stellar luminosity ($L_{\rm star}$) used for the stellar models of each source's SED for the Class II and Class III YSOs, respectively.

2.4.1 Second order SED parameters $\alpha_{\rm excess}$ and $\lambda_{\rm turnoff}$

The first order SED parameter α is used as a primary diagnostic of the excess and circumstellar environment and to separate the YSOs into different "classes" (§ 2.3.2). Once we have a model of the stellar source, however, we are able to characterize the circumstellar dust better. For each source we determined the values of $\alpha_{\rm excess}$ and $\lambda_{\rm turnoff}$ defined by Cieza et al. (2007) and Harvey et al. (2007) and used in many works since. $\lambda_{\rm turnoff}$ is the longest measured wavelength before an excess greater than 80% of the stellar model is observed. If no excess $> 80\%$ is observed, than $\lambda_{\rm turnoff}$ is set to 24 μm. $\alpha_{\rm excess}$ is the slope of the SED at wavelengths longward of

ID	Fitted stellar spectrum	A_V (mag)	L_{star} ($L_\odot$)	$\lambda_{turnoff}$ (μm)	α_{excess}	L_{disk}/L_{star}
2	K7	20.5	1.89	8.0	0.3	0.086
3	K7	0.0	0.14	5.8	-0.5	0.150
5	K7	19.0	0.46	5.8	-1.3	0.083
8	K7	2.9	0.57	5.8	-0.4	0.169
9	A0	7.5	1.46	2.2	0.1	0.205

Table 2.7 SED modelling results for Class II sources

Note. — Table 2.7 is published in its entirety in the electronic edition of the *Astrophysical Journal*. A portion is shown here for guidance regarding its form and content.

ID	Fitted stellar spectrum	A_V (mag)	L_{star} ($L_\odot$)	$\lambda_{turnoff}$ (μm)	α_{excess}	L_{disk}/L_{star}
11	A0	0.0	156.74	8.0	-1.6	0.019
15	K7	1.5	0.79	24.0	···	0.015
17	K7	20.0	0.40	8.0	-1.3	0.006
19	K7	8.1	0.53	24.0	···	0.009
54	K7	4.0	4.66	8.0	-1.0	0.014

Table 2.8 SED modelling results for Class III sources

Note. — Table 2.8 is published in its entirety in the electronic edition of the *Astrophysical Journal*. A portion is shown here for guidance regarding its form and content.

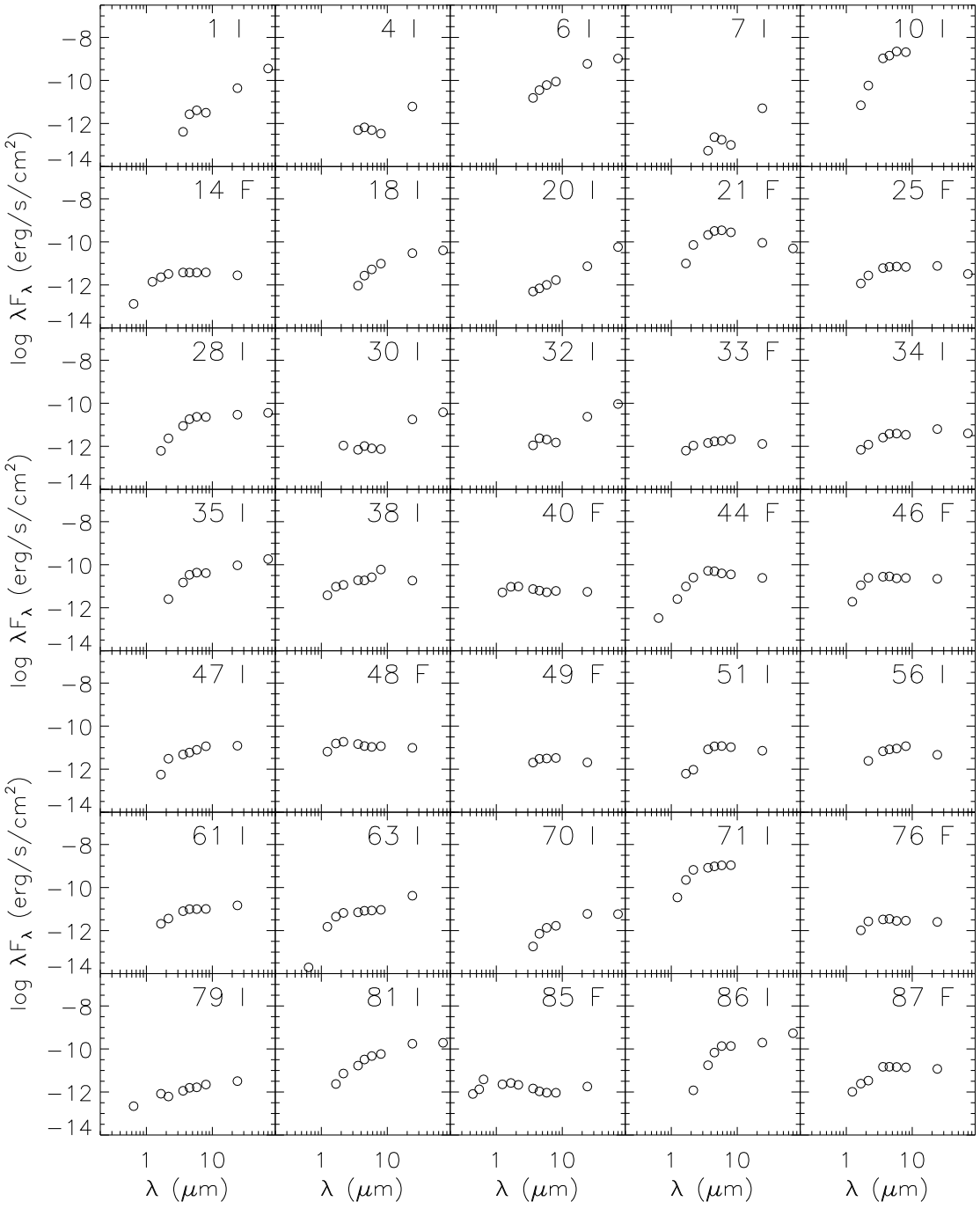

Figure 2.10 SEDs of Class I and Flat sources. The YSO ID, from Tables 2.4 and 2.5, is shown in the upper right of each panel along with the Class (I or F) of the YSO.

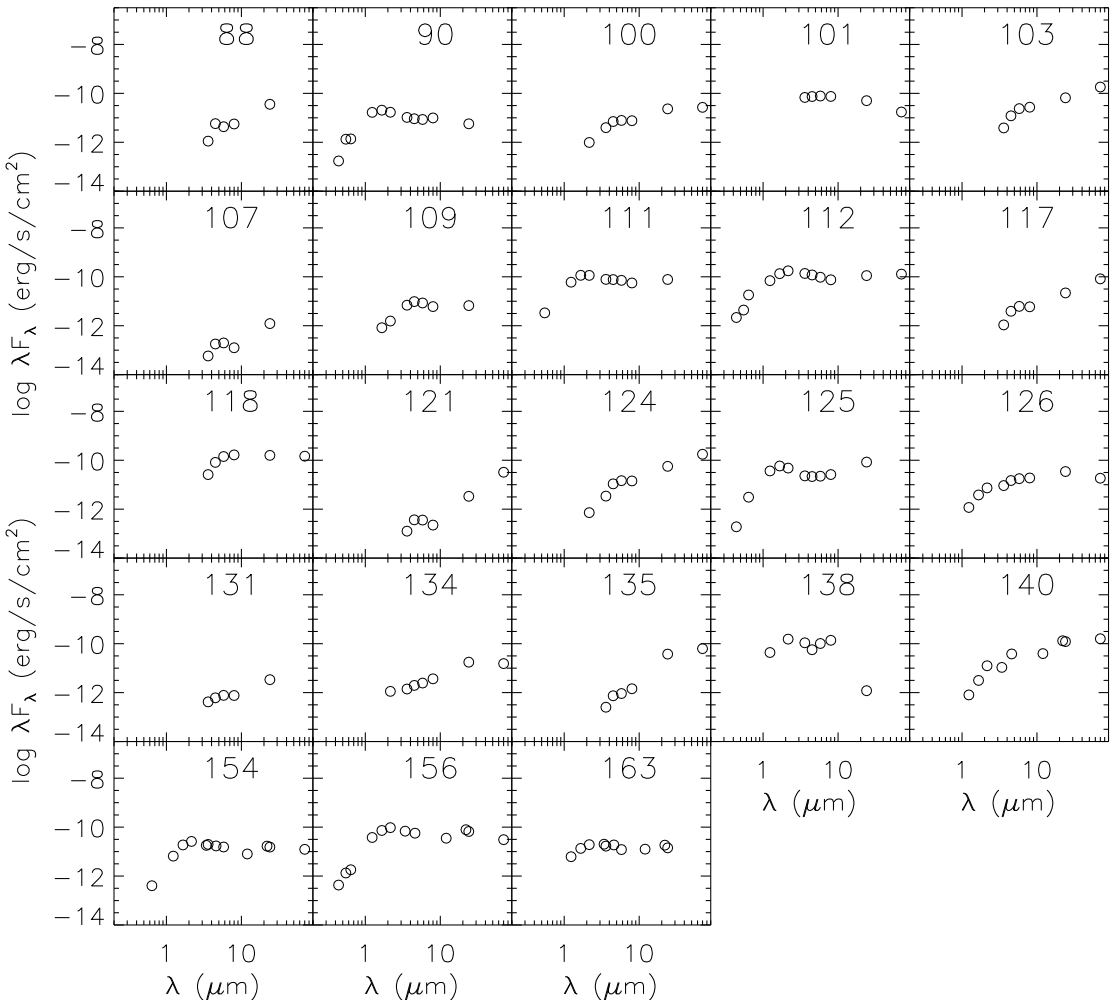

Figure 2.11 SEDs of Class I and Flat sources (continued). The YSO ID, from Tables 2.4 and 2.5, is shown in the upper right of each panel along with the Class (I or F) of the YSO.

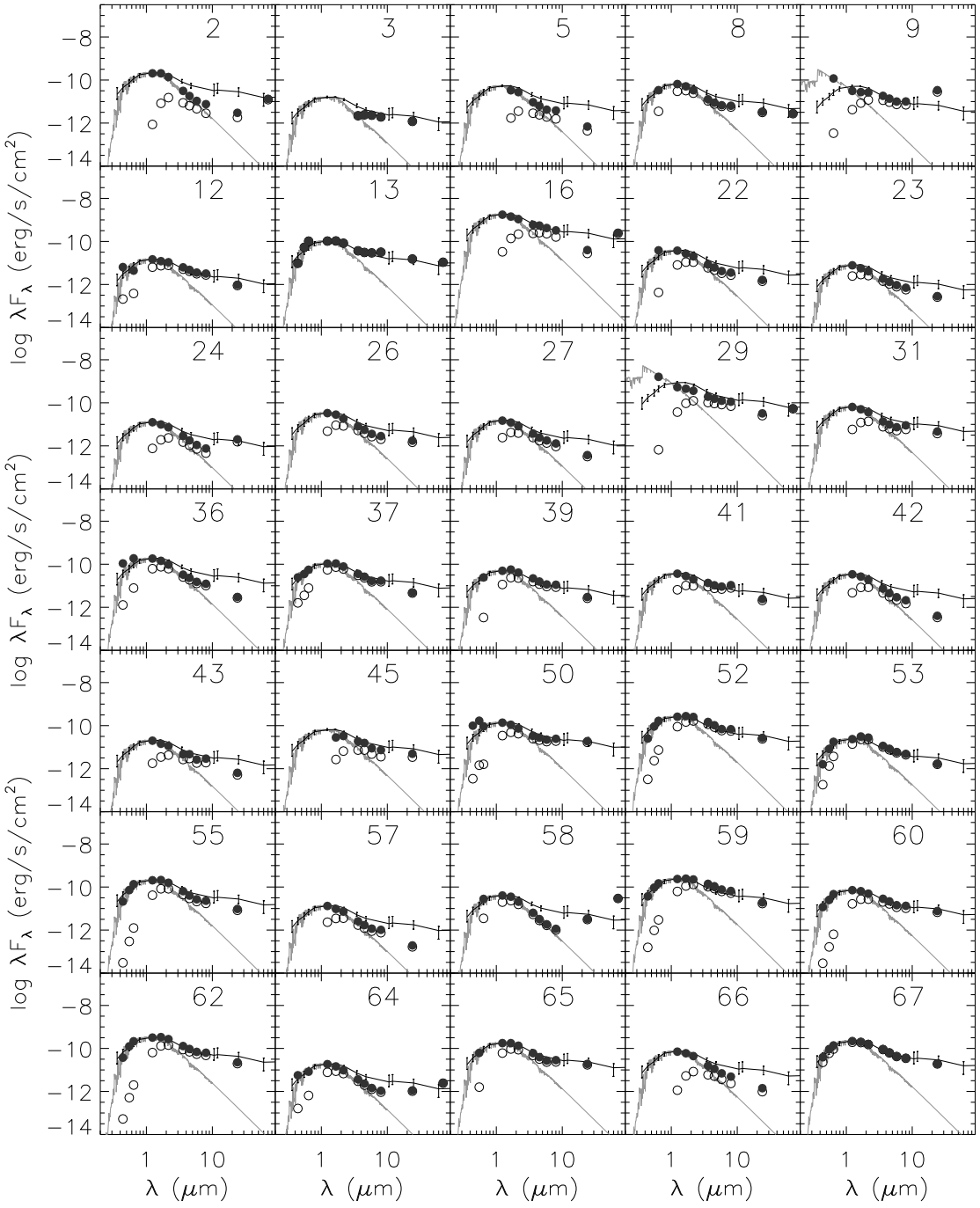

Figure 2.12 SEDs of Class II sources. The YSO ID, from Tables 2.4 and 2.5, is shown in the upper right of each panel. The observed fluxes are plotted with unfilled circles. The de-reddened fluxes are plotted with filled circles. The grey line plots the model stellar spectrum fit to the shorter wavelengths. The black line shows the median SED of T Tauri stars in Taurus (with error bars denoting quartiles of the distribution, D'Alessio et al. 1999) normalized to the B band flux and J band flux of the K7 and A0 stellar spectrum models, respectively.

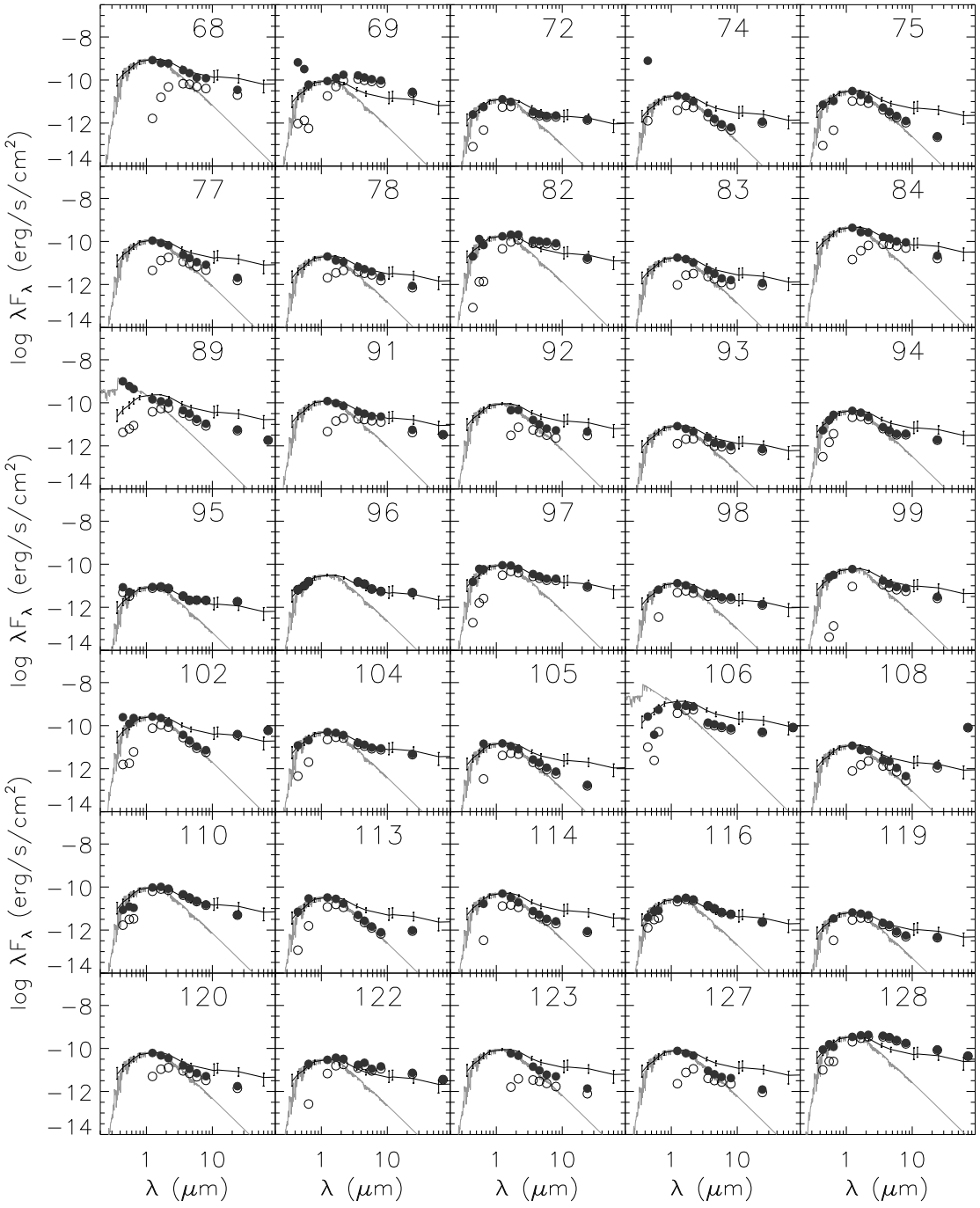

Figure 2.13 SEDs of Class II sources (continued). The YSO ID, from Tables 2.4 and 2.5, is shown in the upper right of each panel. The observed fluxes are plotted with unfilled circles. The de-reddened fluxes are plotted with filled circles. The grey line plots the model stellar spectrum fit to the shorter wavelengths. The black line shows the median SED of T Tauri stars in Taurus (with error bars denoting quartiles of the distribution, D'Alessio et al. 1999) normalized to the B band flux and J band flux of the K7 and A0 stellar spectrum models, respectively.

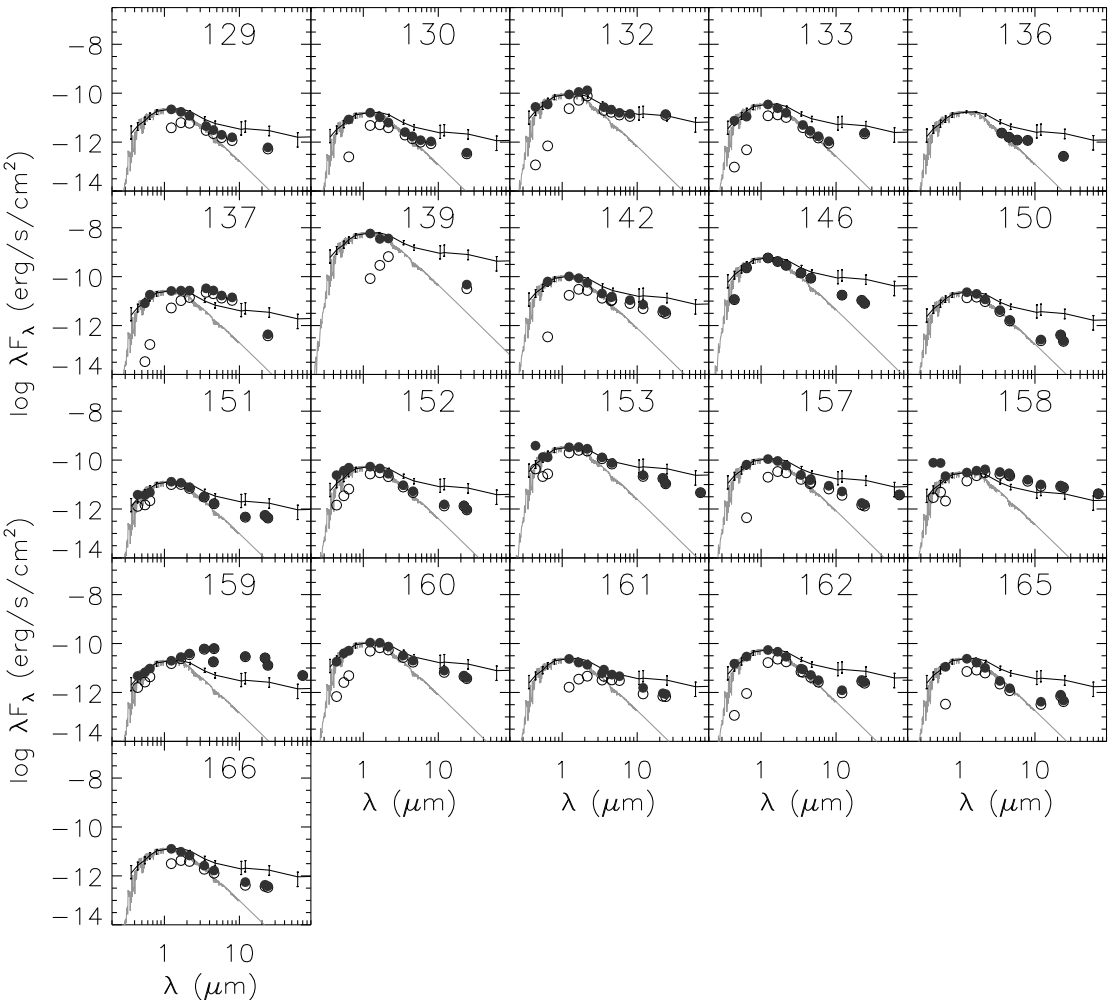

Figure 2.14 SEDs of Class II sources (continued). The YSO ID, from Tables 2.4 and 2.5, is shown in the upper right of each panel. The observed fluxes are plotted with unfilled circles. The de-reddened fluxes are plotted with filled circles. The grey line plots the model stellar spectrum fit to the shorter wavelengths. The black line shows the median SED of T Tauri stars in Taurus (with error bars denoting quartiles of the distribution, D'Alessio et al. 1999) normalized to the B band flux and J band flux of the K7 and A0 stellar spectrum models, respectively.

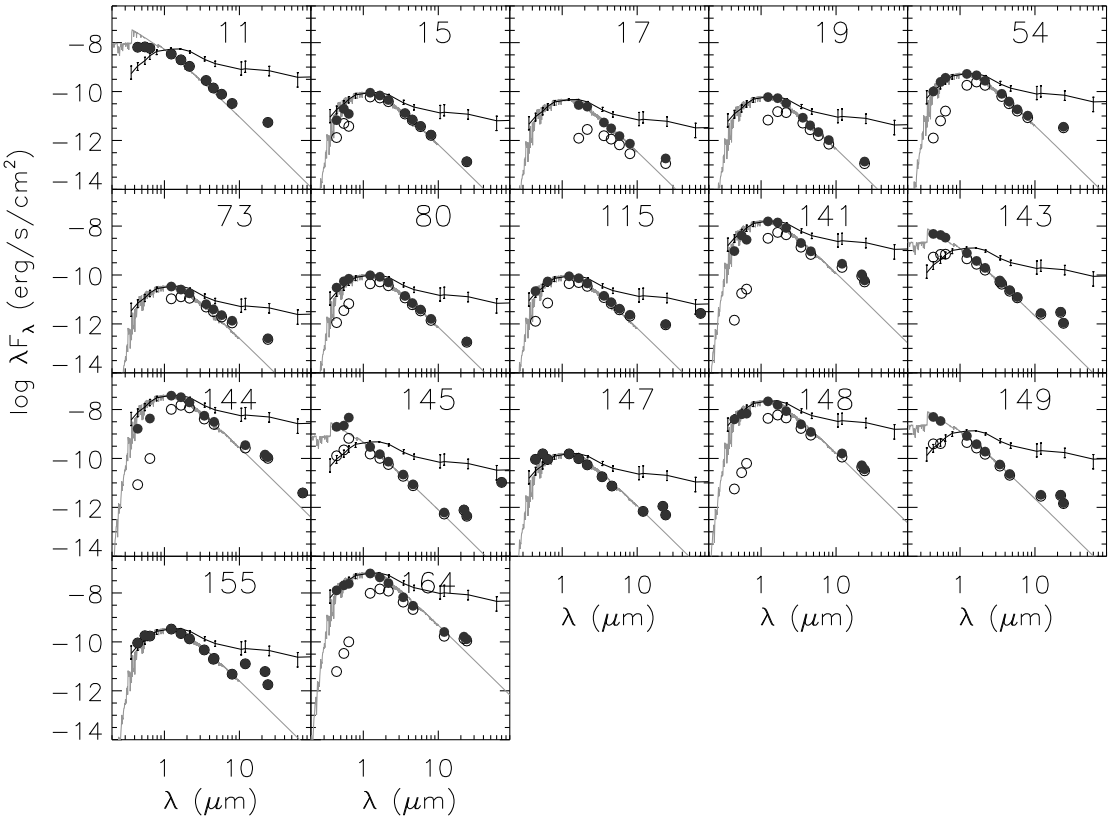

Figure 2.15 SEDs of Class III sources. The YSO ID, from Tables 2.4 and 2.5, is shown in the upper right of each panel. The observed fluxes are plotted with unfilled circles. The de-reddened fluxes are plotted with filled circles. The grey line plots the model stellar spectrum fit to the shorter wavelengths. The black line shows the median SED of T Tauri stars in Taurus (with error bars denoting quartiles of the distribution, D'Alessio et al. 1999) normalized to the B band flux and J band flux of the K7 and A0 stellar spectrum models, respectively.

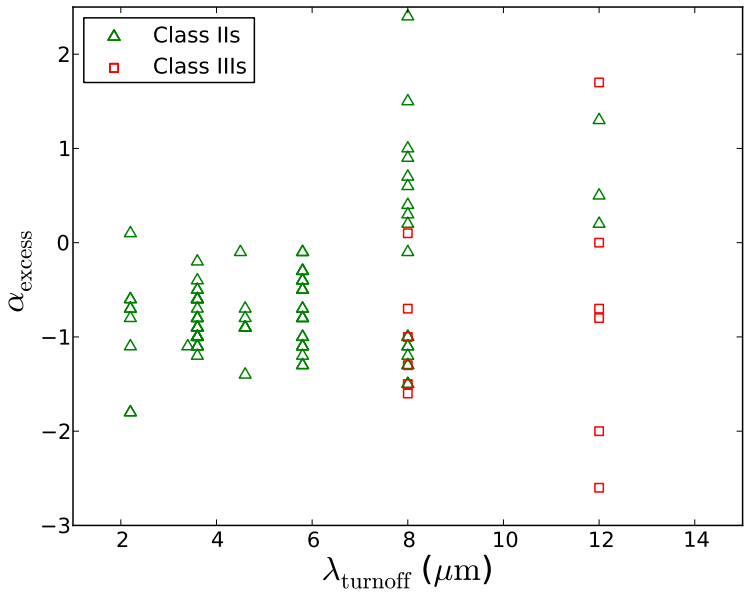

Figure 2.16 Distribution of α_{excess} and $\lambda_{turnoff}$ for Class II and Class III sources. The Class IIIs with $\lambda_{turnoff}$= 24 μm (IDs 15, 19, 80, and 148) are not shown as those sources typically do not have excess measured across a wide enough range to calculate reliable values of α_{excess}.

$\lambda_{turnoff}$. α_{excess} is not calculated for YSOs with $\lambda_{turnoff}$ = 24 μm as there are not enough data points to determine the slope of the excess. These parameters provide a better characterization of the excess since α can include varying contributions from the stellar and dust components.

Figure 2.16 shows the distribution of α_{excess} and $\lambda_{turnoff}$ for the Class IIs and Class IIIs. Class II and Class III YSOs with long $\lambda_{turnoff}$ and positive α_{excess} (YSOs 2, 24, 58, 64, 74, 102, 108, 113, 115, and 133 in the 8 μm bin and YSOs 145, 150, 162, and 165 in the 12 μm bin of Figure 2.16) are good classical transition disk candidates; the lack of near-IR excess but large mid-IR excess is a sign of a deficit of material close to the star within a substantial disk. Cieza et al. (2012) have recently done a study on the transition disks in the AMC, Perseus and Taurus and identify six transition disk candidates in the AMC, three of which are also in our list of candidates (YSOs 58, 102 and 115). Of their remaining candidates, two were debris-like disks (YSOs 11 and 54) and the other was not identified in our YSO list. The larger distribution of α_{excess} for sources with longer $\lambda_{turnoff}$ is consistent with distributions found for other disk populations (e.g., Cieza et al. 2007; Alcalá et al. 2008; Harvey et al. 2008; Merín

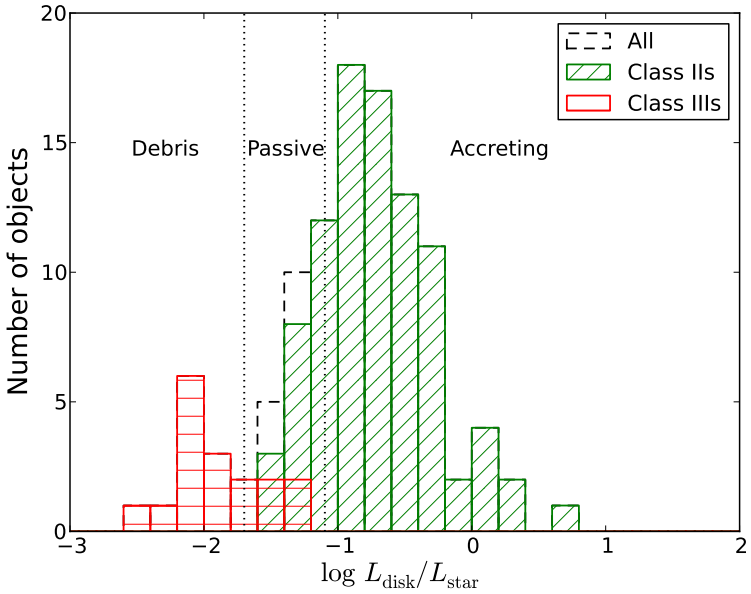

Figure 2.17 The ratio of the disk luminosity to the stellar luminosity for Class II and Class III sources. Also shown are the typical boundaries found for accreting disks, passive disks and debris disks (Kenyon & Hartmann, 1987).

et al. 2008).

2.4.2 Disk luminosities

Figure 2.17 shows the ratio of the disk luminosities to stellar luminosities for the Class II and Class III sources. The disk luminosity is the integral of the observed excesses. (The excess at a given wavelength is calculated by subtracting the flux of the stellar model at that wavelength from the observed flux). The distribution of $L_{\rm disk}/L_{\rm star}$ for Class II and III sources in the AMC is similar to that found for other *c2d* and GB surveys with *Spitzer* (Serpens: Harvey et al. 2007, IC 5146: Harvey et al. 2008, Chameleon II: Alcalá et al. 2008, Lupus: Merín et al. 2008, and the Cepheus Flare: Kirk et al. 2009). We find the Class III sources in the regions typically occupied by sources with passive disks and debris disks (e.g., $0.02 < L_{\rm disk}/L_{\rm star} < 0.08$ for passive disks; Kenyon & Hartmann 1987). The low disk luminosity may be attributable to the lack of mid-IR excess at IRAC wavelengths in these sources' SEDs.

Group	Position (RA, Dec)	$N_{\rm YSO}$	$N_{\rm II}$	$N_{\rm F}$	$N_{\rm I}$	$N_{\rm I+F}/N_{\rm II}$	$R_{\rm eff}$ (pc)	$R_{\rm circ}$ (pc)	Aspect Ratio	Mean Surf. Dens. (pc^{-2})
1[a]	67.562286, 35.239391	49	34	7	8	0.44	0.99	1.22	1.52	15.8
2	67.610970, 35.770126	23	12	7	4	0.92	0.55	1.23	5.01	24.1
3	67.671758, 35.541806	12	9	0	3	0.33	0.66	0.74	1.26	8.55
4	67.188288, 36.440921	10	4	1	5	1.5	0.48	0.69	2.03	13.3
5	67.708443, 34.958037	8	3	0	5	...	...	...	...	...
6	62.662345, 38.094258	6	5	0	1	...	...	...	...	...
7	62.525460, 40.037669	5	2	0	3	...	...	...	...	...

Table 2.9 AMC Groups Summary

[a]Several known members near LkHα 101 are missing in our YSO list, affecting the values reported for this group.

2.4.3 Questionable Class III sources

It is possible that some of the Class III sources identified here are field giants. Oliveira et al. (2009) followed up on 150 *Spitzer* identified YSOs in Serpens and obtained 78 optical spectra with sufficient signal-to-noise. They showed that there were at least 20 giant contaminants in this list, 18 of which were identified as Class III sources. The more scattered spatial distribution of Class IIIs throughout the AMC is consistent with this idea that they are contaminants. Additionally, five of our Class III objects (YSOs 11, 141, 144, 148, 164) have very high luminosities (> 100 L$_\odot$). Four of these objects (YSOs 141, 144, 148, 164), as well as YSO 149 which is not of particularly high luminosity, are quite removed from the areas of high extinction towards the AMC (see Figure 2.18 in the following section) and regions of low column density ($N_{\rm H2} < 5 \times 10^{21}$ cm^{-2}, see § 2.3.1).

2.5 Spatial Distribution of Star Formation

The spatial distribution of IRAC/MIPS-identified YSOs by class is shown in Figure 2.18. A close-up of the region surrounding the LkHα 101 cluster and the cluster extension along the filament is also included so the relatively densely clustered YSOs can be better distinguished. Figure 2.18 shows that the bulk of star formation in the AMC has been concentrated in this southern region of the cloud; the majority of the identified YSOs (79%) are in this area. (Note that the number of YSOs in that region is a lower limit as it is likely that a significant number of YSOs in the LkHα 101 region are not identified, see discussion at the end of § 2.3.1.)

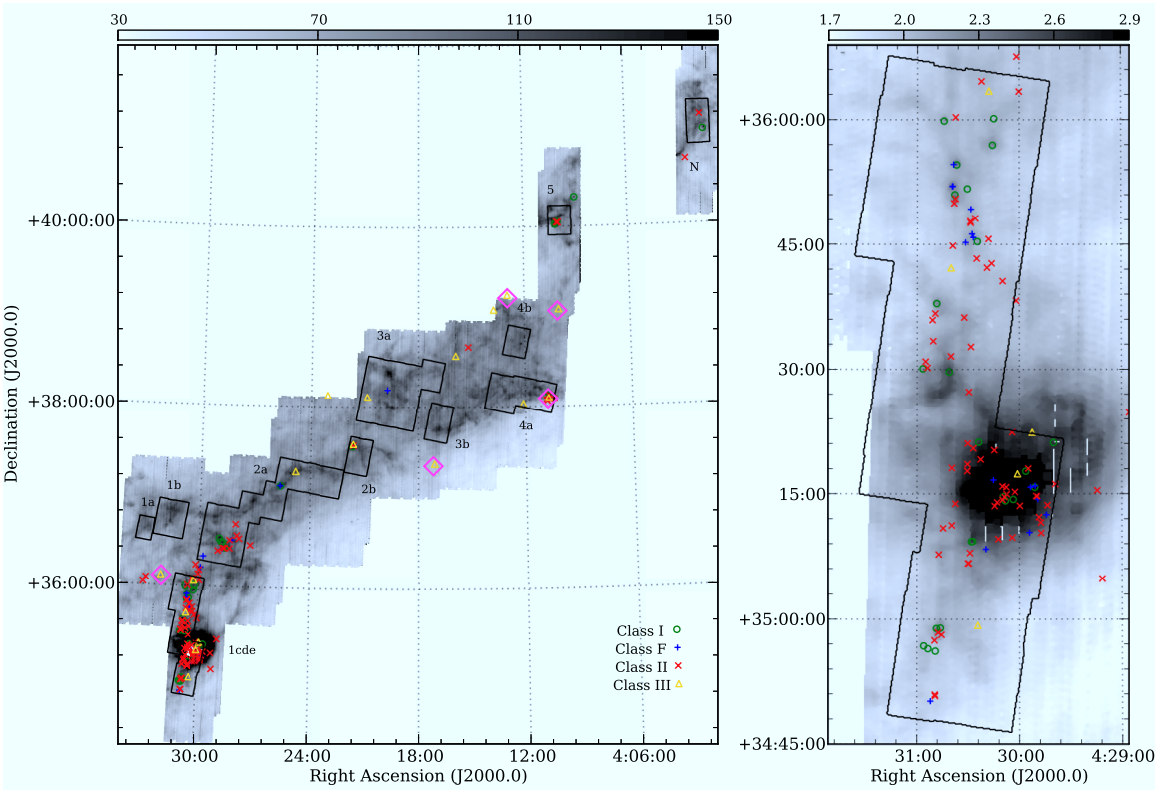

Figure 2.18 Left: The positions of YSOs and IRAC fields in Auriga. The greyscale is the MIPS 160 μm map (colorbar units are MJy sr^{-1}) and the YSOs are marked according to their classification: green circles denote Class Is; blue +s denote Class Fs; red $\times$s denote Class IIs; yellow triangles denote Class IIIs. The magenta diamonds mark the Class III sources of high luminosities that are likely contaminants (see § 2.4.3). IRAC fields are outlined in black and labelled. (Note that some YSOs fall beyond the 160 μm coverage because it is slightly offset from the 24 μm coverage that is used for YSO identification.) Right: Close-up of the region around LkHα 101. The greyscale is the log (base 10) of the flux (colorbar units are log(MJy sr^{-1})). The centre of the field is entirely saturated. As is evident, there are some YSOs outside the IRAC coverage area. This list of MIPS-only YSOs has been trimmed by using WISE data to remove more objects that are likely background galaxies.

2.5.1 Identification of YSO groups

We performed a clustering analysis on the identified Class I, F, and II sources in the AMC to identify the densest regions of YSOs and the largest groups. The details of the analysis are described in Masiunas et al. (2012). We omit the Class III sources from the analysis to avoid the risk of including field giants (see for example § 2.4.3). We performed a minimum spanning tree (MST) analysis to identify groups of YSOs within the region. This analysis connects YSOs by the minimum distance to the next YSO to form a "branch" (Cartwright & Whitworth, 2004). Figure 2.19 shows the cumulative distribution function (CDF) of the branch lengths between YSOs. This is used to determine the MST critical branch length, L_{crit}, that defines the transition between the branch lengths in the denser regions to the branch lengths in the sparser regions (Gutermuth et al., 2009). Therefore L_{crit} is based on relative over densities of objects. We measure an L_{crit} of $210''$ for the AMC. Group memberships are defined by members which are all connected by branches of lengths less than L_{crit}. The boundary of a group is defined where the branch length between adjacent sources exceeds L_{crit}. Figure 2.20 shows that we have extracted four groups with 10 or more members (marked by colored convex hulls) and three groups with 5–9 members (marked with magenta circles). Table 2.9 lists the properties of these groups. The position of the group is given by its geometric center. The group's effective radius, $R_{\rm eff}$, defines the radius of a circle with the same area as the convex hull containing the group members. The maximum radial distance to a member from the median position gives $R_{\rm circ}$, therefore a circle with this radius would contain all group members. Finally, the elongation of the group is determined by comparing $R_{\rm circ}$ to $R_{\rm eff}$ and represented by the aspect ratio, ${R_{\rm circ}}^2/{R_{\rm eff}}^2$. The MST analysis on the full cloud recovers the clustering surrounding LkHα 101. The cluster subtends a larger area than that measured in Gutermuth et al. (2009) confirming their claim that there was star formation extended beyond their field of view. The star formation is mostly extended along the North-South direction of the cluster and therefore we measure a more elongated group than measured by Gutermuth et al. (2009). This is still the largest group in the AMC in terms of area and the number of members.

As discussed in § 2.3.1, our analysis is likely to have underestimated the number of YSOs in the region around LkHα 101. To check the consistency of our analysis with Gutermuth et al. (2009), we ran the MST analysis on both YSO lists within the Gutermuth et al. (2009) area of 4-channel IRAC coverage. This leaves us with 41

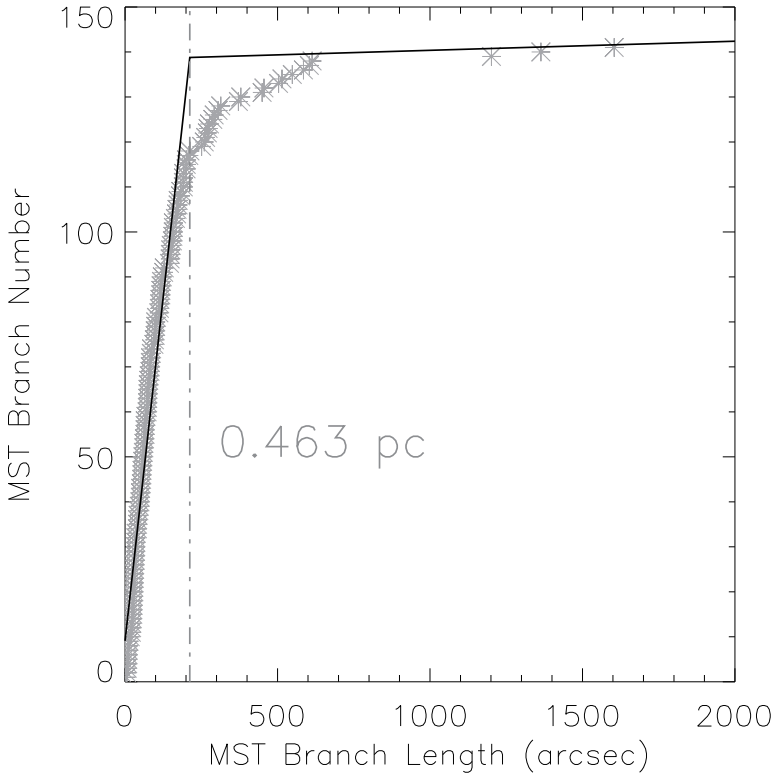

Figure 2.19 Cumulative distribution function (CDF) of MST branch lengths (asterisks). The solid lines represent linear fits to each end of the CDF. The dot-dash line marks L_{crit} where the solid lines meet. The solid lines follow the CDF in the dense regions (steep line) and the sparser regions (shallow line).

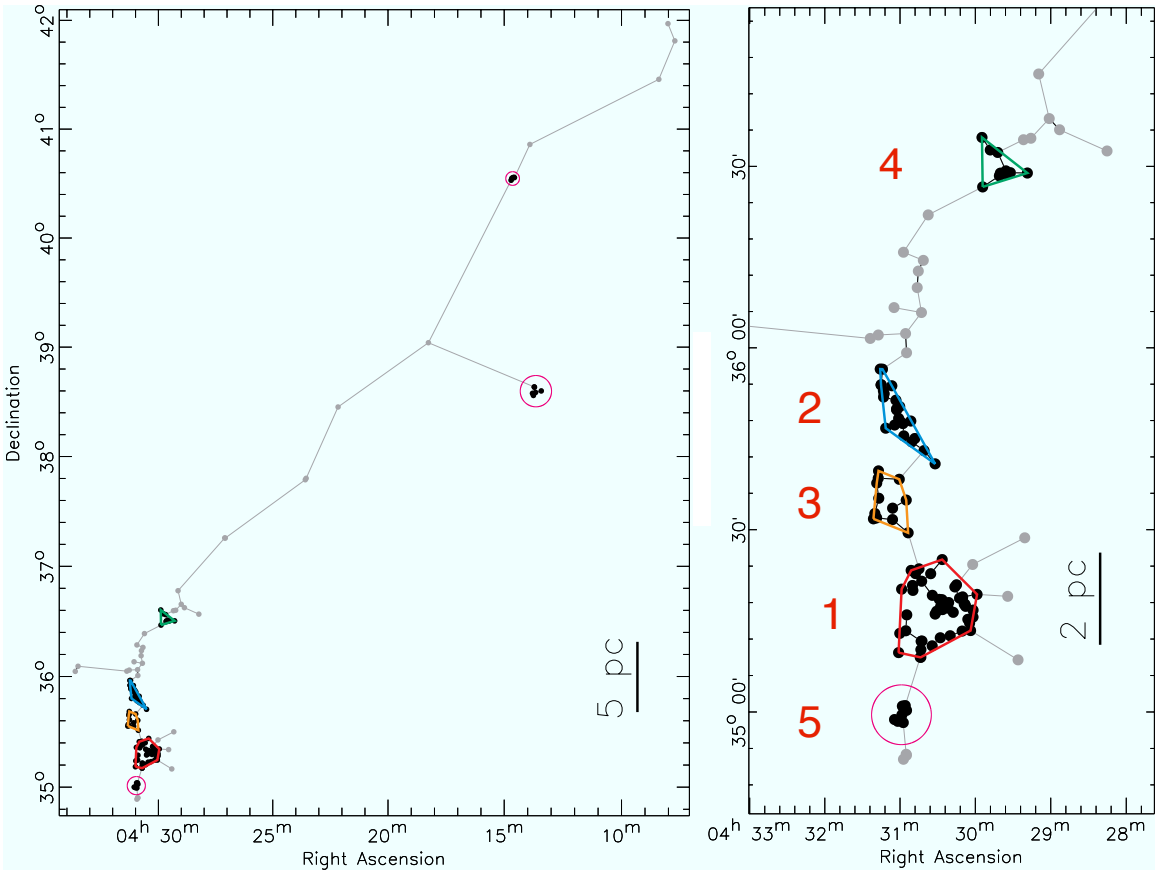

Figure 2.20 We extract four groups with 10 or more members (colored convex hulls) and three groups with 5–9 members (magenta circles) using an MST analysis. The right hand panel shows the enlarged southern region of the cloud where most of the groups are located. The red numbers adjacent to the groups correspond to the group number listed in Table 2.9.

of the YSOs presented here and 102 of those presented in Gutermuth et al. (2009). (There is one bright YSO in Gutermuth et al. 2009 that lies just outside their 4-channel IRAC coverage to the south. It was only observed at IRAC1 and IRAC3.) We get an L_{crit} of 120″ for our cropped list of YSOs and an L_{crit} of 73″ for the cropped Gutermuth et al. (2009) YSO list. (Note that running the analysis on the cropped field, which is dense compared to the rest of the cloud, yields a smaller L_{crit} than when the analysis is run on the whole cloud. This is expected as L_{crit} is based on over densities, as discussed above.) The ratio of the L_{crit} values for the two YSO lists ($73/120 = 0.61$) agrees with our expectation that it should scale with the square-root of the density, and hence the cropped YSO count ($\sqrt{102/41} = 0.63$). Therefore we report that the derived properties are consistent with those measured by Gutermuth et al. (2009). (Differences are expected as shown by Gutermuth et al. (2009) with their comparisons among several shared regions.) However, the missing YSOs at the centre of the cluster complicate any further comparison their results.

2.5.2 Comparison of grouped and non-grouped YSOs

We find 76% (113 of the 149) of the Class Is, Class Fs, and Class IIs are found in groups. Rather than compare the class fractions, given by $N_{\rm I+F}/N_{\rm II}$ in Table 2.9, we directly compare the underlying distribution of α to determine whether the distribution of YSOs within groups is consistent with the whole cloud. We get the same result for each group: a KS test on the α distribution of the group and the α distribution of the whole cloud shows that we cannot reject the hypothesis that they are drawn from the same sample (p-values > 0.13). (We also did a KS test for each group with the extended population and found the same result.)

Similarly, we compared the properties of disks within groups and those not in groups by performing a KS test on the distributions of disk luminosities (p-value of 0.08), $\alpha_{\rm excess}$ (p-value of 0.9), and $\lambda_{\rm turnoff}$ (p-value of 0.9) and find no evidence that the two populations are drawn from different parent populations.

2.6 Summary

We observed the AMC with IRAC and MIPS aboard the *Spitzer Space Telescope* and identify 138 YSOs in the cloud. As our IRAC coverage is segmented, we complemented our more contiguous MIPS coverage with WISE data to further eliminate

galaxies from the sample, leaving 28 MIPS-only YSOs remaining, bringing the total number of YSOs in the AMC to 166. We classified the YSOs based on the spectral slope of their SEDs between 2 μm and 24 μm and find 37 Class I objects, 21 Class F objects (flat spectrum sources), 91 Class II objects, and 17 Class III objects. The high fraction of Class Is and Class Fs suggests that the AMC is relatively unevolved compared to other star-forming clouds. Despite the similarity in cloud properties between the AMC and the OMC, there is a distinct difference in the star formation properties. The star formation in the AMC is also concentrated along its filament, however, it is also forming a factor of about 20 fewer stars than the OMC. Lada et al. (2009) find that there is much less material at high density in the AMC than in the OMC and attribute the difference in star formation to this. Further studies of the star formation and YSO population in the AMC are needed to highlight the differences of the two clouds given their similar age.

We modelled the SEDs of the Class II and Class III sources and their excesses by first fitting a K7 stellar spectrum to the optical and near-IR fluxes. The spectrum is normalized to the 2MASS flux (or the IRAC1 flux when 2MASS is unavailable) and we use an A_V value to match the spectrum of the stellar model to the de-reddened observed optical fluxes. An A0 stellar spectrum is used in the eight cases where a K7 spectrum is unable to provide a reasonable fit. Fitting a stellar spectrum allows us to measure the disk luminosities and characterize the excess. The excesses of the Class II and Class III sources were further parameterized by $\lambda_{\rm turnoff}$, the longest wavelength before an excess greater that 80% is measured, and $\alpha_{\rm excess}$, the slope of the SED at wavelengths longward of $\lambda_{\rm turnoff}$. $\lambda_{\rm turnoff}$ is a useful tracer for the proximity of dust to the star and consequently we identify fourteen classical transition disk candidates.

The bulk of the star formation in the AMC is in the southern region of the cloud. We included a clustering analysis to quantify the densest areas of star formation and to identify groups within the cloud. We find four groups with 10 or more members all in the region around LkHα 101 and its adjoining filament. We find three smaller groups with 5 – 9 members scattered throughout the cloud. The largest group is that around LkHα 101 and contains 49 members. We note that there are likely even more YSOs in this group since our YSO identification criteria of S/N $\geq$ 3 in IRAC1-4 and MIPS1 are difficult to attain in this bright region.

Acknowledgements

We thank the referee whose comments and suggestions greatly helped improve the paper and its clarity. H.B.F gratefully acknowledges research support from an NSERC Discovery Grant. This research made use of APLpy, an open-source plotting package for Python hosted at http://aplpy.github.com This research made use of Montage, funded by the National Aeronautics and Space Administration's Earth Science Technology Office, Computation Technologies Project, under Cooperative Agreement Number NCC5-626 between NASA and the California Institute of Technology. Montage is maintained by the NASA/IPAC Infrared Science Archive.

Chapter 3

The JCMT Gould Belt Survey: A first look at the Auriga-California Molecular Cloud with SCUBA-2

Originally submitted to the Astrophysical Journal with a response from the referee recieved.

Authors: H. Broekhoven-Fiene, **B.C. Matthews**, **P. Harvey**, **M. Chen**, **J. Lane**, **M.J. Currie**, **H. Kirk**, **K. Pattle**, **J. Buckle**, **D. Johnstone**, **J. Di Francesco**, **E. Drabek-Maunder**, D.S. Berry, M. Fich, J. Hatchell, T. Jenness, J.C. Mottram, D. Nutter, J.E. Pineda, C. Quinn, C. Salji, S. Tisi, M.R. Hogerheijde, D. Ward-Thompson, P. Bastien, D. Bresnahan, H. Butner, A. Chrysostomou, S. Coude, C.J. Davis, A. Duarte-Cabral, J. Fiege, P. Friberg, R. Friesen, G.A. Fuller, S. Graves, J. Greaves, J. Gregson, W. Holland, G. Joncas, J.M. Kirk, L.B.G. Knee, S. Mairs, K. Marsh, G. Moriarty-Schieven, C. Mowat, J. Rawlings, J. Richer, D. Robertson, E. Rosolowsky, D. Rumble, S. Sadavoy, H. Thomas, N. Tothill, S. Viti, G.J. White, C.D. Wilson, J. Wouterloot, J. Yates, M. Zhu,

ABSTRACT

We present 850 μm and 450 μm observations of the Auriga-California molecular cloud using SCUBA-2 as part of the JCMT Gould Belt Legacy Survey to identify candidate protostellar objects, measure the masses of their circumstellar material (disk and envelope), and compare the star formation to that in the Orion A molecular cloud. We identify 36 candidate protostars based on the presence of compact submillimeter emission, complementing these observations with existing *Herschel*/SPIRE maps. Of our candidate protostars, 18 are associated with young stellar objects (YSOs) in the *Spitzer* and *Herschel*/PACS catalogs of 166 and 60 YSOs, respectively (177 unique), confirming their protostellar nature. The

remaining 18 candidate protostars are in regions, particularly around LkHα 101, where the background cloud emission is too bright to verify or rule out the presence of compact 70 μm emission expected for a protostellar source. We keep these candidate protostars in our sample but note that they may indeed be prestellar in nature. Our observations are sensitive to the high end of the mass distribution in Auriga-Cal. We find that the disparity between the richness of infrared star forming objects in Orion A compared to the sparsity in Auriga-Cal extends to the submillimeter, suggesting that the relative star formation rates have not varied over the Class II lifetime and that Auriga-Cal will maintain a lower star formation efficiency.

3.1 Introduction

The Auriga-California Molecular Cloud (Auriga-Cal) is a nearby (450 $\pm$ 23 pc: Lada et al. 2009) giant molecular cloud, notable for its relatively quiescent star formation in contrast to the Orion A Molecular Cloud. Auriga-Cal was first identified as a contiguous cloud and located in the Gould Belt by Lada et al. (2009), who also noted that despite Auriga-Cal and Orion A sharing a similar filamentary morphology as well as similar mass ($\sim 10^5 M_\odot$), spatial scale (80 pc), and distance (i.e., similar physical characteristics and no drastic observational bias), Auriga-Cal appeared to have much less ongoing star-formation. Lada et al. attributed this deficit of star formation to the lower mass of the cloud at high density ($\sim$ an order of magnitude). The *Spitzer* Survey of Interstellar clouds (P.I. L. Allen) extended the area of Auriga-Cal surveyed by *Spitzer* beyond just the young stellar cluster region NGC 1529 around LkHα 101 (observed by Gutermuth et al. 2009, hereafter G09) to confirm this deficit with a census of the young stellar object (YSO) population throughout the cloud. This census showed that Auriga-Cal contains 16-20 times fewer *Spitzer*-identified YSOs than Orion A (Broekhoven-Fiene et al. 2014; hereafter BF14). Combined with Auriga-Cal's single early B-star, LkHα 101, in contrast to Orion A's dozens of OB stars, star formation in Auriga-Cal appears more like that in lower mass clouds like Taurus and Ophiuchus. The classification of the YSOs reveals a high fraction of Class I and F (Flat spectrum) YSOs (associated with early, short-lived stages of star formation) suggesting that Auriga-Cal itself is in an earlier evolutionary stage (BF14). An H-R diagram analysis of the LkHα 101 cluster alone (where it is difficult to measure the infrared Class ratios due to the bright emission around LkHα 101) suggests the majority of individual YSOs have ages < 3 Myr with a median age of 1 Myr (Wolk et al., 2010). This situation makes Auriga-Cal an interesting target in which to study both YSOs and cloud properties at early evolutionary stages. Harvey et al. (2013) observed Auriga-Cal with the *Herschel* Space Observatory to map the large-scale structure with PACS (70 μm and 160 μm) and SPIRE (250 μm, 350 μm, and

500 μm) instruments and identify Class 0/I YSOs with *Herschel*/PACS. In this work, we focus on the protostellar objects (YSOs) evident in submillimeter observations.

We present the first results from observations of Auriga-Cal taken with the Submillimetre Common-User Bolometer Array-2 (SCUBA-2: Holland et al. 2013) on the James Clerk Maxwell Telescope (JCMT). These data are part of the JCMT Gould Belt Legacy Survey (GBS: Ward-Thompson et al. 2007) to observe nearby star-forming regions (within 500 pc) and trace the earliest stages of star formation. We also include previously unpublished ^{12}CO J=3-2 observations (PI Matthews: Program IDs M09BC16 and M10BC09) taken with the Heterodyne Array Receiver Programme (HARP). In this work, we describe the observations and data reduction in Section 3.2. In Section 3.3, we describe the source extraction (Section 3.3.1) to identify compact sources associated with protostellar objects and isolate them from larger structures such as cloud emission and clumps. We also describe the measurement of fluxes (Section 4.2.3) and compare our source catalog with *Spitzer* and *Herschel*/PACS YSO catalogs (Section 3.3.4) to identify previously unknown young objects (Section 3.3.5). We use the submillimetre emission to measure the masses of YSOs (Section 3.3.6) and compare the population of embedded candidate YSOs in Auriga-Cal to that in Orion A to investigate the recent relative star formation rates between the two clouds. We summarize our conclusions in Section 3.4.

3.2 Observations and Data Reduction

3.2.1 SCUBA-2

Continuum observations at 850 μm and 450 μm were made using fully sampled 30$'$ diameter circular regions, referred to as "pongs", (PONG1800 mapping mode; Kackley et al. 2010) between July 2012 and January 2015. Larger regions were mosaicked with overlapping scans. The reduced data presented here are from the GBS Legacy Release 1 of the GBS data reduction team (Mairs et al., 2015). Six different pong regions were observed, as shown in Figure 3.1. Only the densest areas of the cloud are observed, as the GBS used a column density threshold of $A_V > 1$ to select mapping areas. This results in a more piecemeal coverage of wispier clouds such as Auriga-Cal. The exception to this is the AUR_Central-N region which was added to the survey in January 2015 when the management of the JCMT by the Joint Astronomy Centre was coming to a close and the legacy surveys were nearing completion. Extra regions that could be observed in Band 2 weather were submitted so the JCMT would not be idle were there no other higher priority legacy survey regions visible. We submitted the AUR_Central-N regions as it contained one of the few groups of YSOs identified with *Spitzer* (BF14) not already included in the survey coverage. Regions within

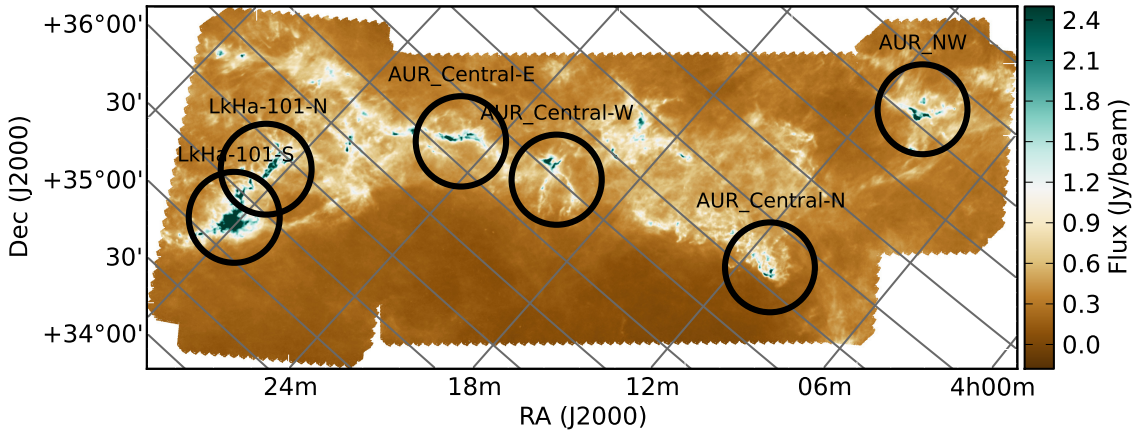

Figure 3.1 SCUBA-2 observed regions in Auriga-Cal. Circles marking the area observed by SCUBA-2 (and labelled according to their observation name) are overlaid on the *Herschel* 500 μm map from Harvey et al. 2013 to illustrate the locations throughout the cloud that were observed. The highest column density regions were targeted and the LkHα 101 pongs, which cover the part of the cloud with the densest area of star formation, were prioritized to be observed in the best weather (Band 1). For optimal display of the entire cloud, the celestial coordinates are tilted, i.e., North is not up as it is for Figure 3.2.

the GBS are prioritized such that the highest priority regions (those with $A_V > 3$) are observed in Band 1 ($\tau_{225\mathrm{GHz}} < 0.05$), the best weather conditions, to have better 450 μm sensitivity, with other regions observed in Band 2 weather ($0.05 < \tau_{225\mathrm{GHz}} < 0.08$). The LkH$\alpha$ 101 pongs in the southern end of the cloud were prioritized for Band 1 observations. As this region of the cloud has higher density material, it unsurprisingly is the richest area in the cloud in terms of previously identified YSOs. Band 1 regions are observed with four repeats each and regions observed in Band 2 weather have six repeats each (except AUR_Central-N, which has 5 repeats). The 450 μm and 850 μm maps of each region are shown in Figure 3.2.

The data were reduced using an iterative map-making technique (makemap in SMURF; Chapin et al. 2013), and gridded to 3″ pixels at 850 μm and 2″ pixels at 450 μm. The iterations were halted when the map pixels, on average, changed by <0.1% of the estimated map rms. The initial reductions of each individual scan were coadded to form a mosaic from which a signal-to-noise ratio (SNR) mask of SNR > 3 was produced for each region at 850 μm, which was then smoothed and rethresholded in an attempt to bridge nearby areas of bright emission likely containing emission. This better determines the locations of the fainter emission as the coadded mosaic of multiple songs has higher a SNR and is sensitive to fainter emission than the individual pongs. The final mosaic was produced from a second reduction using this mask for both 850 μm and 450 μm maps to define areas of emission. Detection of emission structure and calibration accuracy are robust within the

masked regions, and are uncertain outside of the masked region. Any astronomical signal which may be outside the mask, although real, may likely be underestimated in flux and size. The mask used in the reduction can be seen in the quality array in the reduced datafile and is shown in Figure 3.2.

A spatial filter of $600''$ is used in the reduction, which means that flux recovery is robust for sources within the masked region and with a Gaussian FWHM less than $2.5'$. Sources between $2.5'$ and $7.5'$ will be detected, but both the flux and the size are underestimated because Fourier components with scales greater than $5'$ are removed by the filtering process. Detection of sources larger than $7.5'$ is dependent on the mask used for reduction (see Mairs et al. 2015).

The data are calibrated in mJy/arcsec^2, using aperture flux conversion factors of 2.34 Jy/pW/arcsec^2 and 4.71 Jy/pW/arcsec^2 at 850 μm and 450 μm, respectively, derived from average values of JCMT calibrators (Dempsey et al., 2013), and correcting for the pixel area. The pong scan pattern leads to lower noise in the map centre and overlap regions, while data reduction and emission artifacts can lead to small variations in the noise over the whole map.

The typical pixel-to-pixel noise level in the 850 μm maps is 0.05 mJy/arcsec^2. The noise level varies more for 450 μm, which is more sensitive to the different conditions in which the data were taken (for example weather conditions and extended observing), but is typically 1 mJy/arcsec^2. It is twice that for AUR_Central-N (2.2 mJy/arcsec^2) and slightly lower (0.7 mJy/arcsec^2) for LkHa-101-S. The detected emission (Figure 3.2) shows filamentary structure reminiscent of the large-scale structure observed with Herschel/SPIRE (Harvey et al., 2013). There are some locations in the map, particularly near LkHα 101, with negative bowling around bright emission. This artifact occurs when the boundary of the external mask, which forces the flux to go to zero at the edge where it meets the noise level, does not contain all of the true emission. Any future work on the larger scale cloud emission will need a more appropriate mask to recover such emission. The mask used in this work, however, is sufficient for recovering compact sources. Reductions testing different external masks for the JCMT GBS showed that the flux of a compact source, measured with aperture photometry, is consistent between reductions as the increase in recovered large-scale emission is accounted for with the sky aperture. We continue our analysis, which is focused on the compact sources in Auriga-Cal associated with YSOs, with the standard external mask described above.

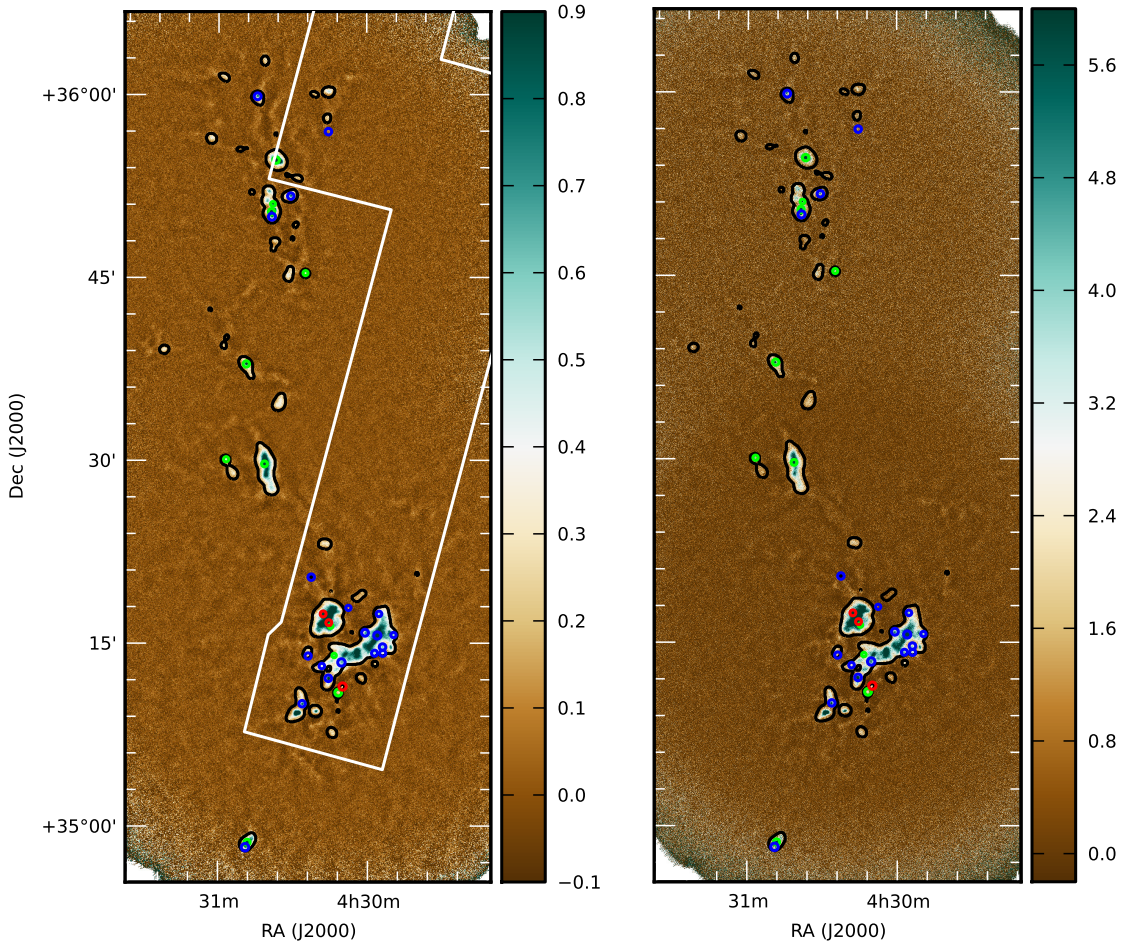

Figure 3.2 Maps of LkHα 101 at 850 μm (left) and 450 μm (right). Blue, red, and green circles mark identified candidate YSOs at 450 μm, 850 μm, or both, respectively, with circle size corresponding to the extracted source size (see Section 3.3.1). The ^{12}CO J=3-2 coverage is outlined in white. (Note, that some of the noisy map edges are visible in the area displayed.)

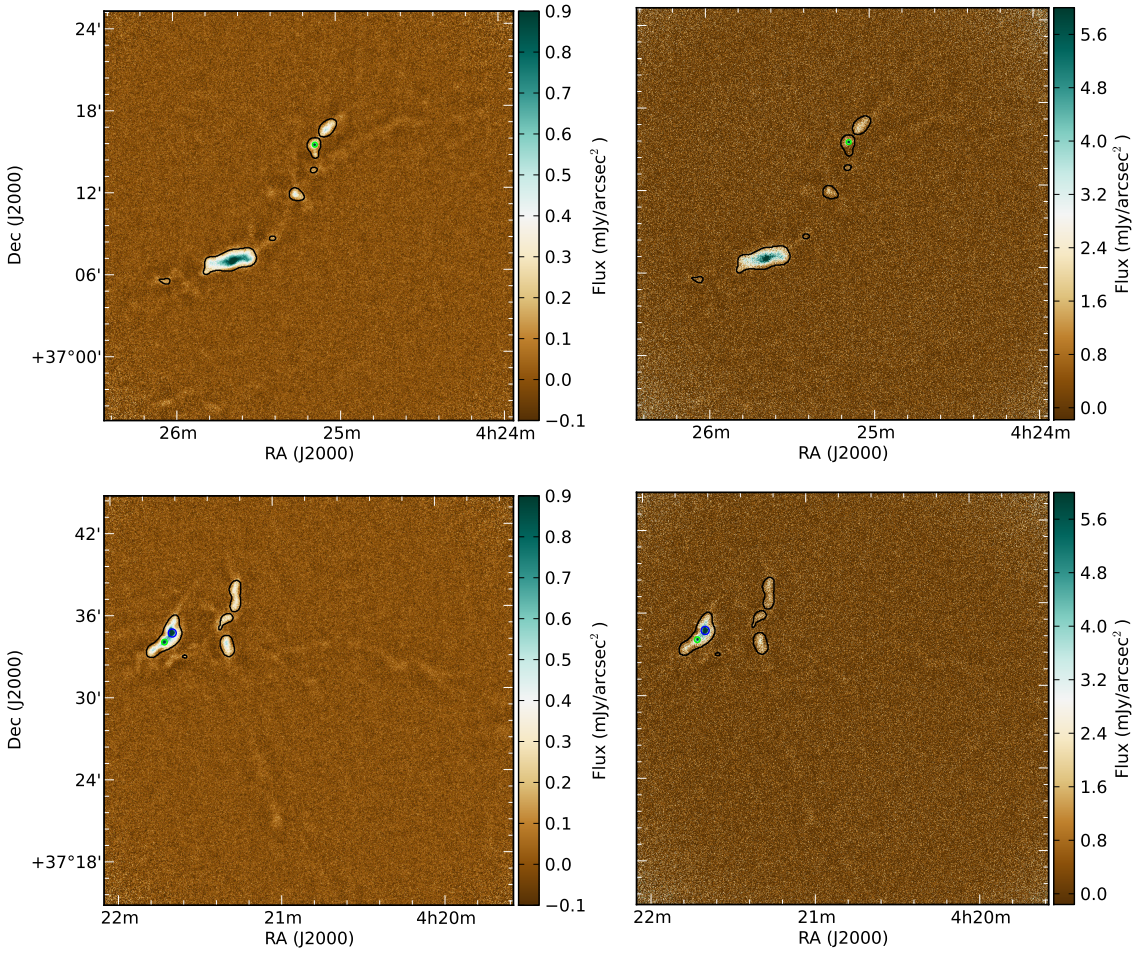

Figure 3.2 *continued*. Maps of AUR_Central-E (top) and AUR_Central-W (bottom) regions at 850 μm (left) and 450 μm (right). Some faint filamentary structure is visible and matches that seen in *Herschel* 500 μm maps (c.f. Figure 3.1).

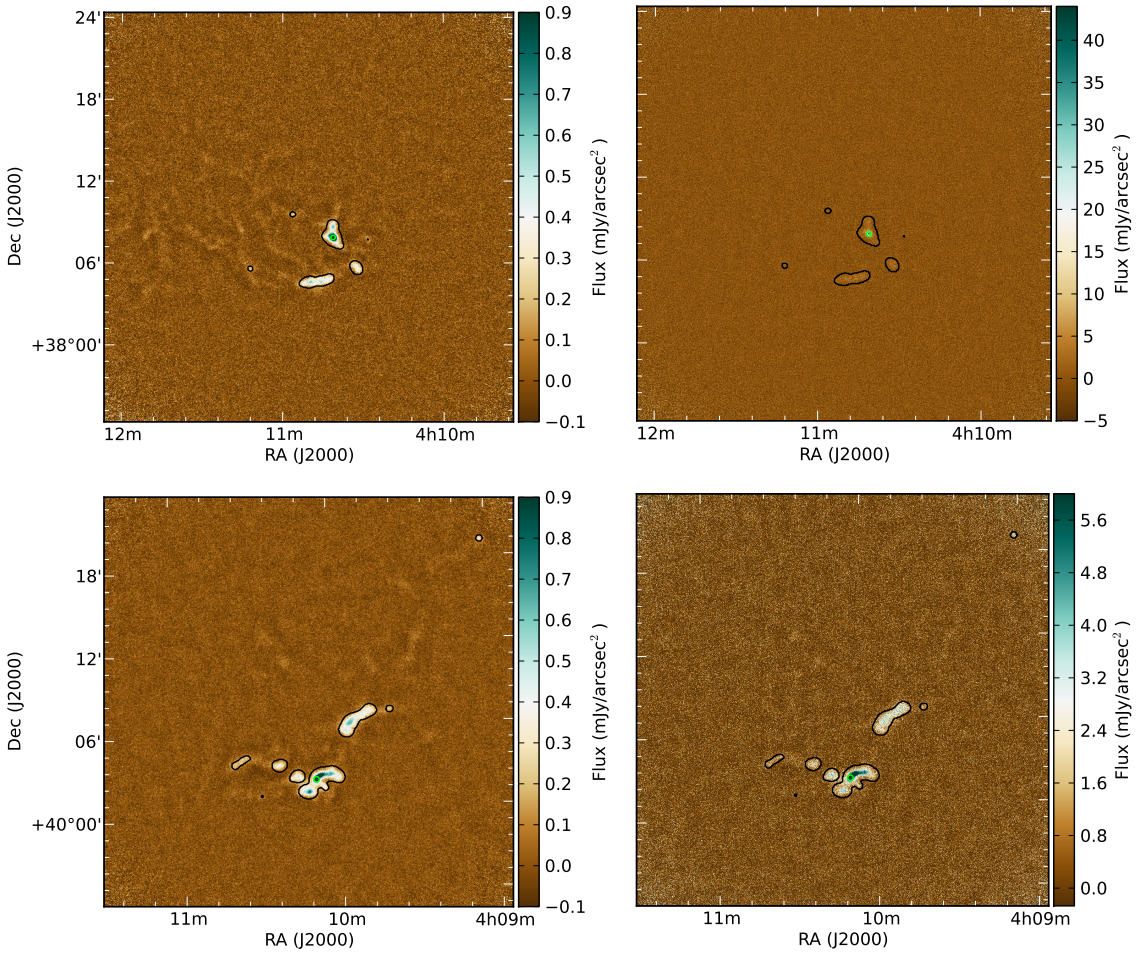

Figure 3.2 *continued*. Maps of AUR_Central-N (top) and AUR_NW (bottom) regions at 850 μm (left) and 450 μm (right).

3.2.2 HARP

We include previously unpublished ^{12}CO J=3-2 observations (PI Matthews: Program IDs M09BC16 and M10BC09) taken with HARP. Although that program was not completed, the coverage around LkHα 101, the region most susceptible to CO contamination (see below), was completed by the GBS with the same observing setup as the PI data.

All HARP data were processed with the ORAC-DR heterodyne pipeline (Jenness et al., 2015) using the REDUCED_SCIENCE_NARROWLINE recipe. In brief this sorts the timeseries into temporal order, identifies and rejects spectra affected by high-frequency noise and low-frequency non-astronomical signal using a non-linearity coefficient of 0.08 (where the best spectra have coefficients <0.025). The recipe enters an iterative phase. First it combines all the filtered timeseries cubes to form a group spectral cube with 6″ pixels and an effective spatial resolution of 16.6″, 1.0km s^{-1} (LkHα 101) or 0.1km s^{-1} spectral resolution. The spectral cube is smoothed with a spatial bias, and linear baselines subtracted to enable emission features to be detected and masked. The emission-free regions permit improved baseline fits, which are then subtracted from the group cube. One iteration proved sufficient. A clump-finding algorithm applied to the group cube locates the emission (using the CLUMPFIND technique from the CUPID package: Berry et al. 2007) which is integrated to generate a map for the CO contamination.

CO decontamination

The ^{12}CO J=3-2 (hereafter CO) emission line lies within the 850 μm SCUBA-2 filter, and therefore such emission is included in the total flux observed at 850 μm. We use the ^{12}CO J=3-2 HARP observations to remove the CO contribution from 850 μm maps in order to isolate the dust continuum emission. The CO emission has been found to be a significant contaminant of observations of dust continuum in the presence of outflows from young YSOs (Drabek et al., 2012); Sadavoy et al. (2013) found the CO line emission contributed up to 90% of the 850 μm flux in the presence of outflows. It is therefore necessary to measure the CO flux in the NGC 1529 cluster area around LkHα 101 where we expect the highest contamination, as it hosts the brightest cloud emission and is the densest area of star formation in the cloud (BF14). We subtract the detected CO emission in this one region to place an upper limit on CO contamination elsewhere.

To create a 850 μm map that is decontaminated of CO emission, the 850 μm data are reduced in the same way as the external mask reduction described in Section 3.2.1, with the exception of supplying the integrated CO intensity map as a negative source to the MAKEMAP routine. Done in this way, the CO emission that is subtracted from the map is subject to the same processing effects, such as spatial filtering, as the 850 μm data are.

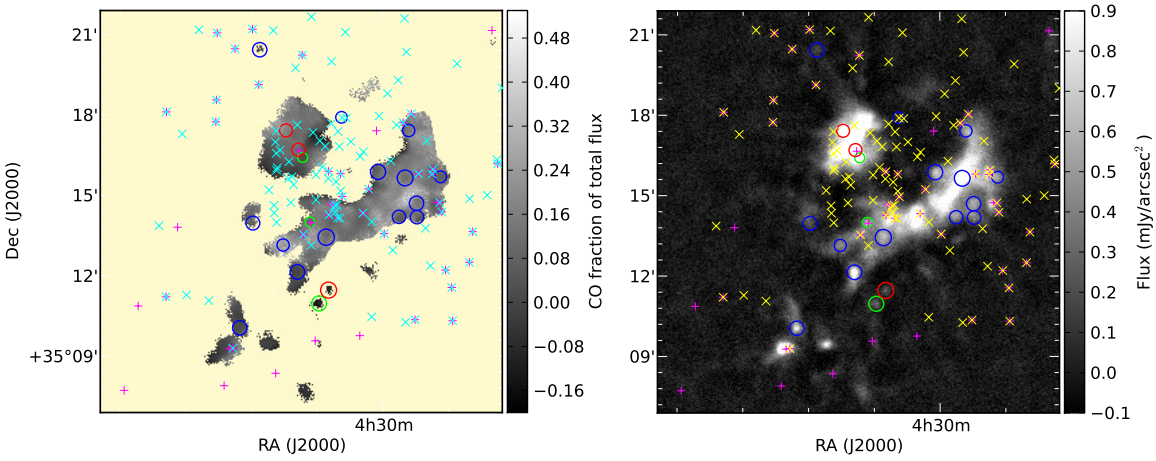

Figure 3.3 The fractional contribution of CO to the total 850 μm flux (left) is calculated from the CO-subtracted and non-CO-subtracted 850 μm maps in the region around LkHα 101. We mask pixels where the 850 μm flux is not detected, i.e., $< 3\sigma$ (pale yellow background) to measure the fractional contamination of CO in this region from only detected emission. The unmasked SCUBA-2 850 μm map is shown in the right panel. The locations of SCUBA-2 identified candidate YSOs satisfying compact source criteria (see Section 3.3) at both and 850 μm and 450 μm (green circles), only at 850 μm (red circles), and only at 450 μm (blue circles) are shown, with circle size corresponding to source size. Their locations coincide with lower relative CO contamination (generally levels below $\sim$20%) since the 850 μm continuum flux is higher. Candidate YSOs located in the bright arc of emission near LkHα 101 tend to fail the compact source criteria at 850 μm where the contrast between YSOs and the cloud emission is less due to both lower resolution and YSOs being fainter further down the Rayleigh-Jeans tail. Therefore it is harder to disentangle and characterize the 850 μm emission in this region. *Spitzer*-identified YSOs (magenta crosses from BF14 catalogue and x's from G09 catalogue) are also shown. The infrared YSOs (*Spitzer* and *Herschel*/PACS) are difficult to detect against the bright cloud emission and hence the locations of infrared YSOs and submillimeter candidate YSOs (*Herschel*/SPIRE and SCUBA-2) are almost mutually exclusive.

Figure 3.3 shows a map of the fractional contribution of CO to the total flux in the region around LkHα 101 where both dust and CO are detected. Overall, we find the measured CO contamination in NGC 1529 to be below 20% at the locations of compact sources (see Figure 3.3, left) and less than 50% elsewhere. As the total 850 μm emission peaks at source locations, the relative contribution of CO is lower for these objects. Additionally, the CO line saturates in bright areas limiting its total contribution to the 850 μm map, further limiting the relative contribution of the CO emission in brighter regions with high continuum flux. Therefore, we do not find that outflows from nearby sources are significantly contaminating the 850 μm fluxes of compact sources and expect that the contamination of 850 μm fluxes of compact sources elsewhere in the cloud is also <20%.

3.3 Results

3.3.1 Identifying candidate YSOs

As described in Section 3.2.1, the emission in the SCUBA-2 maps is composed of large scale cloud emission and compact emission from YSOs. With the varying brightness of the cloud emission, the co-location of YSOs (expected to have sizes up to ∼10 000 AU, ∼20″ at Auriga-Cal's distance) with such emission, and the large beam size of single-dish submm observatories (14.5″ and 7.5″ at 850 μm and 450 μm, respectively, at the JCMT), it is non-trivial to isolate the compact emission associated with YSOs from the larger scale emission associated with the cloud. There are many source finding algorithms used for such datasets (i.e., single dish submillimeter observations of star-forming regions), each with its own variation to identify and characterize emission. We use the *getsources* algorithm (Men'shchikov et al. 2012, Version 1.140127) to identify sources due to its sophisticated approach of using spatial decompositions and handling information from multiple maps with different resolutions. These qualities are especially powerful for the multiwavelength maps of varying resolution (such as 850 μm and 450 μm maps) and for the southern end of the cloud, where the star formation density is highest (and therefore source crowding is even more of an issue) and where the cloud emission is particularly bright due to the warming of the material from the early B-star, LkHα 101. This approach allows us to retain the advantage of the highest resolution available with JCMT maps, rather than having to degrade the resolution of 450 μm maps to match the 850 μm maps. We start by identifying all sources and then continue our analysis with only those that are compact, and therefore likely associated with YSOs (as opposed to larger sources associated with clumps and starless cores) in order to identify the population of submillimeter protostars and measure the mass of their circumstellar material.

The *getsources* algorithm was developed for source extraction in the *Herschel* Gould Belt Survey (André et al., 2010). It identifies sources by decomposing the maps into different spatial scales and using multi-wavelength observations of fields to identify structures and sources common to different maps while accounting for various resolutions. An initial extraction is run at each wavelength independently (monochromatic extractions), and then a combined extraction is done using information from the monochromatic extractions to make a source catalog. A final extraction (also composed of first monochromatic extractions and then a combined extraction) then uses the combined catalog from the initial extraction to flatten the images of background emission for the final estimation of source properties.

We perform the source extraction using both the 850 μm and 450 μm maps for each field independently. This is because of the varying noise levels between the 450 μm maps of different fields due to the increased sensitivity to the weather conditions in which they were observed. We also use *getsources* to extract the properties of sources identified in SCUBA-2 maps at *Herschel*/SPIRE wavelengths by supplying the footprints from the SCUBA-2 extraction to *getsources* and running it on the *Herschel*/SPIRE maps from Harvey et al. (2013). (We do not run *getsources* on the *Herschel*/PACS maps, however, as source identification in these maps was already done by Harvey et al. 2013.) The final *getsources* catalog contains 226 sources in SCUBA-2 maps and includes the extracted fluxes and sizes of the sources at each wavelength, as well as various internal parameters to represent the quality or robustness of each extracted source. This initial source catalog contains various kinds of sources that can be appear as a 2D Gaussian structure in these maps, such as, large scale cloud emission, clumps, cores, and YSOs/protostars. As our analysis is targeting at the protostar population, which we expect to have sizes of $\sim$20$''$, we first select only the compact sources in this original source list and then visually confirm this subset. The cuts for compact sources associated with protostars are based on geometry (sources must be compact with FWHM $\leq$ 20$''$ along both major and minor axes, and must not be elongated, i.e., aspect ratio $\leq$ 2) and flux (having a positive flux value with a signal-to-noise ratio $\geq$ 3 from *getsources*' internal parameters).

Figure 3.4 shows the measured values for each of the 38 compact sources that meet these criteria at 450 μm and/or 850 μm, and highlights where a compact source does not meet a specific criterion at either wavelength. All of the 38 compact sources are round at both wavelengths (i.e., none are elongated at either wavelength, even if other compact source criteria failed). Several have a similar size measured from the 850 μm map and the 450 μm map ($\sim$15–20$''$), suggesting that the measured size is tracing the true size of these objects. Those compact sources with low SNR ($<$ 3) determined within *getsources* at 850 μm tend also to have a large size and lie in the bright emission near LkHα 101, where it is more difficult to isolate and characterize sources. A source with a larger size is more difficult to

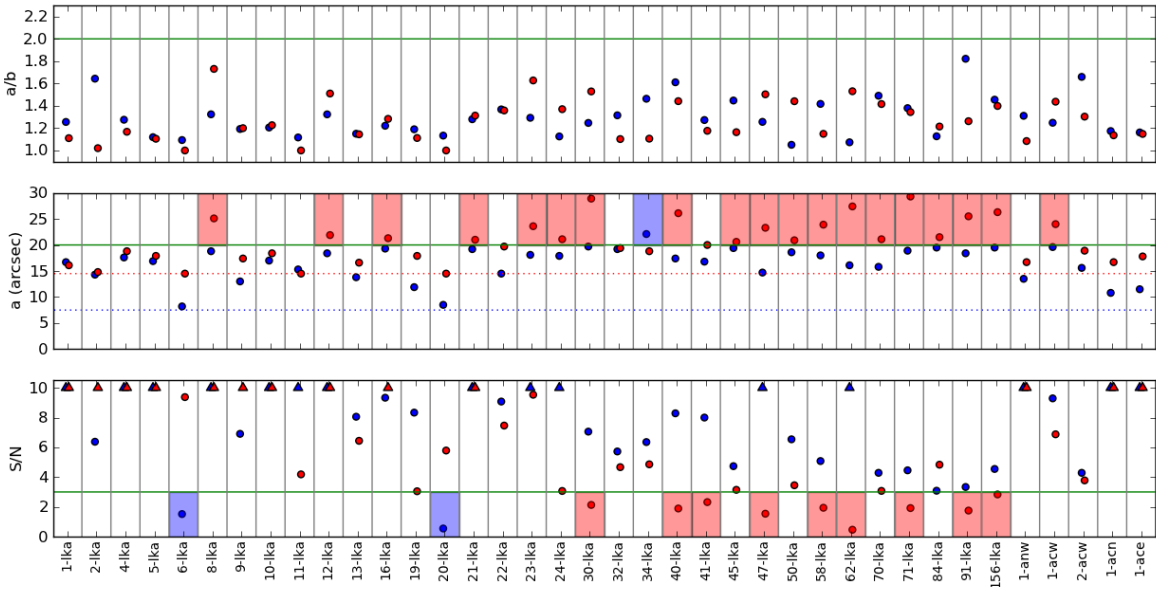

Figure 3.4 Criteria for identifying compact objects from the *getsources* extraction: aspect ratio (top), size (middle), and SNR (bottom, SNR) for each of the 38 objects that meet our criteria for compact sources at one or both SCUBA-2 wavelengths. (Note that an upwards arrow is displayed for the compact sources with SNR > 10 and therefore extending beyond the plot boundaries.) The green horizontal line marks the boundary for each criterion. The measured property is displayed for each source at both 450 μm (blue) and 850 μm (red). The area of the plot is shaded where a compact source does not meet the criterion at the wavelength corresponding to the color of the shading (blue=450, red=850). This highlights that a large size and/or a low SNR is the main issue for objects that do not meet all criteria at 850 μm. The objects which fail tend to be those co-located with the bright emission around LkHα 101 (see Figure 3.3). Dotted lines show the 450 μm and 850 μm beam sizes. All sources, however, are not elongated and have sizes < 30 $''$(about $2\times$ the beam size at 850 μm). This supports the interpretation that all sources that meet this criteria at at least one wavelength can be considered compact sources.

isolate from background emission. Also, it will be hard to accurately measure the size of a faint source with a low SNR. This issue is more problematic at 850 μm given both the lower resolution compared to 450 μm and the lower contrast between compact sources and background emission. The contrast is better at 450 μm, as source emission is higher up the Rayleigh-Jeans tail. These sources are still reasonable to include as compact sources as they all have measured sizes $<30''$, which is similar to the expected size of $\sim$20 $''$, especially considering that these sizes may be artificially higher to the difficulty in isolating them from large-scale emission.

All compact sources are then visually inspected to ensure that they are not associated with a feature such as a tail from another source. We plot the location of each compact source in a zoomed-in region of the SCUBA-2 maps to inspect them more carefully. We similarly also plot their location in *Herschel*/SPIRE and *Herschel*/PACS maps. These figures help us to determine: 1) the reliability of each extracted compact source, 2) whether there is, or could be, compact 70 μm emission indicating a protostellar source, and 3) the shortest wavelength at which the compact source is evident. We show an example for each of these points in Figure 3.5. Following this inspection, we remove two compact sources located in a strongly blended region (and therefore neither can be considered as a single source) around a background source (in the southern-most emission of our maps) that was recently identified at cm wavelengths with the Very Large Array (Broekhoven-Fiene et al., in prep).

We refer to the 36 vetted compact sources identified with the *getsources* algorithm as candidate YSOs, due to the compact nature of their emission. They are listed in Table 3.1 and named according to the IAU convention and designation for the GBS. We measure the submillimeter fluxes of these compact sources in Section 4.2.3 and use them in Section 3.3.4, along with consideration of *Spitzer* and *Herschel* catalogues, to refine their classifications.

The locations of the candidate YSOs are included in Figure 3.2, which shows that they are co-located with cloud emission. Such co-location is expected given that protostars have been observed to lie predominately along the filaments of their natal clouds (André et al., 2010). Consequently, our sensitivity to protostellar objects is limited by the brightness of the cloud emission along the line of sight rather than by our observation sensitivity, which determines the cloud emission recovered. For this reason, we expect the measured fluxes to be much higher than our sensitivity to an isolated point source.

3.3.2 Comparison to previous YSO catalogs

The positions of extracted candidate YSOs are compared to *Spitzer* (G09; BF14) and *Herschel*/PACS (Harvey et al., 2013) YSO catalogs. We refer to YSOs by the shortest

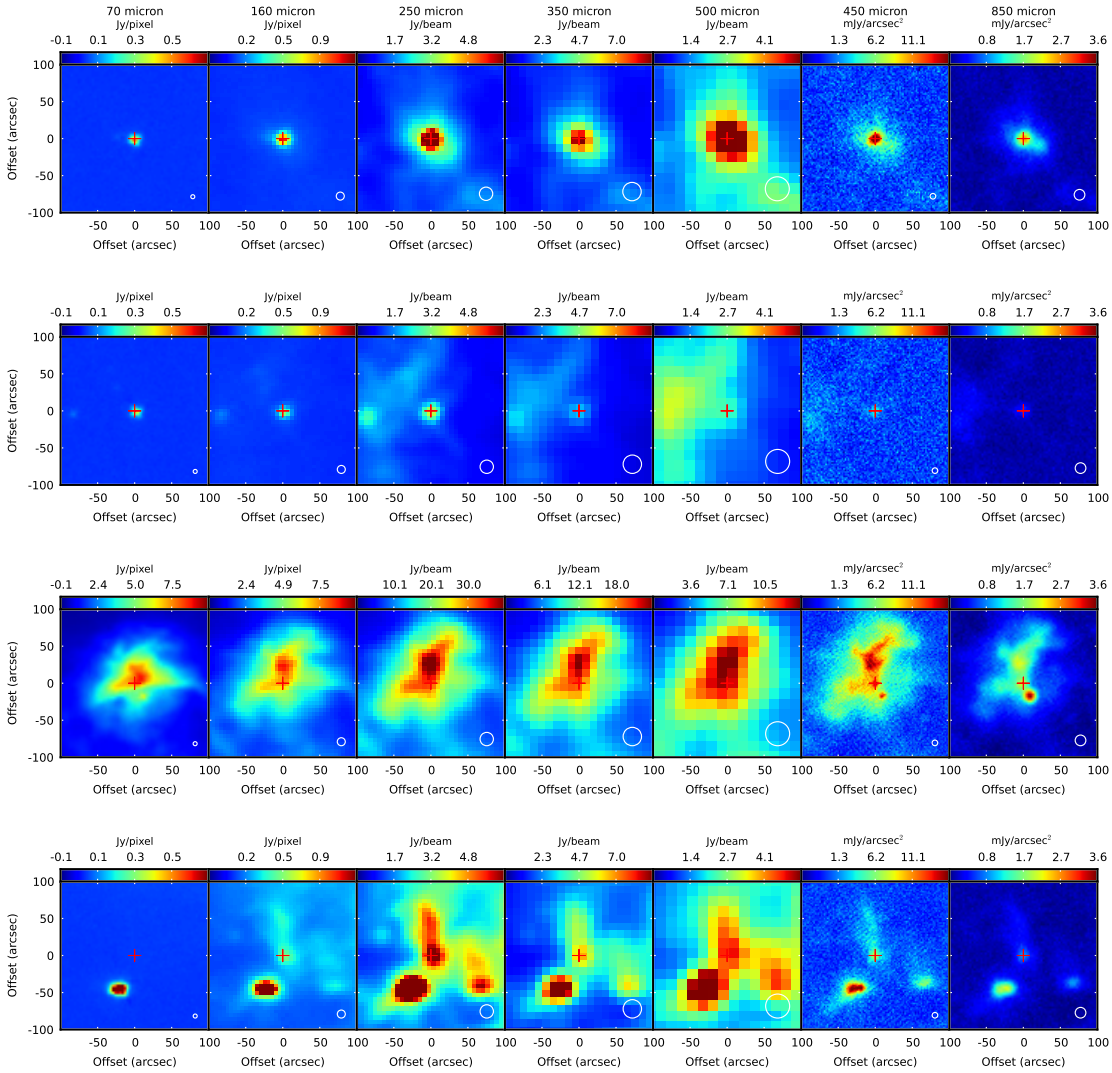

Figure 3.5 Examples of the quality assurance of compact sources extracted using *getsources* showing the *Herschel*/PACS (70 μm and 160 μm), *Herschel*/SPIRE (250 μm, 350 μm, and 500 μm), and SCUBA-2 (450 μm and 850 μm) maps, left to right. Each panel is centred on the compact source in question which is in turn marked with crosshairs. The rows show (from top to bottom): (1) an example of a well-detected compact source associated with a YSO identified with both *Spitzer* and *Herschel*/PACS; (2) A compact source identified in SCUBA-2 maps which is not very convincing visually at either 450 μm or 850 μm. Inspection of *Herschel* maps, however, provides the by-eye conviction of the presence of compact emission. This demonstrates the effectiveness of *getsources*' source identification in the SCUBA-2 maps; (3) An example of a compact source for which the presence of compact 70 μm emission, indicative of a protostellar source, can be neither confirmed nor ruled out given the presence of bright background emission; (4) An example of a seemingly robust submillimeter compact source that is not detected at wavelengths shorter than 160 μm.

wavelength regime at which they were first identified. We detect 18 YSOs previously identified with *Spitzer* or *Herschel*/PACS (2 detected by *Spitzer*-only, and 2 identified with *Herschel*/PACS only). We deem these candidate YSOs associated with a *Spitzer*-YSO or compact 70 μm emission as robust protostellar objects.

Of the 16 robust YSOs that were previously detected with *Spitzer*, 12 were identified as Class I[1], one was identified as Class F (flat spectrum), and three were identified as Class II (BF14). Buckle et al. (2015) show that in Taurus the detection efficiency of the different Class YSOs declines with later Classes. At 850 μm, they recover 88% of the Class I YSOs, 38% of the Class IIs, and 11% of the Class IIIs. Auriga-Cal is 3$\times$ further away than Taurus and so our recovery of YSOs is much less as the YSOs are even fainter.

In Figure 3.3 (right), we highlight the area near LkHα 101 and compare the locations of our candidate protostellar objects to *Spitzer* YSO catalogs (G09; BF14). (There are no *Herschel*/PACS-identified YSOs in this field .) The SCUBA-2 candidate YSOs are mainly located in the arc of cloud emission and the *Spitzer* YSOs are beyond it. There are only three YSOs in the vicinity of LkHα 101 identified in both the infrared and the submillimeter. The other 16 SCUBA-2 candidate YSOs that are associated with YSOs previously identified at infrared wavelengths (with *Spitzer* and/or *Herschel*/PACS) are located elsewhere in the cloud where background cloud emission is not as bright as it is around LkHα 101. The bright cloud emission in this region, due to LkHα 101, obstructs the identification of YSOs in the infrared. In the submillimeter, however, the contrast between a YSO and the background level is higher and more favourable for YSO detection.

[1]Note that a *Spitzer*-identified "Class I" is to be interpreted as a "Class 0 or Class I" as *Spitzer* cannot distinguish between these two SED classes.

ID	Source name	Other identifiers		450 micron flux	850 micron flux	250 micron flux	350 micron flux	500 micron flux
		Spitzer	Herschel	(Jy)	(Jy)	(Jy)	(Jy)	(Jy)
1	JCMTLSG J043014.7+351625	···	···	$\lesssim$1.504[a]	$\lesssim$0.804[a]	···	9.57 ± 2.63	5.42 ± 1.55
2	JCMTLSG J043038.6+355025	···	42	6.92 ± 1.45	1.52 ± 0.40	6.97 ± 1.42	5.10 ± 1.05	3.04 ± 0.79
3	JCMTLSG J043036.8+355439	103	38	10.23 ± 2.12	1.69 ± 0.51	10.40 ± 2.08	7.72 ± 1.56	5.62 ± 1.15
4	JCMTLSG J043015.4+351642	138	···	$\lesssim$1.668[a]	$\lesssim$0.482[a]	15.69 ± 3.58	···	···
5	JCMTLSG J043015.6+351209	···	···	5.51 ± 1.19	0.83 ± 0.30	6.59 ± 1.85	5.62 ± 1.80	3.15 ± 1.16
6	JCMTLSG J043038.0+355103	107	40	1.39 ± 0.38	$\lesssim$0.256[a]	4.37 ± 0.90	2.72 ± 0.60	1.40 ± 0.54
7	JCMTLSG J043048.7+353755	124	50	3.63 ± 0.81	$\lesssim$0.276[a]	5.17 ± 1.06	3.33 ± 0.69	2.08 ± 0.45
8	JCMTLSG J043041.4+352943	117	45	3.14 ± 0.82	$\lesssim$0.350[a]	3.22 ± 0.74	2.28 ± 0.72	1.32 ± 0.37
9	JCMTLSG J043026.1+351003	···	···	2.12 ± 0.60	$\lesssim$0.196[a]	5.05 ± 1.37	3.95 ± 1.07	2.50 ± 0.74
10	JCMTLSG J043056.8+353006	135	57	2.14 ± 0.49	$\lesssim$0.117[a]	3.67 ± 0.81	2.14 ± 0.54	1.23 ± 0.33
11	JCMTLSG J043038.4+355000	108	41	1.79 ± 0.45	$\lesssim$0.229[a]	4.71 ± 0.96	3.35 ± 0.71	2.46 ± 0.71
12	JCMTLSG J043013.3+351401	67	···	$\lesssim$0.571[a]	$\lesssim$0.157[a]	···	···	···
13	JCMTLSG J043017.7+351725	···	···	3.05 ± 0.84	$\lesssim$0.322[a]	···	···	···
14	JCMTLSG J043044.3+355953	118	46	2.82 ± 0.64	$\lesssim$0.189[a]	3.27 ± 0.66	2.66 ± 0.56	2.07 ± 0.46
15	JCMTLSG J043024.8+354523	81	29	1.93 ± 0.44	$\lesssim$0.106[a]	3.05 ± 0.65	1.47 ± 0.44	···
16	JCMTLSG J043030.8+355141	100	35	2.37 ± 0.56	$\lesssim$0.192[a]	1.43 ± 0.33	1.60 ± 0.36	1.51 ± 0.50
17	JCMTLSG J043000.9+351553	···	···	$\lesssim$0.714[a]	$\lesssim$0.185[a]	···	···	···
18	JCMTLSG J042955.9+351539	···	···	5.65 ± 1.19	0.87 ± 0.26	···	···	···
19	JCMTLSG J043011.6+351058	···	···	1.55 ± 0.38	$\lesssim$0.079[a]	···	···	···
20	JCMTLSG J043009.9+351128	···	···	1.51 ± 0.36	$\lesssim$0.079[a]	···	···	···
21	JCMTLSG J042955.2+351725	···	···	1.56 ± 0.44	$\lesssim$0.163[a]	2.57 ± 0.94	···	···
22	JCMTLSG J042957.0+351412	···	···	1.29 ± 0.47	$\lesssim$0.140[a]	···	···	···
23	JCMTLSG J042953.8+351442	···	···	1.27 ± 0.45	$\lesssim$0.144[a]	2.87 ± 1.11	···	···
24	JCMTLSG J042949.4+351541	···	···	$\lesssim$0.556[a]	$\lesssim$0.136[a]	···	···	···
25	JCMTLSG J043010.4+351326	···	···	1.64 ± 0.51	$\lesssim$0.166[a]	···	···	···
26	JCMTLSG J042953.8+351411	···	···	$\lesssim$0.493[a]	$\lesssim$0.120[a]	···	···	···
27	JCMTLSG J043023.8+351358	···	···	0.90 ± 0.27	$\lesssim$0.080[a]	···	···	···
28	JCMTLSG J043007.5+351755	···	···	0.28 ± 0.09	$\lesssim$0.056[a]	···	···	···
29	JCMTLSG J043022.5+352026	···	···	0.81 ± 0.22	$\lesssim$0.056[a]	···	···	···
30	JCMTLSG J043018.2+351309	···	···	$\lesssim$0.442[a]	$\lesssim$0.113[a]	···	···	···
31	JCMTLSG J043015.6+355659	71	28	0.72 ± 0.20	$\lesssim$0.043[a]	3.00 ± 0.63	1.47 ± 0.36	0.77 ± 0.28
32	JCMTLSG J041008.5+400225	6	7	12.45 ± 2.55	1.56 ± 0.45	20.01 ± 4.03	10.54 ± 2.12	5.50 ± 1.17
33	JCMTLSG J042138.1+373438	16	12	8.01 ± 1.69	0.99 ± 0.37	10.68 ± 2.15	7.72 ± 1.60	5.27 ± 1.10
34	JCMTLSG J042141.0+373358	18	13	2.17 ± 0.62	$\lesssim$0.238[a]	2.04 ± 0.61	2.73 ± 0.77	3.15 ± 0.71
35	JCMTLSG J041041.2+380754	10	9	23.70 ± 4.80	3.63 ± 0.85	32.42 ± 6.49	17.24 ± 3.45	9.07 ± 1.83
36	JCMTLSG J042508.2+371521	···	15	5.30 ± 1.12	0.71 ± 0.26	6.28 ± 1.26	3.76 ± 0.79	2.02 ± 0.42

Table 3.1 Candidate YSOs identified in SCUBA-2 maps with *getsources*

Table 3.1 *Continued:* Candidate YSOs identified in SCUBA-2 maps with *getsources* (table notes)

Note. — Uncertainties quoted are statistical flux uncertainties, returned by aperture photometry for SCUBA-2 fluxes and *getsources* for *Herschel*/SPIRE fluxes, do not include the calibration uncertainties of 10% and 5% for SCUBA-2 observations at 450 μm and 850 μm, respectively Dempsey et al. (2013) and $\pm$5 % for *Herschel*/SPIRE fluxes under ideal circumstances (http://herschel.esac.esa.int/hcss-doc-9.0/).

[a]We have listed first estimates of the fluxes as the peak flux (converted to Jy/beam) for candidate YSOs that are difficult to disentangle from the background emission.

3.3.3 Flux measurement

We include the fluxes measured in maps from multiple infrared and submillimeter instruments, all with different resolutions affecting the appearance. In addition to the effect of resolution, the intrinsic spatial scale sampled of the emission from a YSO depends on the wavelength at which it is observed. At infrared wavelengths, the emission is expected to be more compact than at submillimeter wavelengths, as it originates from the more central material that is warmed by the protostar. The infrared emission can be fit as a point source, even in the 6″ resolution *Herschel*/PACS 70 μm images. YSO emission at submillimeter wavelengths, however, despite the lower resolution (7.5″ and 14.5″ for SCUBA-2), must be fit with allowance for a more extended profile, to account for cooler dust emission from the envelope which can have a size up to 10,000 AU ($\sim$20″ at Auriga-Cal's distance). For each wavelength, therefore, the method we use to determine the flux of the emission associated with the YSO depends on the resolution of maps and the contrast between the cloud and YSO emission. This is preferable to extracting the flux in the same manner at all wavelengths, as such an analysis would require essentially considering all emission at the resolution corresponding to the lowest resolution map (in this case, the 36″ resolution of the 500 μm *Herschel*/SPIRE maps). Such fluxes would be consistent essentially pixel to pixel, however, we would lose the benefits of the higher resolution maps in better isolating compact sources and have more cloud emission contributing to all fluxes at all wavelengths. We therefore measure the fluxes at each of the PACS, SPIRE, and SCUBA-2 wavelengths using the techniques that have been found to be optimal for the corresponding instrument. For each instrument, we describe how the fluxes are measured and how that technique has accounted for the cloud emission to isolate the emission from the YSOs.

The *Herschel*/PACS fluxes for YSO candidates associated with a *Herschel*/PACS-identified YSOs are adopted from Harvey et al. (2013) (measured using the *c2dphot* package developed for the Spitzer Legacy c2d program: Harvey et al. 2006; Evans et al. 2007). These data are very straightforward for identifying compact sources: the 70 μm map is essentially composed of point-like sources with some cloud emission only in the region around LkHα

101 (albeit very bright). The 160 μm map has large scale emission, but it is faint relative to the bright YSOs, which still appear point-like. The SCUBA-2 YSO candidates from this work that are not associated with an infrared YSO (either *Herschel*/PACS or *Spitzer*) are in regions of bright cloud emission and therefore any compact 70 μm emission may be indistinguishable from the bright background. For these candidate YSOs, we measure the upper limit on the possible 70 μm flux as the total flux within a 20$''$ aperture centred on each candidate YSO's position.

The *Herschel*/SPIRE fluxes are adopted from the source properties extracted by *getsources* (see Section 3.3.1). This is reliable since *getsources* has been designed for and tested on *Herschel* data. The compact emission is disentangled from the cloud emission by the spatial decompositions and background modelling done within *getsources*.

For SCUBA-2 fluxes, aperture photometry is used rather than the properties extracted by *getsources*. Although *getsources* is a rigorous algorithm to disentangle emission from nearby sources and the cloud to identify sources (e.g., Figure 3.3), the SCUBA-2 beam shape is very different from the *Herschel* beam, particularly at 450 μm where about half the beam power is concentrated in the secondary beam that extends beyond the primary 7.5$''$ component (Dempsey et al., 2013). The primary beam of both the 450 μm and 850 μm beams is still relatively Gaussian (Dempsey et al., 2013) allowing *getsources* to identify Gaussian-like sources with spatial decompositions. More subtle differences in the larger scale components of the JCMT beam shapes from the *Herschel* beam shapes, however, complicate using the flux measurements by *getsources* for SCUBA-2 data. Using aperture photometry on SCUBA-2 maps, however, is well-tested and better understood (Dempsey et al., 2013; Buckle et al., 2015; Pattle et al., 2015) and therefore we use it to measure 850 μm and 450 μm fluxes, accounting for the background with sky apertures.

Aperture photometry is performed on the 850 μm maps and 450 μm maps which have been convolved to the 850 μm resolution to sample similar spatial scales. The convolution kernel used, described in Pattle et al. (2015), is based on Dempsey et al. (2013)'s SCUBA-2 beam models. Fluxes are measured using 20$''$ diameter apertures at the locations of the candidate YSOs and sky annuli from 30$''$ to 40$''$. In cases where sky annuli are not appropriate (e.g., a varying background or a nearby source lying inside the sky annulus), a nearby sky aperture of 20$''$ diameter is used instead. In some cases, such as the bright arc of emission near LkHα 101, we use an irregularly shaped aperture to estimate the sky value and standard deviation in the entire arc while masking the peaks/candidate YSOs. This, however, still results in a background value with a large standard deviation and therefore strong SNR is difficult to obtain. For sources in this region that have a low SNR (< 3) due to this difficult to model cloud emission, we have listed the peak flux in Table 3.1. We use aperture corrections from Dempsey et al. (2013) of 0.69 for 20$''$ apertures at 850 μm. We use

the same aperture correction for the 450 μm fluxes as the 450 μm maps have been convolved to the 850 μm beam. The final aperture corrected fluxes are included in Table 3.1.

3.3.4 YSO population

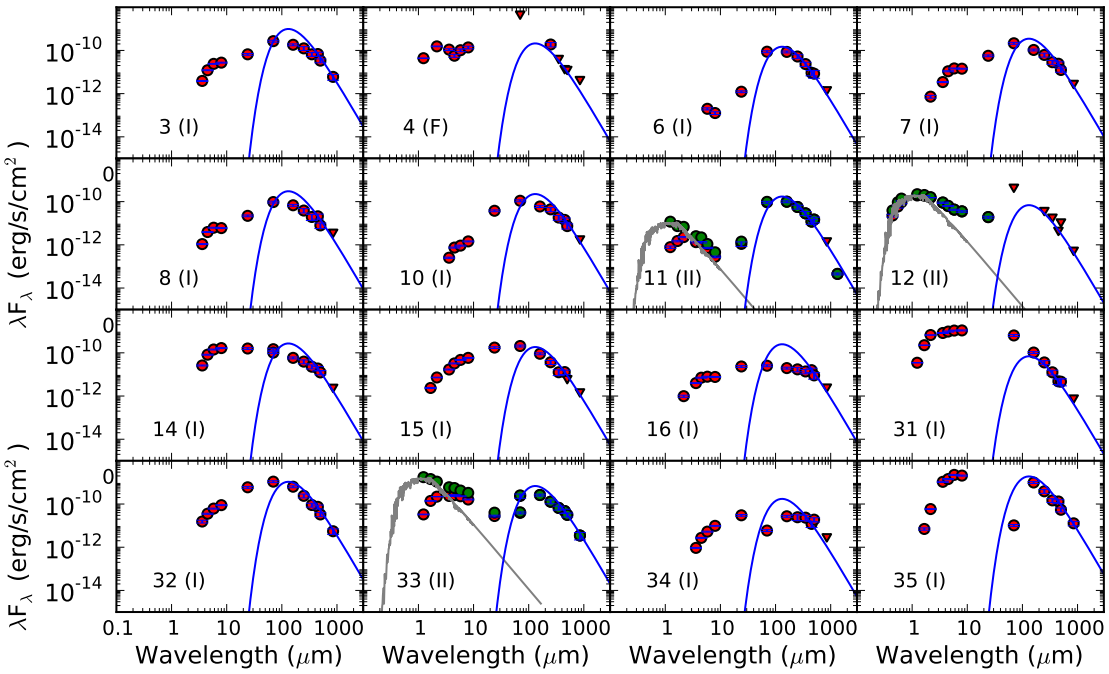

Figure 3.6 SEDs for SCUBA-2 candidate YSOs associated with *Spitzer*-identified YSOs. The ID number from Table 3.1 is shown in the bottom of each panel with the *Spitzer* YSO Class listed in parentheses. Red circles show observed fluxes. Panels with Class II sources include a sample stellar K7 spectrum that is normalized to the IR flux at the shortest available wavelength. The fitted stellar spectrum is used to estimate an A_V value and therefore the dereddened fluxes (green circles). The blue curve shows the emission from 20 K dust fit using the masses calculated from 450 and 850 μm fluxes (see Section 3.3.6) and listed in Table 3.2.

We collect available photometry from 2MASS, *Spitzer*, *Herschel*/PACS to complement the SCUBA-2 and *Herschel*/SPIRE photometry measured here. The SEDs for SCUBA-2 candidate YSOs associated with *Spitzer*-identified YSOs are shown in Figure 3.6 along with their *Spitzer* Class identification. The near-infrared photometry of Class II YSOs is more likely to be tracing the photosphere of the central star (than the enshrouded Class I and earlier YSOs), and so we have included a sample K7 stellar spectrum normalized to the near-infrared flux at the shortest available wavelength. SEDs for candidate YSOs with photometry at only far-infrared and longer wavelengths are shown in Figure 3.7.

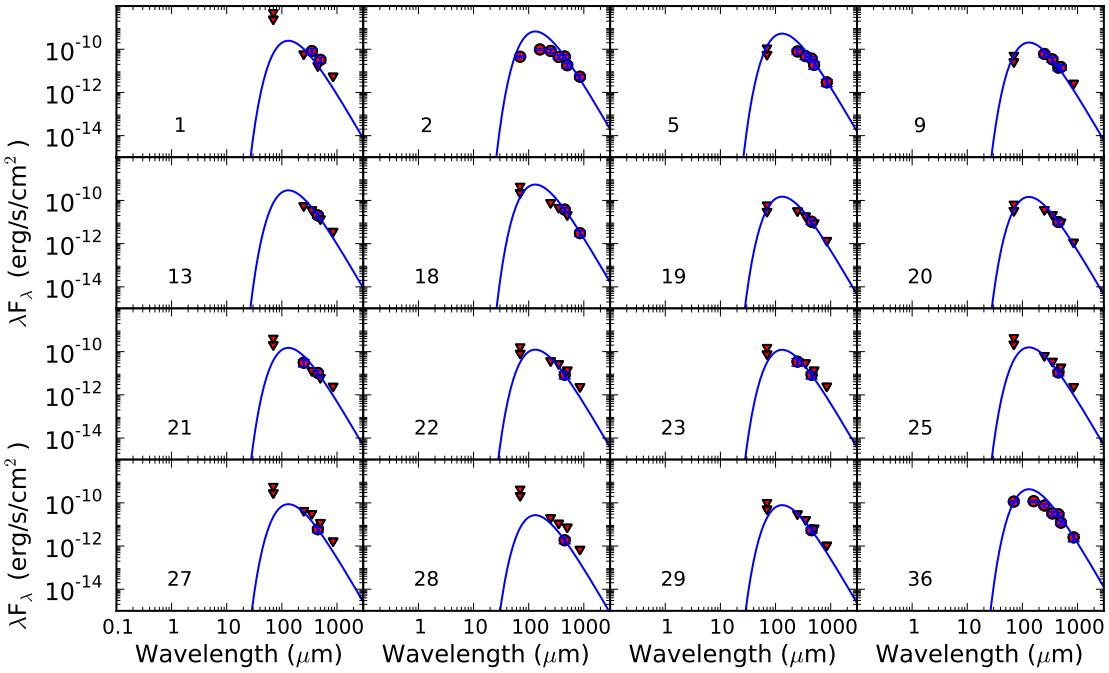

Figure 3.7 SEDs for SCUBA-2 candidate YSOs not associated with *Spitzer*-identified YSOs (most probably due to observational constraints in the region rather than the absence of compact IR flux, see Section 3.3.5). The ID from Table 3.1 is shown in the bottom of each panel. Only the 16 candidate YSOs with detections at two or more wavelengths are shown. The blue curve shows the emission from 20 K dust fit using the masses (or upper limits) calculated from 850 μm and 450 μm fluxes (see Section 3.3.6) and listed in Table 3.2.

To identify whether the candidate YSOs are associated with Class 0 YSOs, we follow the approach of Sadavoy et al. (2014) for candidate YSOs identified in the submillimeter (*Herschel* and SCUBA-2). Class 0 protostars are more deeply embedded than later Class protostars and therefore more of their emission is emitted at longer wavelengths, especially the submillimeter. Consequently, they are identifiable by lower bolometric temperatures, T_{bol}, and a higher ratio of submillimeter luminosity, L_{smm}, to bolometric luminosity, L_{bol}, than later Class protostars. Briefly, the Class 0 object criteria are $T_{bol} < 70$ K, $L_{smm}/L_{bol} > 1\%$, and $M_{env} > M_*$, where M_{env} is the mass of the envelope (circumstellar material) and M_* is the mass of the central protostar. (The final criterion requires that the protostar is still in an earlier stage of accretion with more mass in the envelope than the central protostar.) The final criterion is imposed by using a decreasing accretion rate model, which implies $M_{env}/M_\odot > 0.2\ (L_{bol}/L_\odot)^{0.6}$, or a constant accretion rate model, which implies $M_{env}/M_\odot > 0.1\ (L_{bol}/L_\odot)$. T_{bol} is calculated using the prescription by Myers & Ladd (1993) and the trapezoidal rule for integration. L_{bol} is calculated using all available photometry and L_{smm}

is calculated using only fluxes at wavelengths > 350 μm (see Sadavoy et al. 2014 for details). We include extracted fluxes from *Herschel*/SPIRE maps and 70 μm flux upper limits from *Herschel*/PACS maps to constrain L_{bol} and T_{bol}.

Objects which meet these criteria are noted as Class 0 YSOs in Table 3.2. T_{bol} is calculated for all candidate and robust YSOs and also included in Table 3.2 for comparison with YSO classifications based on infrared data alone of robust protostellar objects. In some cases the Class of the object has been updated to an earlier Class upon the inclusion of the submillimeter data. We include the upper limits on T_{bol} for the remaining candidate YSOs, using the upper limit of 70 μm flux. The limits on T_{bol} for these objects are generally $\lesssim 50$ K (except for one with $T_{bol} \lesssim 315$ K) suggesting that if these objects are indeed protostellar, they must be very young (Class 0). One might suggest that this is obvious given the absence of a detection in the infrared, suggesting a deeply embedded object, however, we remind the reader that all the submm-only candidate YSOs are in very bright regions of the cloud where the background level prohibits detection of the expected level of emission from a YSO (see Section 3.3.1 and 3.3.5). It is also possible that these are actually prestellar objects and no protostar is present at their centres. Given the limitations in resolution and sensitivity above the cloud emission, interferometric observations will be required to probe the circumstellar dust emission.

3.3.5 Candidate YSOs co-located with bright cloud emission

Half of the candidate YSOs identified in SCUBA-2 maps (18 out of 36) are not associated with a *Spitzer*-identified nor *Herschel*-identified YSO. The candidate YSOs are predominantly located in the bright emission near LkHα 101, with three located in other bright areas. We therefore focus on the bright emission near LkHα 101, particularly the arc of emission to the south-west. We discuss here the limitations to confirming the nature of these candidate YSOs through the identification of compact 70 μm emission, constraints on their size, and the measurement of a submillimeter SED consistent with that of a YSO.

Compact 70 μm emission associated with warmer material closer to the protostar is expected for YSOs. Compact prestellar cores in contrast will not be associated with compact infrared emission and only be detected at submillimeter wavelengths. Therefore the identification of compact infrared emission, such as at 70 μm, can be used to confirm the protostellar nature of a source. Such emission in the 70 μm maps can be neither ruled out nor verified, however, in the bright arc of cloud emission near LkHα 101. The median 70 μm flux of robust YSOs associated with a *Herschel*/PACS YSO is $\sim$1 Jy in comparison to the average flux per pixel of the arc of $\sim$0.7 Jy. This is further demonstrated by the fact that no YSOs are identified in the 70 μm data in this region (shown in Figure 3.3).

We therefore continue to call these sources candidate YSOs as we cannot verify or rule out compact emission at infrared wavelengths.

The contrast between these candidate YSOs and the cloud is much higher at submillimeter wavelengths. Coupled with the higher resolution compared to *Herschel*/SPIRE maps, this makes the peaks of compact sources easier to identify in SCUBA-2 maps. It is still difficult to disentangle cloud emission from the compact YSO emission with sky apertures, as the cloud emission varies within the sky apertures. For these candidate YSOs, although we are confident in the existence of compact emission identified with *getsources*, the flux associated with that compact emission is difficult to isolate. For these sources, which have much higher uncertainty in sky aperture and therefore total flux, we therefore list the flux of peak pixel (converted to Jy/beam) of the candidate YSO as an initial estimate of the flux of the source.

3.3.6 Masses

The circumstellar masses, M, of submillimeter-detected robust and candidate YSOs are calculated from the 850 μm and 450 μm fluxes, where available, using

$$M = \frac{F_{dust} D^2}{\kappa_\nu B_\nu(T_{dust})} \tag{3.1}$$

where D is the distance to the source, κ_ν is the opacity of the dust grains, and $B_\nu(T_{dust})$ is the Planck function for temperature, T_{dust}. The opacity is assumed to be $\kappa_\nu = 0.1(\nu/1000\ \mathrm{GHz})^\beta\ \mathrm{cm}^2\ \mathrm{g}^{-1}$ (Beckwith et al., 1990). Note that the opacity relation includes an assumed dust-to-gas ratio of 1:100 and therefore M represents the total dust+gas mass of circumstellar material, the disk and envelope. Therefore, the submillimeter mass will be dominated by the envelope for younger (i.e., Class 0/I) sources whereas the submillimeter mass for more-evolved sources (i.e., Class IIs) reflects material which remains in the circumstellar disk after the envelope is dispersed. Our observations are sensitive to the YSOs with the most massive circumstellar material, i.e., the Class 0/Is which are still surrounded by an envelope, as demonstrated by the majority of detected YSOs identified with *Spitzer* YSOs being Class I/F objects with only a few associated with Class II objects (Section 3.3.2).

We assume a dust temperature of 20 K for the submillimeter emission of all candidate YSOs to calculate their circumstellar masses as a compromise between various Classes. We expect objects of earlier Class to be slightly cooler ($\sim$15 K; Young et al. 2003), shielded by their envelope, and objects of later Class to be slightly warmer. This assumption simplifies the comparison between candidate YSOs within Auriga-Cal. The spectral slope between 850 μm and 450 μm of candidate YSOs with significant fluxes at both wavelengths is steeper

ID	IR classification	Classification	T_{bol} (K)	M ($M_\odot$)
(1)	(2)	(3)	(4)	(5)
1	···	candidate Class 0	<50.3	<0.415
2	Class 0 (PACS)	Class 0	21.4	1.116 ± 0.233
3	Class 0/I	Class I	71.3	1.649 ± 0.343
4	Class F	Class I	111.1	<0.354
5	···	candidate Class 0 or I	<312.9	0.888 ± 0.192
6	Class 0/I	Class 0	37.9	0.248 ± 0.060
7	Class 0/I	Class I	78.7	0.585 ± 0.130
8	Class 0/I	Class 0	66.0	0.507 ± 0.132
9	···	candidate Class 0	<19.6	0.342 ± 0.096
10	Class 0/I	Class 0	64.5	0.376 ± 0.076
11	Class II	Class 0	50.8	0.288 ± 0.073
12	Class II	Class II	2464.6	<0.115
13	···	···	···	0.492 ± 0.136
14	Class 0/I	Class I	212.8	0.455 ± 0.104
15	Class 0/I	Class I	144.7	0.311 ± 0.071
16	Class 0/I	Class I	133.3	0.418 ± 0.086
17	···	···	···	<0.219
18	···	candidate Class 0	<50.2	0.911 ± 0.193
19	···	candidate Class 0	<22.7	0.251 ± 0.062
20	···	candidate Class 0	<23.8	0.244 ± 0.058
21	···	candidate Class 0	<45.7	0.251 ± 0.071
22	···	candidate Class 0	<35.6	0.207 ± 0.076
23	···	candidate Class 0	<40.5	0.204 ± 0.073
24	···	···	···	<0.108
25	···	candidate Class 0	<42.7	0.264 ± 0.082
26	···	···	···	<0.177
27	···	candidate Class 0	<48.2	0.145 ± 0.044
28	···	candidate Class 0	<51.2	0.045 ± 0.014
29	···	candidate Class 0	<35.4	0.131 ± 0.036
30	···	···	···	<0.158
31	Class 0/I	Class I	384.3	0.116 ± 0.032
32	Class 0/I	Class I	84.8	1.792 ± 0.370
33	Class II	Class I	403.0	1.144 ± 0.245
34	Class 0/I	Class I	103.7	0.290 ± 0.092
35	Class 0/I	Class I	325.0	3.177 ± 0.645
36	Class 0 (PACS)	Class 0	25.6	0.714 ± 0.153

Table 3.2 Summary of masses and temperatures

Note. — Columns: (1) – ID from Table 3.1; (2) – Classification based on infrared spectral slope for robust YSOs associated with a detected *Spitzer* YSO or *Herschel*/PACS YSO (YSOs only detected with PACS and not *Spitzer* are noted). Note that *Spitzer* cannot distinguish between Class 0 and Class I, so we have noted Class 0/I instead of Class I as noted in c2d and related works; (3) – Classification based on submillimeter data according to the conditions in Section 3.3.4 with candidate classifications based on T_{bol}; (4) – T_{bol} calculated (see Section 3.3.4) where upper limits calculated using upper limits on 70 μm fluxes (see Section 4.2.3) in conjunction with submillimeter fluxes (if there are enough detections at submillimeter wavelengths); (5) – dust mass measured using Equation 4.2 and assuming T_{dust} = 20 K and $\beta = 1.5$ (see Section 3.3.6).

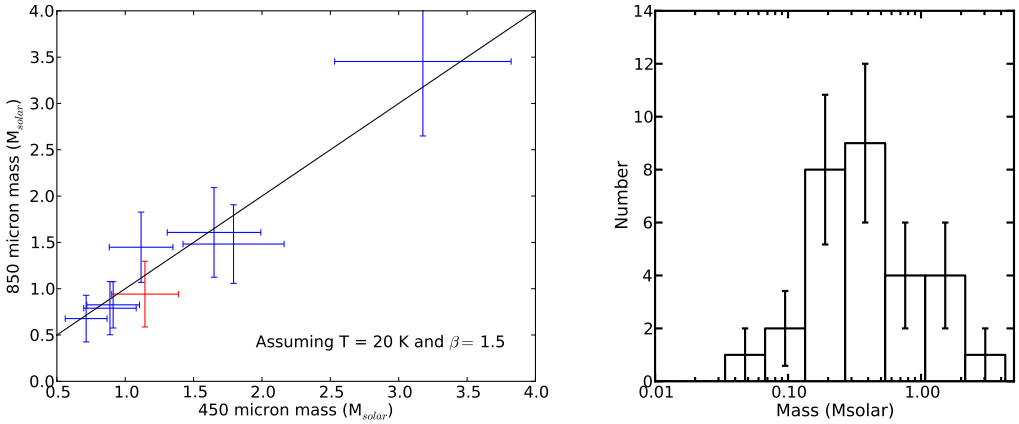

Figure 3.8 Left: comparison of masses calculated with 450 μm (abscissa) and 850 μm (ordinate) fluxes and using Equation 4.2 and assuming T = 20 K and $\beta = 1.5$. The solid black line shows the one-to-one relation. This demonstrates that the assumed parameters are consistent with the SED measured with the JCMT. Right: Circumstellar (disk+envelope) mass distribution of calculated masses. The JCMT GBS observations are sensitive to the high-mass end of the mass distribution.

than the expected power law slope of α=3=2+β for the standard simplifying assumption for YSOs of $\beta = 1$ (e.g., Andrews & Williams 2005). It is more consistent with α= 3.5 and so we use β=1.5 in our mass calculation, consistent with the β value measured toward Class 0/I protostars in Perseus by the JCMT GBS (Chen et al., submitted). For candidate YSOs with detections at only one wavelength we therefore adopt a temperature of 20 K and a β of 1.5. For candidate YSOs detected at both wavelengths, we report the weighted mean of the mass calculated from each flux, with mass uncertainties derived from the flux uncertainties. All masses are listed in Table 3.2.

The JCMT GBS observations are sensitive to the high-mass end of the circumstellar mass-distribution, with more masses > 0.1 $M_\odot$ than is measured in other clouds, such as Taurus (Andrews & Williams, 2005) and Ophiuchus (Andrews & Williams, 2007). These clouds, however, are much closer (140 pc and 150 pc) than Auriga-Cal, which may have artificially higher masses due to more mass from surrounding material being included in a single beam. This difference is not surprising given that Auriga-Cal has a higher fraction of Class I objects than these clouds (Chapter 2), and so should have more objects at a younger stage with more circumstellar material. It would be interesting to determine whether disk mass distribution near the early B-star, LkHα 101, were truncated, as is observed for disks in proximity to the O-star θ^1Ori C in Orion A North (Mann & Williams, 2009b; Mann et al., 2014). It is difficult, however, to investigate such a measurement in this region with single dish observations given the bright background cloud emission coupled with the small angular proximity of YSOs.

3.3.7 Comparison with Orion A

Infrared observations with *Spitzer* suggest that Auriga-Cal is forming 15–20 times fewer stars than Orion A (BF14). Auriga-Cal and Orion A are the most distant GBS clouds, both at ∼450 pc, with similar physical resolution and emission sensitivity. Furthermore, they share similar filamentary morphology (in contrast to Orion B, for example, which more resembles pockets of high density material), thus making Orion A an ideal and intriguing region for comparison. The SCUBA-2 coverage of the clouds is different than that of the *Spitzer* surveys. We consider only the fractional difference of *Spitzer*-identified YSOs within the SCUBA-2 coverage, of which there are 1309 in Orion A and 123 in Auriga-Cal. (The count for *Spitzer*-identified YSOs in Orion A is limited to those with detections in all 4 IRAC bands photometry as this is more similar to the source list of BF14, see discussion in Section 2.3.2.) Therefore there are 11 times more *Spitzer*-identified YSOs in Orion A than in Auriga-Cal within the areas observed by SCUBA-2.

We investigate how this fraction extends to YSOs observable in the submillimeter by comparing the number of compact sources in Orion A and Auriga-Cal, as observed with SCUBA-2. We use a *getsources* extraction from JCMT GBS observations of Orion A (Lane et al., in prep.), to ensure the comparison is unbiased by source identification algorithms. We take the final catalog produced by *getsources* and perform the same cuts on flux and geometry as we did for sources in Auriga-Cal (see Section 3.3.1) to identify a total of 295 compact sources. We do not do a visual vetting and source catalog comparison for the Orion A compact source list for this purpose and so we compare this total number of compact sources in Orion A (295) with the number of compact sources identified in Auriga-Cal (38) rather than the number of candidate YSOs (36). There are 8 times more submm compact sources in Orion A.

The ratios of YSOs in Auriga-Cal relative to Orion A observed with *Spitzer* and SCUBA-2 (11 and 8 times fewer, respectively) are consistent and therefore show that the disparity between the two clouds of the number of star-forming objects observed in the infrared extends to the submillimeter. This difference in star formation is attributed to the difference in mass at high density between the two clouds (Lada et al., 2009) of about an order of magnitude. The similar ratios for the embedded and the non-embedded populations in Auriga-Cal and Orion A suggests that there has been no significant differences in the relative star formation rates over the Class II lifetime, as there is not a larger fraction of YSOs about to form. This implies that Auriga-Cal is not expected to be as productive as Orion A for the foreseeable future.

3.4 Conclusion

We analyzed the SCUBA-2 observations of Auriga-Cal at 850 μm and 450 μm as part of the JCMT GBS. We identified 38 compact sources in the SCUBA-2 maps using the *getsources* algorithm and find 36 objects which we identify as candidate YSOs on the basis of the SCUBA-2 data alone. The majority of compact sources are co-located with cloud emission, consistent with observations of YSOs along natal filaments (André et al., 2010). Consequently, our sensitivity to YSOs is limited by the brightness of the cloud emission and therefore we do not expect our census of YSOs to be complete to the depth of the observations. More candidate YSOs are identified at 450 μm than at 850 μm. This difference is thought to be in part due to the higher resolution. The YSOs, however, are brighter at 450 μm and the contrast there is increased between the compact sources and the cold background emission, as these candidate YSOs are generally in the brightest areas of cloud emission, predominately around LkHα 101. The candidates with low SNR at 850 μm also tend to be those with larger sizes ($>20''$) suggesting that either of these characteristics could be responsible for the difficulty isolating the candidate YSO from the cloud emission. Given the complexity and richness of LkHα 101 cluster, the only way to get a census of YSO circumstellar masses in this region is likely with spatially-filtered interferometric observations.

We compared our catalog of candidate YSOs in SCUBA-2 maps with catalogs of *Spitzer* and *Herschel*/PACS YSOs. Half of the SCUBA-2 candidate YSOs (18 out of 36) are associated with an infrared-identified YSO and therefore are deemed to be robust protostellar objects. The majority of the remaining SCUBA-2 candidate YSOs are in areas of bright background emission, mainly the arc of emission near LkHα 101 where it is particularly difficult to identify YSOs. For this reason, we used the sum within a $20''$ aperture on *Herschel*/PACS 70 μm maps centred on the locations of these objects to measure an upper limit on their respective 70 μm flux. These upper limits (shown in Figures 3.6 and 3.7) are above the 70 μm fluxes of YSOs detected with *Herschel*/PACS, and so we could not confirm or rule out whether these sources are indeed protostellar. We therefore continue to refer to these sources as candidate protostellar objects based on the detection of compact emission at submillimeter wavelengths.

We measured the fluxes of candidate YSOs using aperture photometry on 850 μm maps and 450 μm maps that were convolved to the 850 μm beam size, to sample emission on similar scales. We complemented our analysis with *Herschel*/SPIRE data by using *getsources* to extract the fluxes at SPIRE wavelengths given the locations of the identified SCUBA-2 candidate YSOs, as *getsources* is optimized for *Herschel* maps.

SCUBA-2 fluxes were used to measure the masses of the circumstellar material (disk +

envelope) where the envelope has a larger contribution to the total mass for earlier Class objects. We assumed a temperature of 20 K and a β value of 1.5 for the mass calculation. This value of β is to account for the steeper submillimeter spectral slope between 450 μm and 850 μm and is consistent with values measured toward early Class protostars in Perseus (Chen et al., submitted)

Finally, we compared the ratios of submillimeter-detected compact objects (associated with candidate YSOs) to *Spitzer*-identified YSOs with 5 band photometry for Auriga-Cal and Orion A. We found the ratios for the two clouds to be consistent within the uncertainties (31$\pm$8% for Auriga-Cal and 23$\pm$2% for Orion A) showing that the disparity of star formation populations between the clouds observed in the infrared extends to the submillimeter. This similarity shows that the relative star formation rates of the two clouds has not varied over the Class II lifetime and suggests that Auriga-Cal will maintain a paltry population of stellar objects with respect to Orion A.

Acknowledgements

H.B.F. and B.C.M. acknowledge a Discovery Grant from the Natural Science & Engineering Research Council (NSERC) of Canada. H.B.F. acknowledges support from the Alfred Bader Scholarship in Memory of Jean Royce administered by Queen's University, Canada. This research used the facilities of the Canadian Astronomy Data Centre operated by the National Research Council of Canada with the support of the Canadian Space Agency. This research also made use of APLpy (Robitaille & Bressert, 2012), an open-source plotting package for Python hosted at http://aplpy.github.com

Chapter 4

Planet formation potential in Auriga - the radio perspective

Investigators: Hannah Broekhoven-Fiene, Brenda C. Matthews, Gaspard Duchêne, James Di Francesco, Rita K. Mann, Cassandra Fallscheer, and Tyler L. Bourke

4.1 Introduction

Chapters 2 and 3 describe the identification of YSOs and the characterization of the star formation in Auriga-Cal. In this Chapter, we turn the discussion to the circumstellar disks of these YSOs to investigate their planet formation potential.

In previous chapters, we saw that despite Auriga-Cal having a high total mass in terms of material available for star formation, there is much less ongoing star formation than in Orion A, the other nearby giant molecular cloud with the same total mass. This difference is attributed to the difference in high density material in the cloud with Auriga-Cal having much less mass at high density. In this chapter, we turn from the questions about star formation potential to the questions about planet formation potential.

The main question we target in this chapter is whether or not protoplanetary disks in Auriga-Cal exhibit similar characteristics of planet formation as other protoplanetary disks do. The two key characteristics we investigate are the disk mass (and therefore the amount of material available to form planets, Section 1.3.1) and the evidence of grain growth (and therefore the earliest stages of planet formation, Section 1.3.2). Recall from Section 1.3.2 that grain growth to mm and cm sizes in protoplanetary disks from sub-micron sizes in the interstellar medium is an indicator of the earliest stages of planet formation to assemble the building blocks. Also recall that observations are sensitive to dust grains with sizes that are the same order of magnitude as the wavelength at which they are observed. In this chapter,

therefore, our VLA observations at 0.7 cm and 1.3 cm are sensitive to dust grain sizes in the cm regime.

Resolved imaging of protoplanetary disks across submm to cm wavelength regimes have shown a radial variation in the grain size distribution (e.g., Banzatti et al. 2011; Guilloteau et al. 2011; Pérez et al. 2012, 2015; Tazzari et al. 2016). A major contributor to this effort is the Disks@EVLA[1] program which targets 66 systems in the nearest star-forming regions (Taurus, Ophiuchus, and a few isolated systems). Specifically, these studies show that the maximum grain size of the distribution, $a_{\rm max}$, varies, with $a_{\rm max}$ of cm sizes in the inner disk regions $\lesssim$40 AU, and $a_{\rm max}$ of mm sizes in the outer regions. Other studies aim to investigate the vertical distribution of the grain size distribution to study grain growth and sedimentation (Melis et al., 2011). Preliminary results show a Class 0 disk with a dearth of cm-sized grains, indicated by a steepening of the slope from the mm ($\alpha_{\rm mm}\sim$1.93) to the cm ($\alpha_{\rm cm}\sim$2.87) regimes. This global $\alpha_{\rm cm}$, i.e., measured from the total disk flux, is similar for other individual disks that have been highlighted from first results coming out of the Disks@EVLA program (Pérez et al., 2015).

In this work, we aim to characterize radio bright YSOs, to measure the dust thermal emission associated with cm-sized dust grains. A survey of YSOs at 1.3 cm will characterize the total dust emission, indicative of the disk mass, for disks throughout the cloud. A subsample of these disks is also observed at 0.7 cm to measure the spectral slope in the cm regime, $\alpha_{\rm cm}$, and therefore characterize the grain growth in several disks. These YSOs are also observed at 3 cm where free-free emission is found to dominate, and therefore determine its contribution to the 0.7 cm and 1.3 cm observations which are sensitive to both the thermal dust emission and the free-free emission. Finally, the disks detected here identify bright YSOs which can be followed up in more detail in the cm wavelength regime for more in depth study of individual disks.

The 1.3 cm disk survey was originally part of the program 13A-476 which was to survey Class II disks (identified in Chapter 2) in Auriga-Cal. This program was granted filler time and so not all of the original proposed pointings, chosen to sample different regions of the cloud, were observed. The observed pointings were prioritized by the number of YSOs within the field of view (Class Is, Class Fs, and Class IIs) that could be simultaneously observed. The observing strategy for disks was revised for program 14A-462 to target Class IIs (identified in Chapter 2) that were brightest in *Herschel* maps from Harvey et al. (2013), which were the longest wavelength observations available at the time. This program was targeted at 0.7 cm, the VLA's highest observing frequency, where the dust thermal emission

[1]The Very Large Array was temporarily called the Expanded VLA, or EVLA, while extensive upgrades were being incorporated to recognize the improvements, before it was renamed the Jansky Very Large Array.

Band	Wavelength	Number of pointings	YSOs in fields	Primary beam (Field of view)	Array Configuration	Dominating source of emission
Q	0.7 cm	11	13	$1'$	D	Thermal dust emission
K	1.3 cm	15	69	$2'$	C	Thermal dust emission
X	3 cm	14	79	$4.5'$	A	Free-free emission

Table 4.1 VLA observation bands

in the disk is brightest, and 3 cm and 5cm to measure the levels of free-free emission and its spectral slope. Some of the targets overlapped with YSOs that had been observed with the 13A-476 program at 1.3 cm. The 0.7 cm observations were granted the highest priority status and all proposed pointings were observed. The 3 cm and 5 cm, having lower weather constraints, were granted filler status. None of the 5 cm observations were conducted and so we used the remaining time for 1.3 cm observations of any 13A-476 targets which did not otherwise have any measurements of the free-free emission. Finally, program 14B-406 was targeted at the Class IIs targets of the 14A-462 program which had not already been observed at 1.3 cm with the 13A-476 program. These three programs resulted in Class I, Class F, and Class II YSOs throughout the cloud being surveyed at 1.3 cm and 3 cm (owing to the larger field-of-view at these wavelengths) and a subset of survey sample, consisting of only the brightest Class II YSOs as seen in *Herschel* maps, being observed at 0.7 cm.

In Section 4.2, we describe the observations, data calibration, and measurements. In Section 4.3, we measure the fluxes at 3 cm (Section 4.3.1) to determine thelevel of free-free emission contamination at shorter wavelengths, at 1.3 cm (Section 4.3.2) to measure the mass distribution of YSOs in Auriga-Cal, and at 0.7 cm (Section 4.3.3) to measure the spectral slope and revisit the assumptions made to measure disk mass. In Section 4.4, we summarize the implications for protoplanetary disks in Auriga-Cal.

4.2 Observations

We observed at three VLA bands summarized in Table 4.1. 0.7 cm and 1.3 cm observations target the thermal dust emission. Observations at 3 cm are dominated by free-free emission. 1.3 cm observations were observed as part of programs 13A-476 and 14B-406. 0.7 cm and 3 cm observations were taken as part of 14A-462.[2]

The observations at different bands were taken in different array configurations to match the resolution better between observations at different wavelengths.[3] The 0.7 cm and 1.3 cm observations have a similar synthesized beam FWHM of $\sim 1''$. The 3 cm observations

[2]These programs can be found on the NRAO archive by program ID.

[3]Recall that resolution depends on both the wavelength of observation (proportional) and the size of the aperture (inversely proportional). Different array spacings, and therefore different aperture sizes, yield different resolutions.

have a slightly higher resolution ($\sim$0.3″ synthesized beam FWHM) as they were taken in A-configuration instead of B-configuration (which would have yielded a more similar synthesized beam size to the 0.7 cm and 1.3 cm observations) for practical time constraints of the thesis.

Observations were set up to use full polarization and 64 $\times$ 2 MHz channels with 3-bit digitization to provide the maximum possible bandwidth and optimize continuum sensitivity. Observations at 0.7 cm (44 GHz, Q-band) were centred at 41, 43, 45, 47 GHz for a total of 8 GHz bandwidth. Observations at 1.3 cm (22 GHz, K-band) were centred at 19, 21, 23, 25 GHz for a total of 8 GHz bandwidth. Observations at 3 cm (10 GHz, X-band) were centred at 9, 11 GHz for a total of 4 GHz bandwidth.

The primary beam, which determines the field-of-view of interferometric observations, is determined by the observing wavelength and the diameter of the dishes. 3 cm observations therefore have the largest field of view, and in some cases multiple 0.7 cm pointing are used to observe YSOs that were observed in a single 3 cm pointing. (Similarly, in some cases, multiple 0.7 cm pointings were used for YSOs within a single 1.3 cm pointing.) Figure 4.1 shows the all pointings and therefore the area we observed within Auriga-Cal with the VLA.

4.2.1 Calibration

The CASA software was used for calibration and analysis. All data were processed through the VLA calibration pipeline[4]. Briefly, the pipeline Hanning smooths the data channels, does basic flagging (online flags, shadowing, zeros, pointing scans, beginning of scans, the end channels of spectral windows and basebands) and radio frequency interference (RFI) flagging, and does the complex gain calibration, the bandpass calibration, and the absolute flux density calibration. Our observations used 3C147 as the absolute flux density calibrator and the bandpass calibrator. Complex gain calibration was done using J0418+3801 at 0.7 cm and 1.3 cm and J0414+3418 for 3 cm observations. J0414+3418 was also used for the pointing scans for 0.7 cm and 1.3 cm observations. Cycle times for complex gain calibrators were $\sim$5–6 min at 0.7 cm and 1.3 cm, and 15 min at 3 cm.

The VLA Pipeline is straightforward for continuum observations such as ours. The pipeline products were visually inspected to confirm there were no obvious problems with the calibration applied. For example, we checked that there were no jumps in the data in amplitude vs. time, phase vs. time, amplitude vs. frequency, phase vs. frequency, and amplitude vs. uv-distance for calibrators and science targets.

[4]https://science.nrao.edu/facilities/vla/data-processing/pipeline

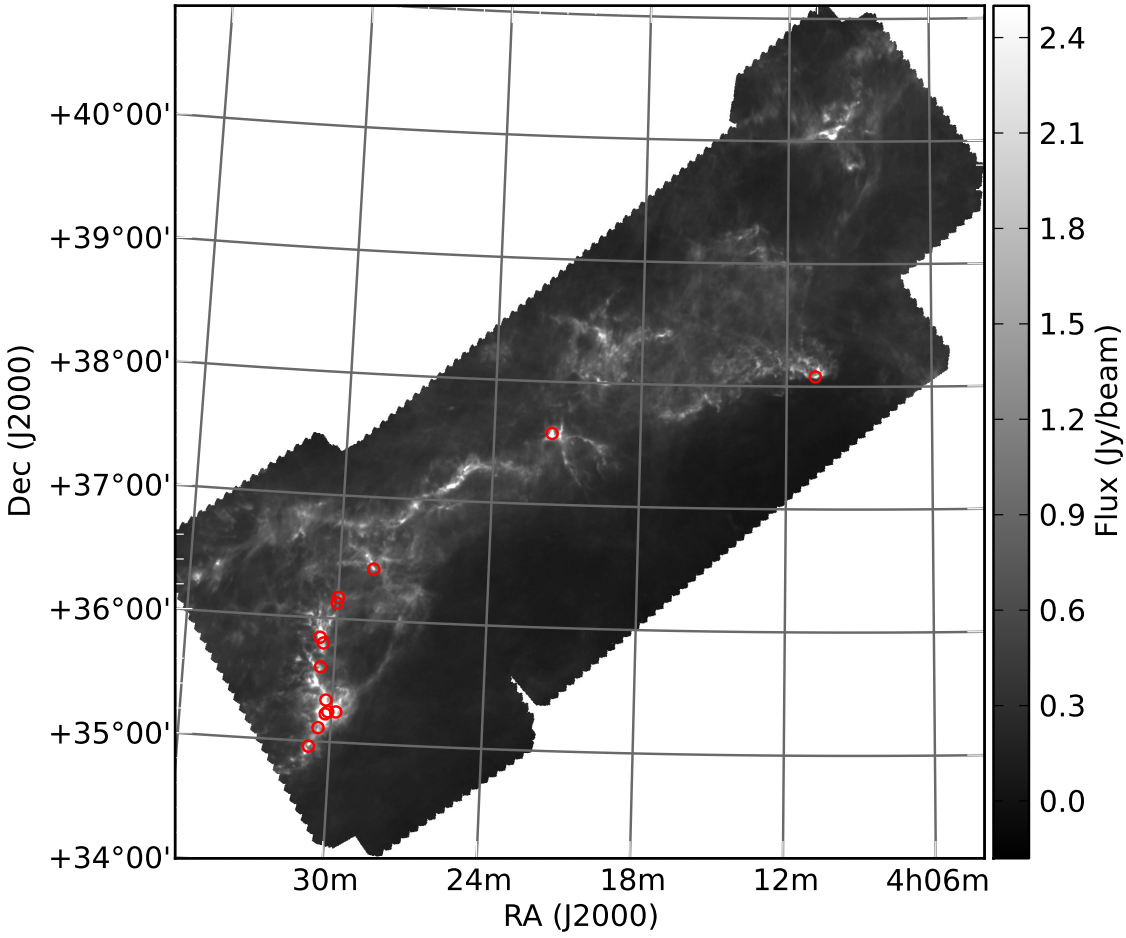

Figure 4.1 Fourteen 3 cm pointings are shown with red circles against the *Herschel* 500 μm greyscale backdrop. All 0.7 cm and 1.3 cm pointings are within the 3 cm fields.

4.2.2 Imaging

All fields are imaged using the CLEAN task in CASA using 0.3″, 0.2″, and 0.06″ pixel sizes at 0.7 cm, 1.3 cm and 3 cm, respectively, so as to have at least 5 pixels across the target beam sizes of ∼1.5″ (675 AU), ∼1″ (450 AU), and ∼0.3″ (150 AU), respectively. Images were cleaned interactively to a threshold of 3× the measured map rms. As YSOs are expected to be unresolved, we used natural weighting to maximize point source sensitivity. LkHα 101 was found to contribute emission significantly to fields within a few arcmin. Therefore LkHα 101 is simultaneously imaged using outlier fields in the CLEAN task while imaging these fields, however a number of these fields still contain some artifacts. Images of YSO 102 at 1.3 cm and 3 cm contain significant artifacts in a bright asterisk. This shape is due to the arrangement of the VLA dishes and is apparent for bright sources in images that have not been cleaned completely to model all the flux. The images of YSOs presented here are made from multiple observations of the same target target. Follow-up on cleaning each observation for YSO 102 individually results in less residuals.

4.2.3 Flux extraction

The tasks IMFIT and IMSTAT in CASA are used to measure fluxes and rms levels in the images. First, IMSTAT is used to measure the peak flux in a 7″ circular region and compare it to the rms measured in a 7″–15″ annulus, both centred on the expected YSO position. If a peak flux $> 5\sigma$ is measured, we follow-up using IMFIT on a 5″ region around the expected YSO position. Table 4.2 lists the measured fluxes and 3σ upper limits.

Our target rms at 1.3 cm of 3 μJy corresponds to a 5σ sensitivity to a disk mass of ∼0.02 $M_\odot$ at Auriga-Cal's distance (see Section 4.3.2). Our detection rate of 28% (21 out of 69) at 1.3 cm is consistent with the expectation to detect $\sim 1/3$ of disks given the mass distribution measured in other clouds, as our 1.3 cm survey was designed to sample YSOs throughout the cloud. Alternatively, our 0.7 cm observations were targeted at the brightest YSOs in *Herschel* maps and therefore we expect a slightly higher detection rate than what you would have randomly selecting YSOs in the cloud. Indeed we detect $\sim 1/2$ of the disks with detections of 5 of the 11 targeted YSOs at 0.7 cm. There are two additional YSOs within the field of view (AMC067 and AMC107) which may be marginally detected with peak fluxes of 4.5 × rms at their expected location, however we only include 5σ detections as robust detections. Additionally, we detect a YSO identified with *Herschel* (Harvey et al., 2013) and SCUBA-2 (Chapter 3), but not *Spitzer*, for a total of 6 YSOs detected at 0.7 cm. Finally at 3 cm, where we aim to constrain the contribution of free-free emission to shorter wavelengths of 1.3 cm and 0.7 cm, we detect 22% (15 out of 69) of the YSOs at 3 cm. Our target rms of 3.4 μJy was required to be sensitive to the lowest levels of free-free emission

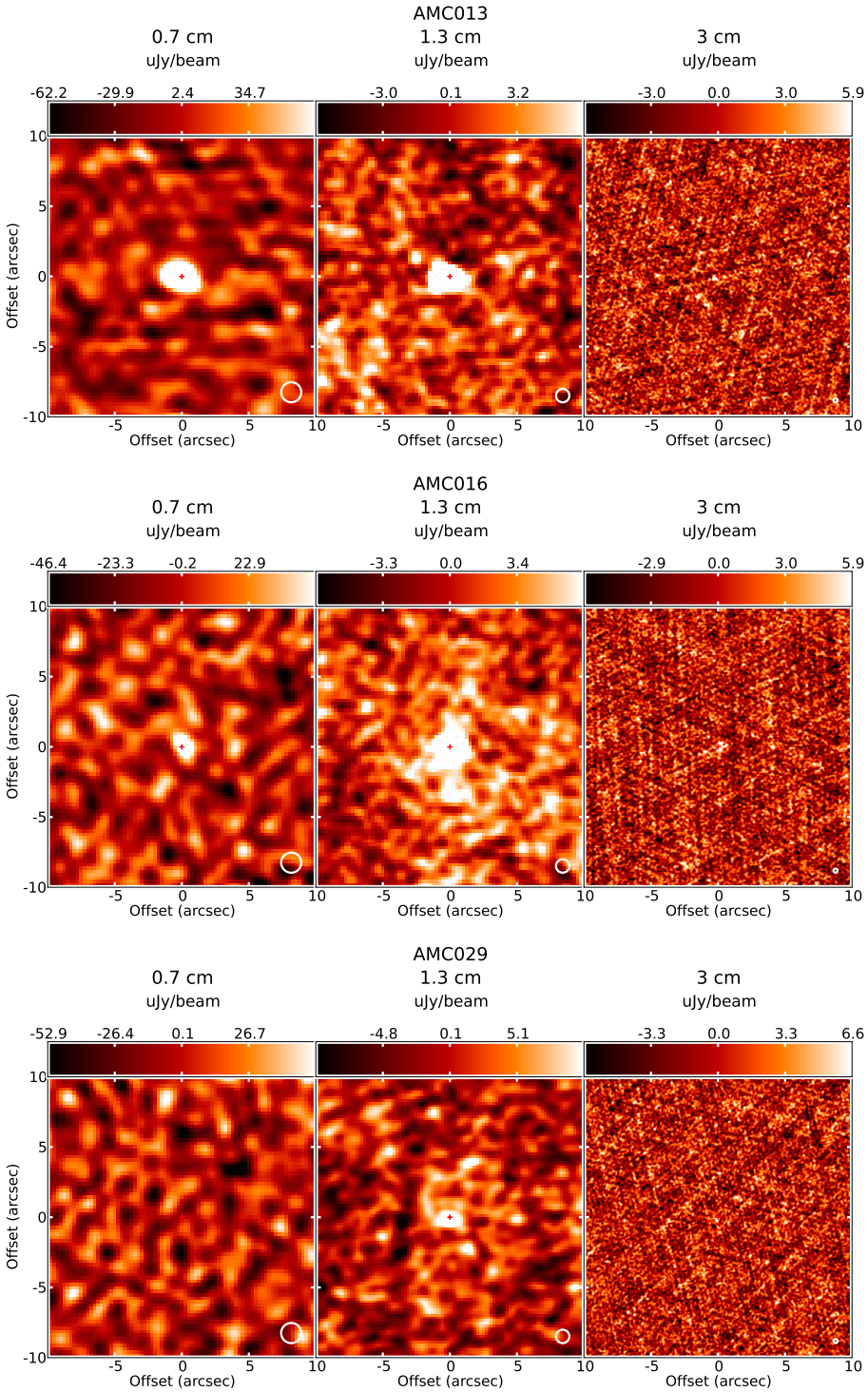

Figure 4.2 Continuum maps of YSOs observed at 0.7 cm (left), 1.3 cm (centre), and 3 cm (right) band. Each set of maps is labelled with the target name ("AMC" followed by the ID number from Chapter 2). Maps are linearly scaled from -3× to 10× the target RMS at each band of 15 μJy, 3 μJy, and 3.4 μJy, respectively. The crosshairs at the centre mark the expected position of the target YSO.

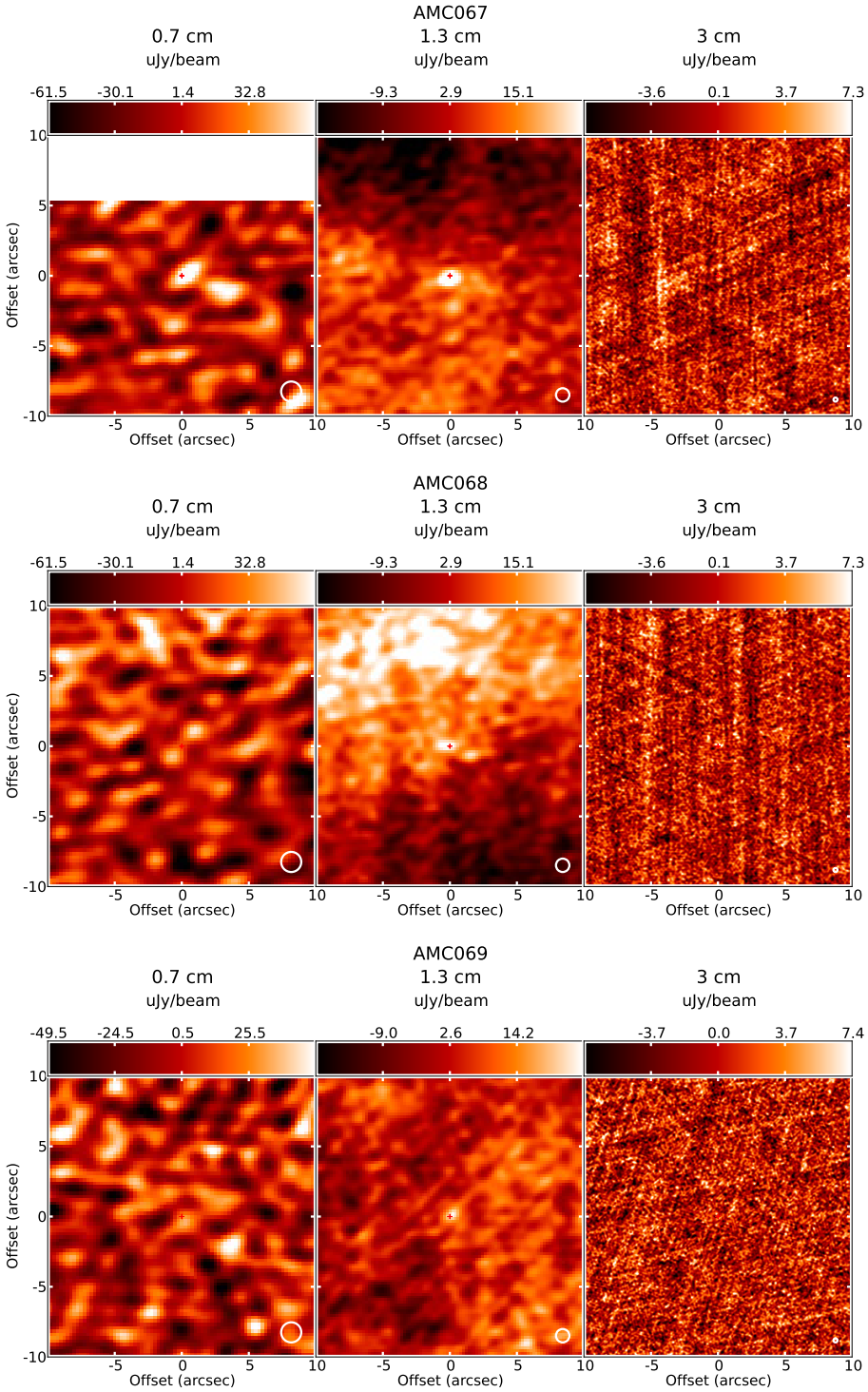

Figure 4.2 *continued* Note: In the top panel, the 0.7 cm image for YSO 68 is recentered on YSO 67 (which can be seen to be near the image edge).

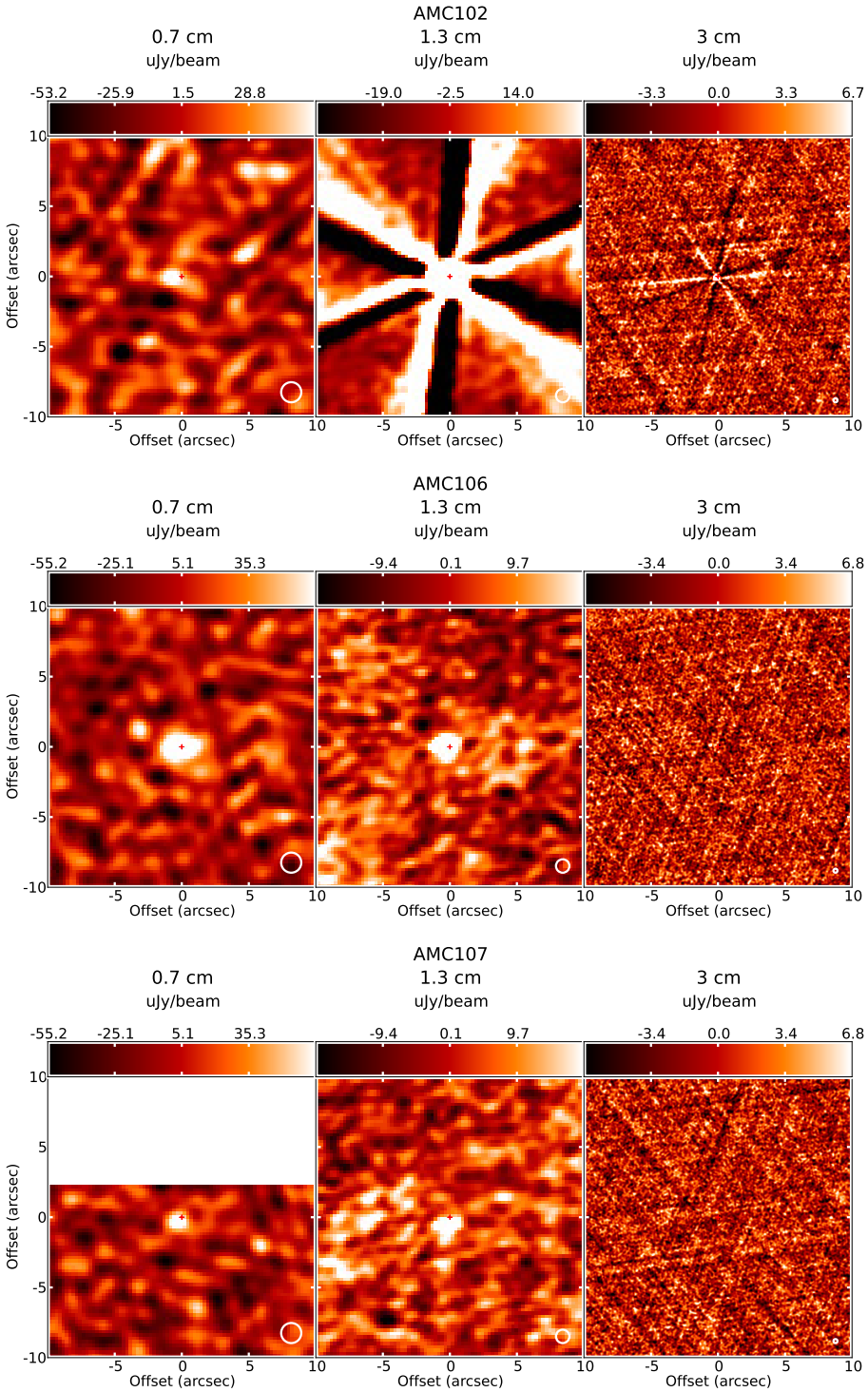

Figure 4.2 *continued* Note: In the top panel, the asterisk shape is due to significant flux from YSO 102 which is not accounted for in the image model. This is because this image is made from multiple observations where YSO 102 has varying flux levels (see text). In the bottom panel, the 0.7 cm image for YSO 106 is recentered on YSO 107 (which can be seen to be near the image edge).

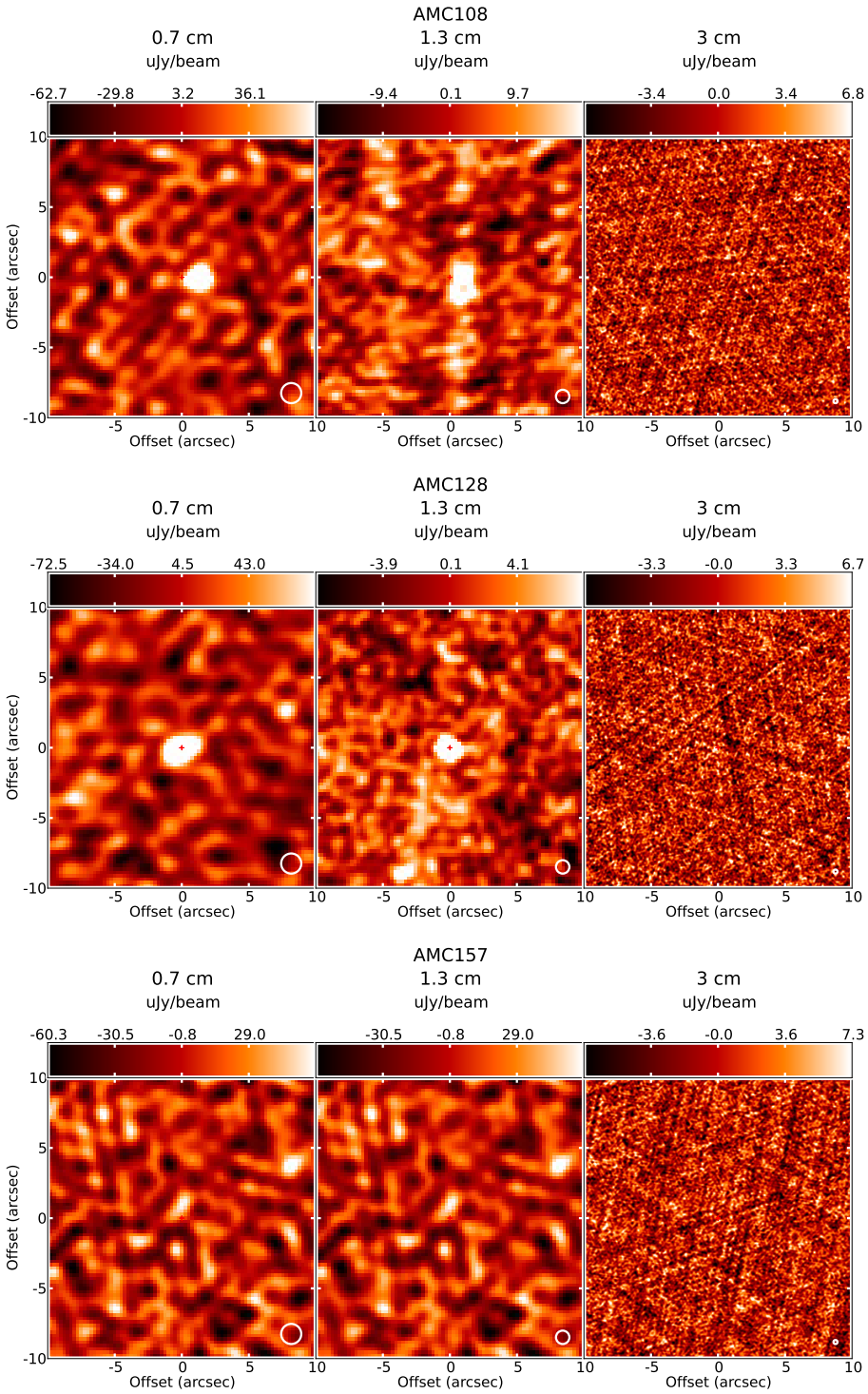

Figure 4.2 *continued*

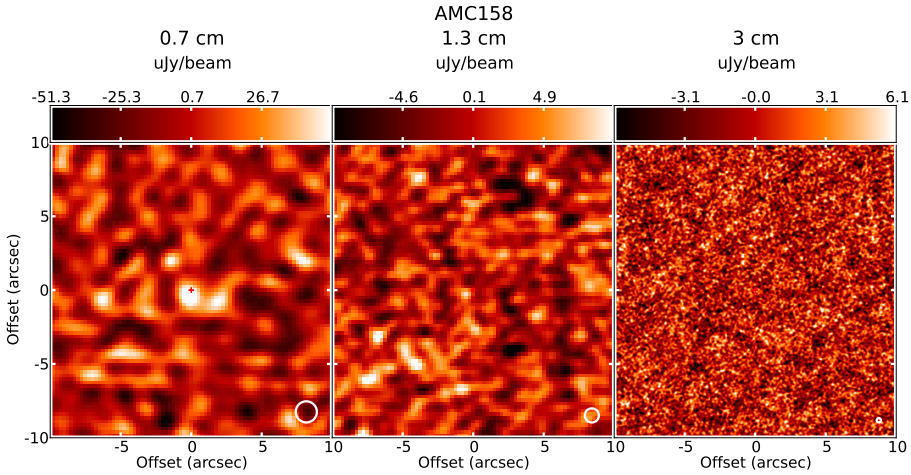

Figure 4.2 *continued*

Spitzer YSO ID	0.7 cm flux (μJy)	1.3 cm flux (μJy)	3 cm flux (μJy)
12	···	<6.8	···
13	249.4 ± 20.9	143.2 ± 2.7	31.3 ± 2.2
16	86.8 ± 16.1	73.9 ± 2.4	14.2 ± 2.2
17	···	<7.2	···
18	···	21.9 ± 2.4	···
28	···	<11.4	<7.1
29	<54.1	21.2 ± 4.0	16.2 ± 2.4
30	···	<12.0	<7.1
44	···	<13.2	<8.0
45	···	167.3 ± 8.0	<8.0
52	···	<12.7	<6.7
55	···	<31.5	12.5 ± 2.4
56	···	<23.5	<6.9
58	···	<18.5	<7.6
59	···	91.2 ± 8.9	<7.3
60	···	<37.0	<8.5
61	···	<17.9	30.7 ± 2.7
62	···	39.4 ± 7.0	13.8 ± 2.6
63	···	<43.4	22.1 ± 3.0
65	···	255.2 ± 15.3	<10.0
67	< 5.4	304.1 ± 57.2	<7.3
68	<72.2	<39.2	<7.3
69	<55.4	<21.9	<8.0
78	···	<18.3	<7.8

Table 4.2 Fluxes measured at 0.7 cm, 1.3 cm, and 3 cm

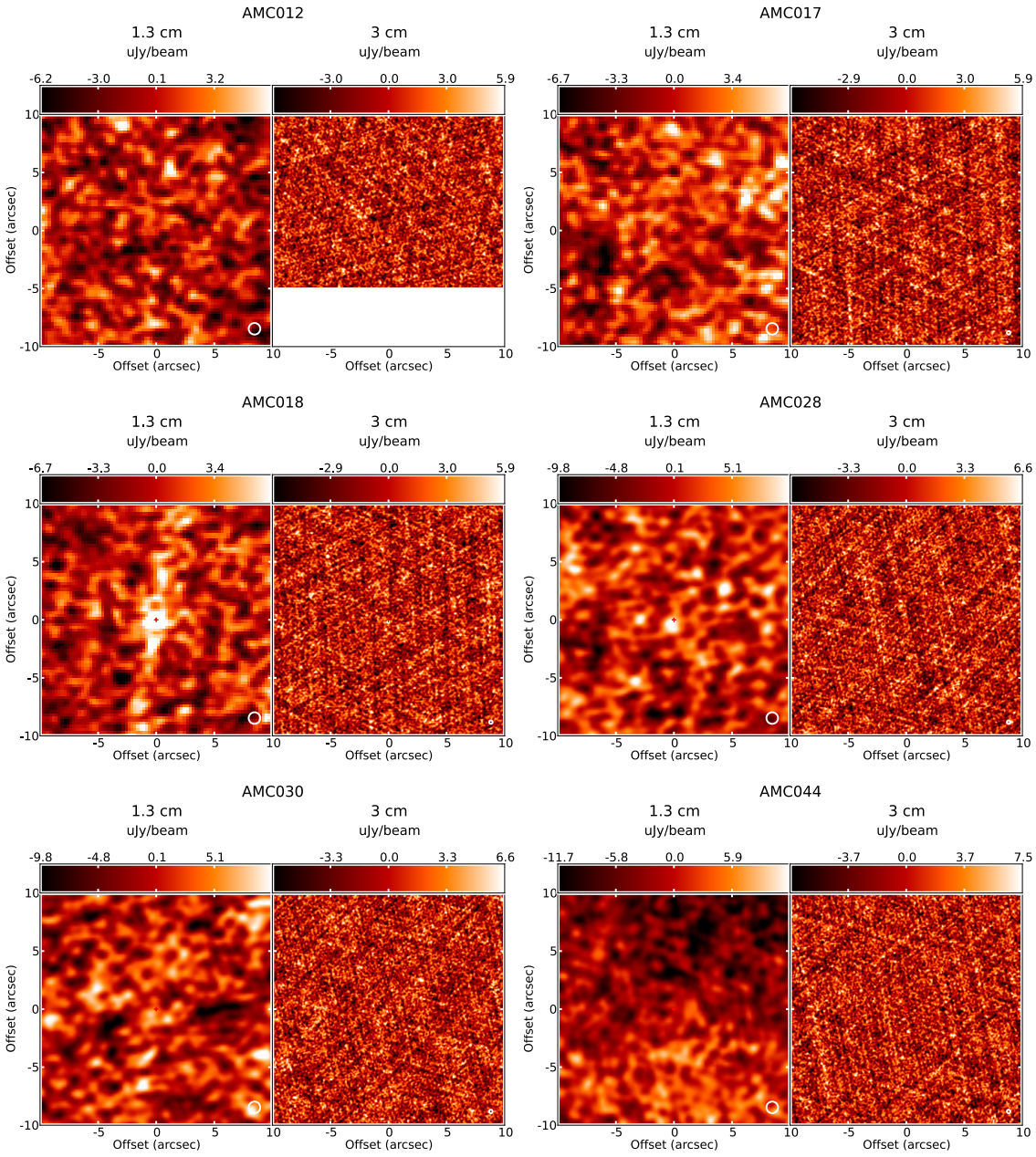

Figure 4.3 Continuum maps of YSOs observed at only 1.3 cm (left) and 3 cm (right). Each set of maps is labelled with the target name ("AMC" followed by the ID number from Chapter 2). Maps are linearly scaled from -3× to 10× the target RMS at each band of 3 μJy and 3.4 μJy, respectively. The crosshairs at the centre mark the expected position of the YSO.

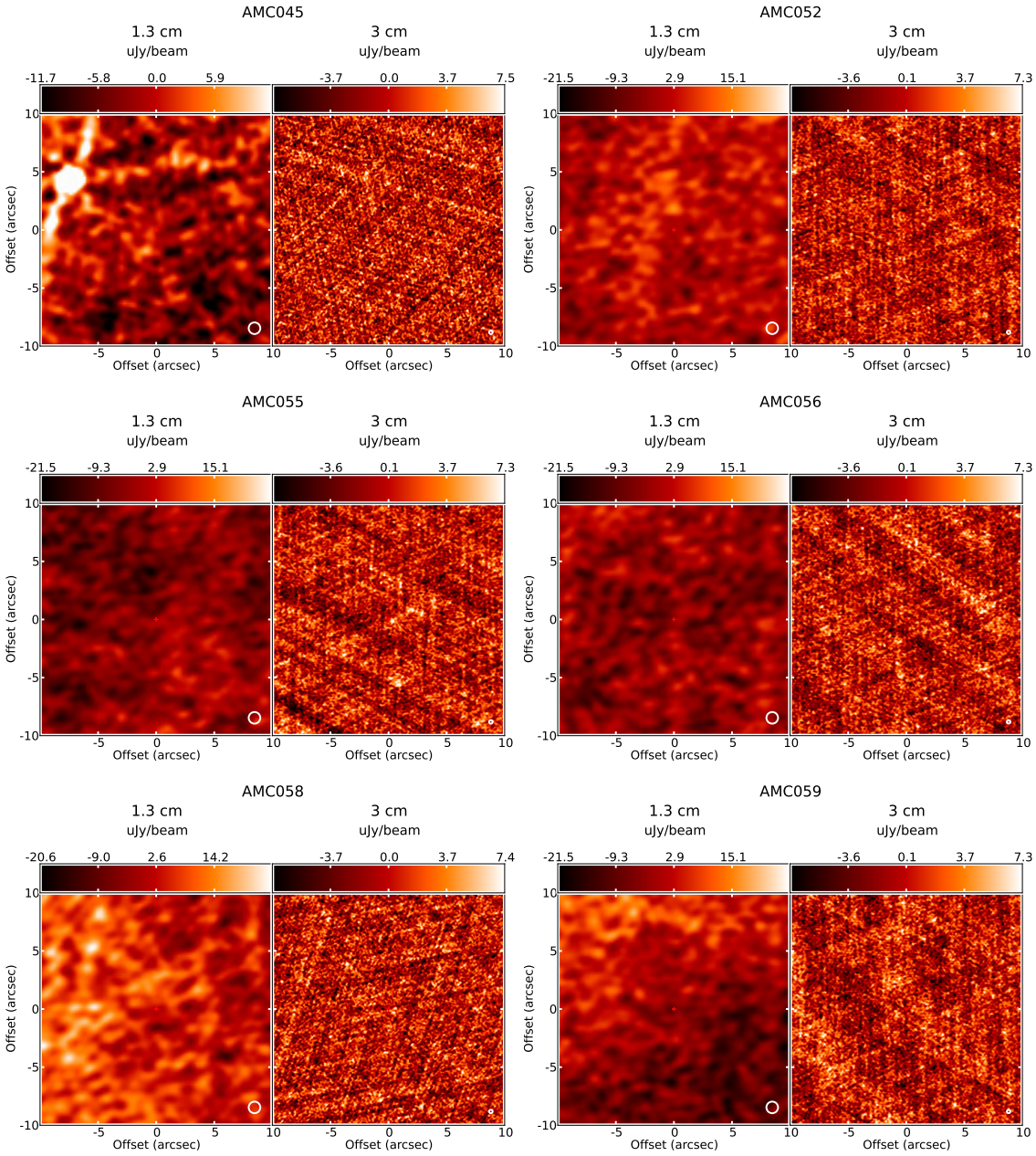

Figure 4.3 *continued*

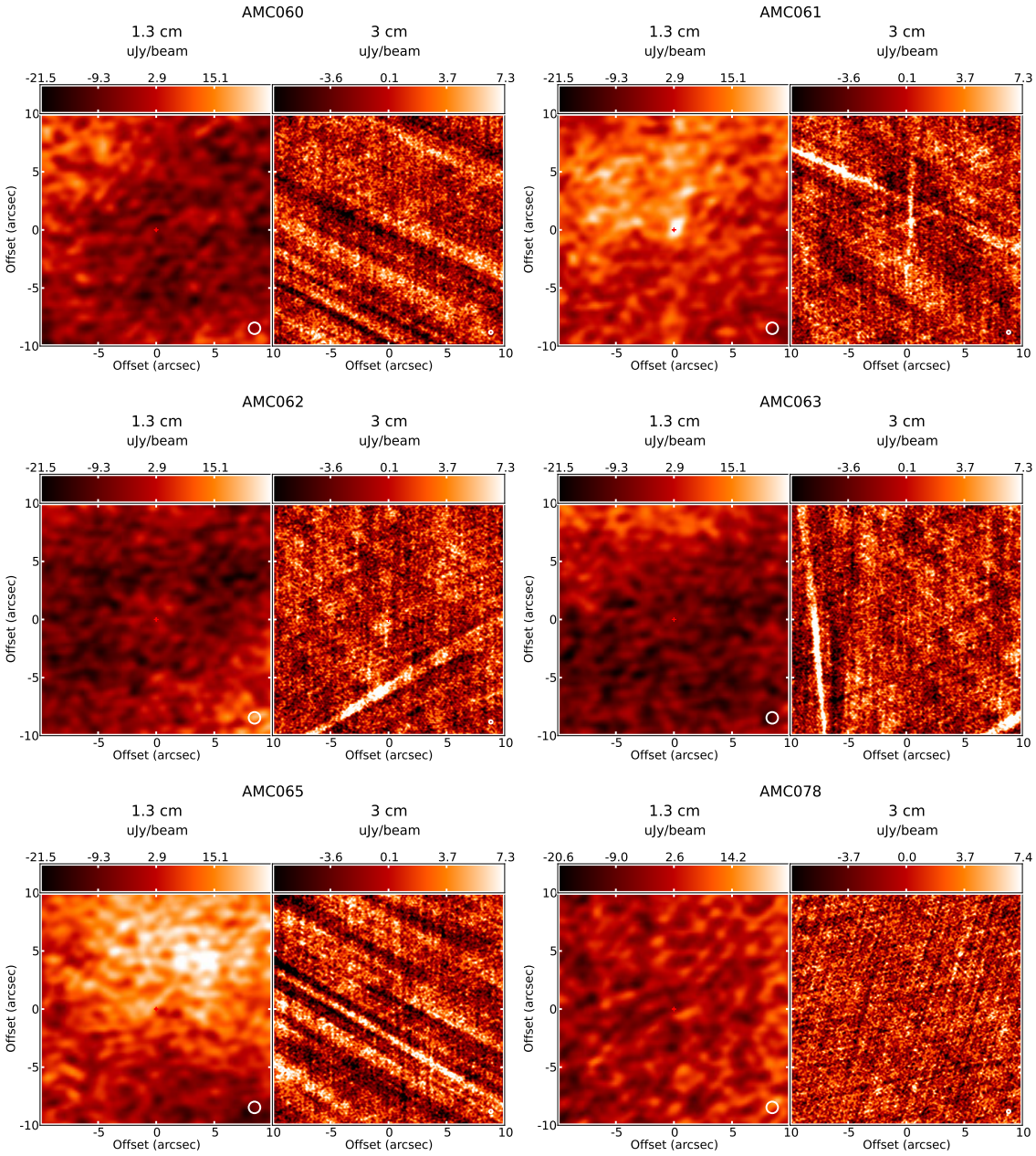

Figure 4.3 *continued*

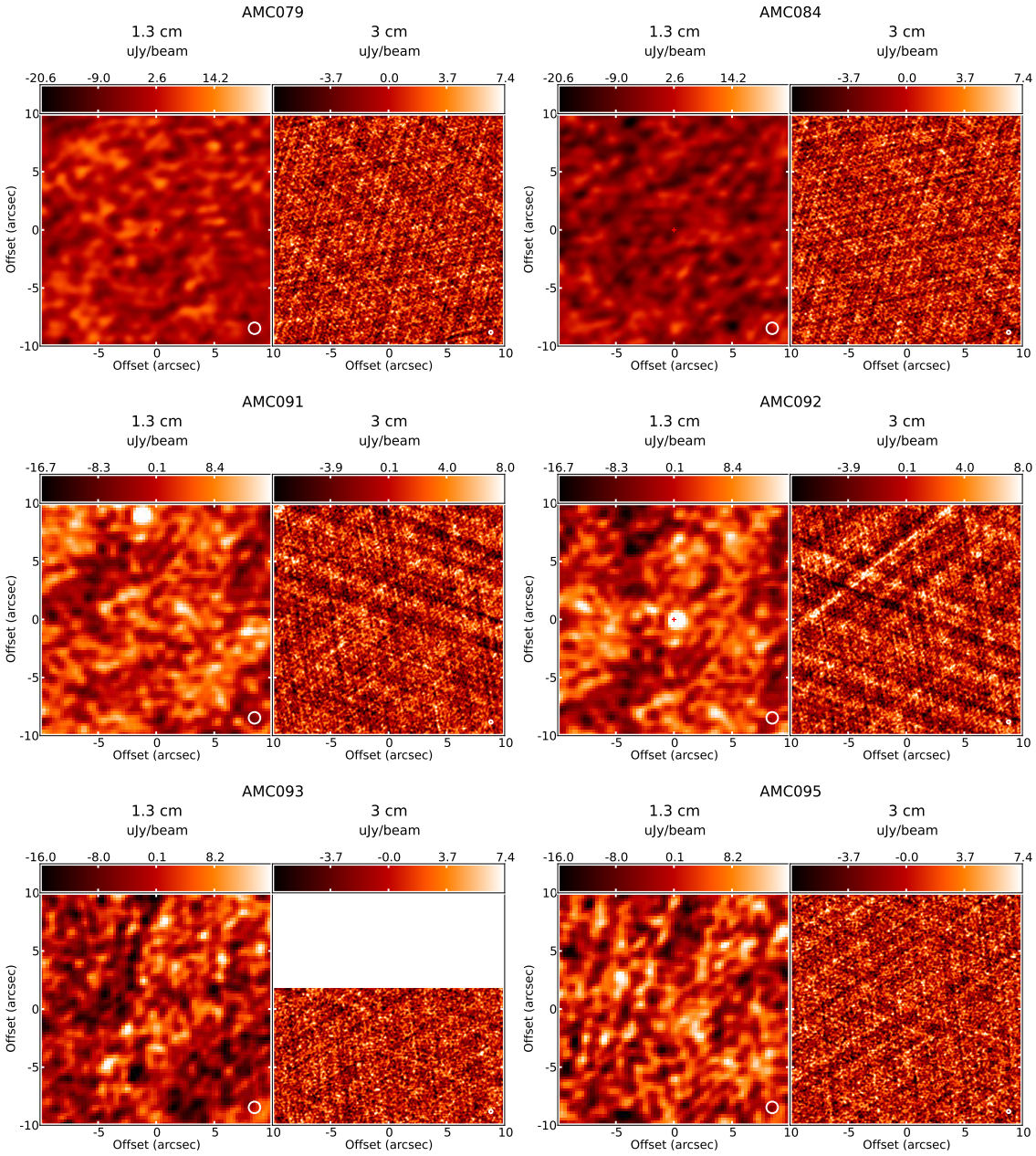

Figure 4.3 *continued*

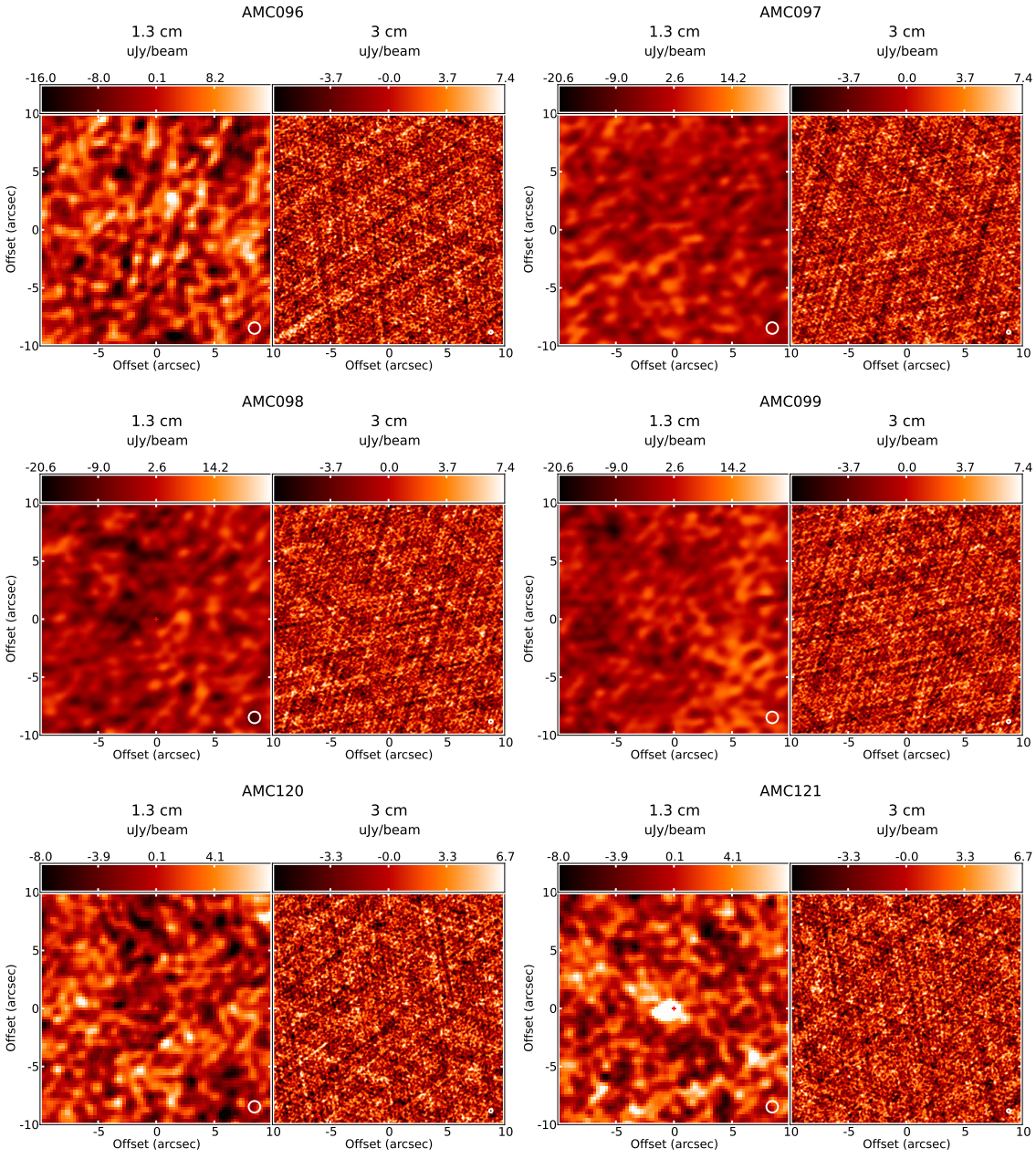

Figure 4.3 *continued*

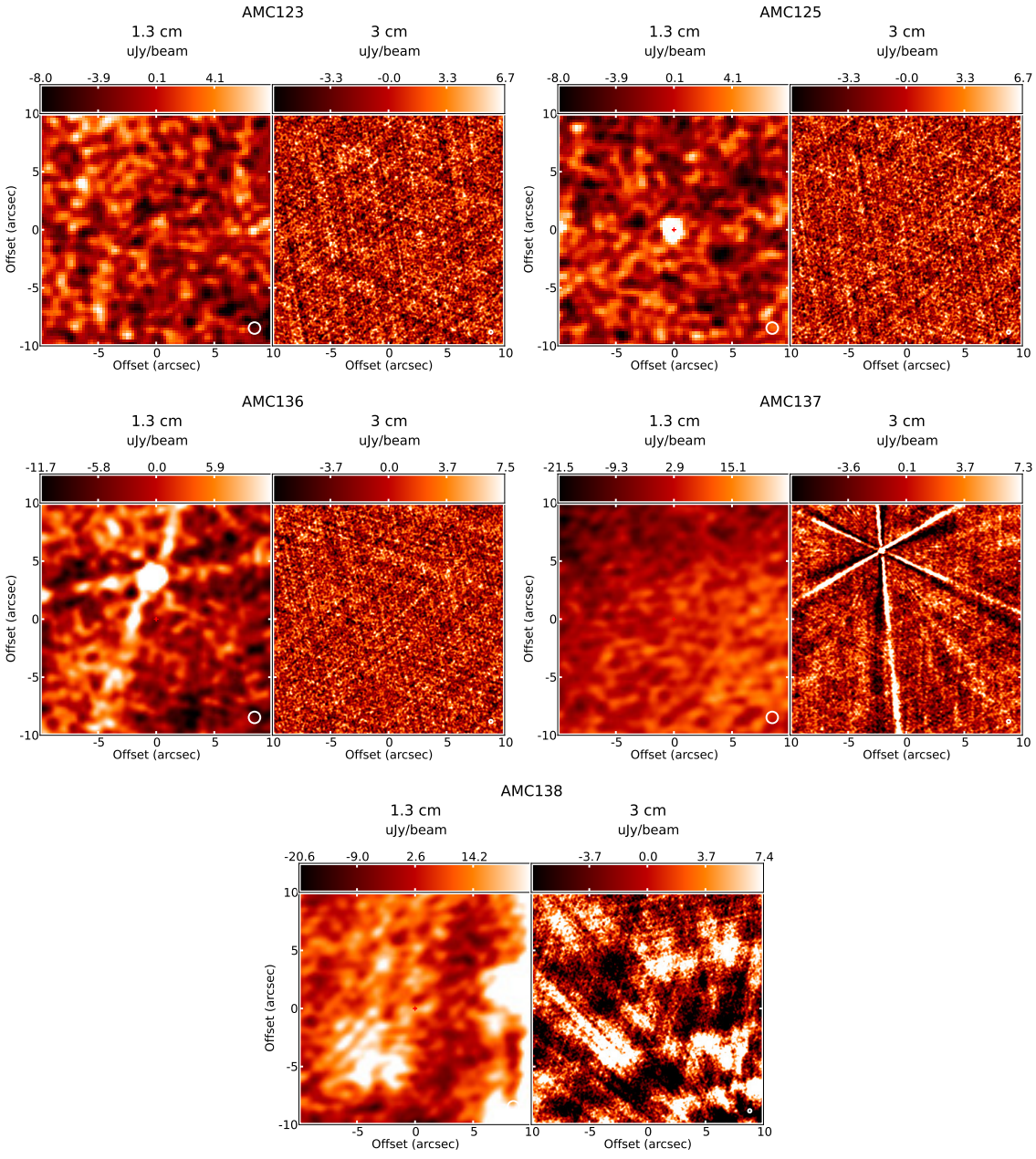

Figure 4.3 *continued*

Spitzer YSO ID	0.7 cm flux (μJy)	1.3 cm flux (μJy)	3 cm flux (μJy)
79	···	<14.6	<7.5
84	···	<14.2	<7.6
91	···	37.3 ± 5.2	<8.6
92	···	37.3 ± 5.8	<8.9
93	···	<16.6	···
95	···	<17.8	<8.1
96	···	69.8 ± 6.1	42.5 ± 2.7
97	···	<13.3	<7.5
98	···	<13.4	<7.4
99	···	<14.5	<7.3
102	<55.8	1440.3 ± 28.6	236.5 ± 2.5
106	235.4 ± 20.8	66.0 ± 7.4	15.3 ± 2.5
107	<5.4	38.9 ± 7.3	12.6 ± 2.5
108	223.2 ± 22.7	44.9 ± 6.5	<7.3
120	···	<8.1	<7.6
121	···	37.2 ± 2.9	<7.4
123	···	99.3 ± 6.3	<7.6
125	···	33.7 ± 3.0	<7.4
128	293.9 ± 25.7	37.5 ± 2.8	21.7 ± 2.6
136	···	167.3 ± 4.8	<8.0
137	···	<28.7	191.5 ± 3.2
138	···	<157.6	92.1 ± 10.5
157	<65.0	···	<8.0
158	<53.0	<9.6	<6.6

Table 4.2 *continued*

observed in Taurus (about 0.5 mJy) and scaled to Auriga-Cal's distance (Rodmann et al., 2006; Melis et al., 2011). This sensitivity is a factor of 4 deeper than observations at 3 cm of Orion, (Zapata et al., 2004; Felli et al., 1993) as high levels of free-free emission in Orion are due to the O star, θ^1 Ori C itself.

4.3 SED analysis

Figure 4.7 shows the SEDs of YSOs we have observed with the VLA. We have included the VLA fluxes measured here as well as fluxes measured with *Spitzer* (Chapter 2), *Herschel*(Harvey et al. 2013 and Chapter 3), SCUBA-2 (Chapter 3), as well as some ancillary data from USNO NOMAD and 2MASS catalogues. In this Section, we discuss the measured VLA fluxes in the context of the SED of thermal dust emission and the free-free emission.

4.3.1 Free-free emission and contamination at shorter wavelengths

At such long wavelengths, contamination from free-free emission must be constrained in some way so that the mass-tracing thermal emission from dust can be measured. There are several approaches that have been used to determine free-free contributions. If data from other observing campaigns are available at longer wavelengths, the level of free-free emission at wavelengths of science observations can be extrapolated assuming an emission profile of $F_\nu \propto \nu^{-0.1}$, as done by Mann & Williams (2009b, 2010); Mann et al. (2014) for disks in the Orion Nebula Cluster (ONC); and Mann et al. (2015) for the NGC 2024 cluster. In this case, Mann & Williams described a range of free-free contamination for their 880 μm observation due to the variability of intensity of observations of a given source. [5] In higher-resolution studies, such as the Disks@EVLA[6] project, contributions of free-free emission and dust emission to the total flux can be spatially separated. Emission centrally located on the star is attributed to free-free emission, and the dust emission is distributed in the disk (e.g., Pérez et al. 2015). In other studies in the cm regime, where high-resolution data are not available and all emission is included in a single flux, observations at longer wavelengths are used to constrain the level and slope of emission detected (e.g. Melis et al. 2011). The additional measurement of the spectral slope, where available, aids in confirming the nature of the emission.

[5]Note that levels of free-free emission are much higher in ONC due to the O star environment and so the free-free emission dominating over the dust emission continues to mm regime whereas in contrast to other star forming regions where the turn over is at much longer wavelengths.

[6]In the interim of the upgrades on the VLA, it was referred to as the Extended Very Large Array to distinguish it from earlier level of capabilities.

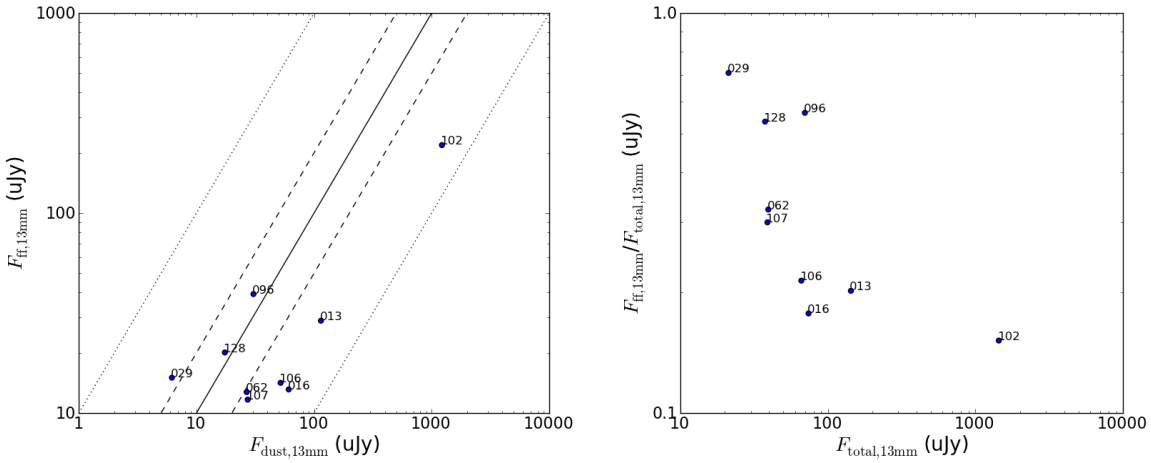

Figure 4.4 Left: the free-free emission at 1.3 cm extrapolated from 3 cm fluxes compared to the inferred dust flux (attributed to the remainder of the flux detected at 1.3 cm). The solid line shows the unity line where the extrapolated free-free emission and the inferred dust emission contribute equally to the total measured flux at 1.3 cm. The dashed and dotted lines show where the ratio of the contribution from one source of 1.3 cm emission (either free-free emission or dust thermal) is 2× and 10×, respectively, the other source of 1.3 cm emission. On the right, these values are shown as a fractional contamination to demonstrate that the lowest 1.3 cm flux disks suffer from the highest fractional contamination, which ranges from 15% to 71%.

In this work, all observations of disks are unresolved (unlike the Disks@EVLA program where the emission is spatially resolved) and we use the method of observations at longer wavelengths[7], specifically 3 cm, and assume the emission comes solely from free-free emission at this wavelength. We assume an emission profile of $F_\nu \propto \nu^{-0.1}$ (Pascucci et al., 2012) to extrapolate to 0.7 cm and 1.3 cm to constrain the contribution of free-free emission and isolate the levels of dust emission.

For YSOs with 3 cm detections, we assume the flux at 0.7 cm and 1.3 cm from dust emission to be:

$$F_{0.7,1.3\ \rm dust} = F_{0.7,1.3\ \rm total} - F_{0.7,1.3\ \rm ff} \tag{4.1}$$

where $F_{0.7,1.3\ \rm ff}$ is the level of free-free emission at 0.7 cm or 1.3 cm extrapolated from 3 cm flux assuming $F_\nu \propto \nu^{0.1}$, and $F_{0.7,1.3\ \rm total}$ is the total flux measured at 0.7 cm or 1.3 cm. For YSOs with flux upper limits at 3 cm, we assume $F_{0.7,1.3\ \rm dust} = F_{0.7,1.3\ \rm total}$ but use the upper limits on the 3 cm flux to quantify the maximum contribution of free-free emission to the 1.3

[7]Our program included X- and C-band (6 cm) observations to constrain the level of free-free emission and measure the spectral slope. Given the demand on the VLA during the semester of observations and the dynamic scheduling of the observations, however, no C-band observations were executed.

cm flux, $F_{0.7,1.3\ \mathrm{ff\ max}} = F_{0.7,1.3\ \mathrm{ff(rms)}} / F_{0.7,1.3\ \mathrm{total}}$, where $F_{0.7,1.3\ \mathrm{ff(rms)}}$ is the rms level at 3 cm extrapolated to 0.7 cm or 1.3 cm for the free-free emission profile assumed. Figure 4.4 shows the contamination of free-free emission at 1.3 cm for YSOs with both 1.3 cm and 3 cm detections. Figure 4.4 also shows the fractional contamination for these YSOs which ranges from 15% to 71%, with the faintest YSOs being subject to the highest fractional contamination from free-free emission. The measurements of free-free emission are shown on YSO SEDs in Figure 4.7. For those YSOs with detections at 3 cm, the assumed profile of the free-free emission is included to show the levels of free-free emission expected at the shorter wavelengths of 0.7 cm and 1.3 cm.

4.3.2 Disk masses

The disk masses are calculated from the 1.3 cm fluxes using

$$M = \frac{F_{1.3\ dust} D^2}{\kappa_\nu B_\nu(T_{dust})} \tag{4.2}$$

where D is the distance to the source, κ_ν is the opacity of the dust grains, and $B_\nu(T_{dust})$ is the Planck function for temperature, T_{dust}. The opacity is assumed to be $\kappa_\nu = 0.1(\nu/1000\ \mathrm{GHz})^\beta$ $\mathrm{cm}^2\ \mathrm{g}^{-1}$ (Beckwith et al., 1990). Note that the opacity relation includes an assumed dust-to-gas ratio of 1:100 and therefore M represents the total dust+gas mass. As a first estimate, we assume a dust temperature of 20 K and $\beta = 1$ (Andrews & Williams, 2005, 2007). This thermal dust emission profile is shown on the SEDs in Figure 4.7 for those YSOs with detections at 1.3 cm. This also puts the VLA fluxes in the context of the thermal emission measured at shorter wavelengths, specifically submm wavelength fluxes of Chapter 3, demonstrating that the observed levels of dust emission are agreeable between the different optically thin regimes.

Our sensitivity limits at 1.3 cm correspond to masses just above the minimum mass solar nebula (MMSN: the minimum mass required to form the Solar System) of 0.01 $\mathrm{M}_\odot$ (Weidenschilling, 1977). We detect a total of 19 disks at 1.3 cm, representing 28% of the YSOs within the observed fields (Table 4.2). This fraction is comparable to that in other Gould Belt clouds with masses measured in the submm/mm exceeding 0.01 $\mathrm{M}_\odot$. In Orion, 31% of the protoplanetary disks have masses that exceed the MMSN (Mann & Williams 2010), and ∼37% and 29% of disks in the low-mass star-forming regions of Taurus and Ophiuchus (Andrews & Williams 2005, 2007). This similarity suggests that the disk mass distribution in Auriga-Cal is like those to that in other nearby regions, should the mm disk mass distribution follow a similar trend as the cm disk mass distribution measured here.

Figure 4.5 shows the mass distribution measured from all 1.3 cm fluxes. The calculated disk masses versus YSO projected distances from LkHα 101 are also shown to determine

whether or not the proximity to the early B-star has an effect on disk mass. Figure 4.5 shows no dependence on distance from LkHα 101. The cm mass distribution in Auriga-Cal extends to higher masses than those measured in the mm regime for other clouds, such as Orion A (Mann & Williams, 2009b, 2010; Mann et al., 2014), Taurus (Andrews & Williams, 2005) or Ophiuchus (Andrews & Williams, 2007). This higher range suggests that more mass could be locked up in cm grains than in mm grains if Auriga-Cal has a similar mm mass distribution as other clouds (as yet, there is no existing comparable, i.e. interferometric, data set for Auriga-Cal that can establish this). The higher cm mass distribution could be an an indication of significant cm-sized pebbles and possible shallowing of slope at longer wavelengths.

The mass distribution has a similar maximum limit for all projected distances from LkHα 101 suggesting that the cm-sized grain population is unaffected by the early B-star's environment, regardless of what the mm mass distribution is. Resolved studies of protoplanetary disks at the 1 cm wavelength regime of more nearby disks show that there is a radial variation of the dust grain size distribution. The larger cm sized grains are found in the inner regions of the disk, typically within 40 AU, whereas in the outer regions, e.g. typically >70 AU, the maximum grain size is limited to $\sim$1 mm (Banzatti et al., 2011; Guilloteau et al., 2011; Pérez et al., 2012, 2015; Tazzari et al., 2016). For disks in Auriga-Cal, it is therefore perhaps unsurprising that the cm-mass distribution is unaffected by proximity to LkHα 101 given that cm-sized grains are predominantly located in the inner regions of disks and therefore would not be affected by any LkHα 101-caused truncation of the outer regions.

To put the Auriga-Cal disks in context, disks in the Orion Nebula Cluster (ONC) are known to have a truncated mm mass distribution (Mann & Williams, 2009a, 2010; Mann et al., 2014). Hence, we can use the ONC disks to verify whether or not we would expect the inner regions of disks in such an environment to be affected. Disks close (within 0.03 pc) to the massive O-star θ^1 Ori C are found to have truncated mass distributions. Namely, closer to the O-star, disks are eroded by the UV radiation from θ^1 Ori C. Since these observations are made in the submm/mm ($\sim$880 μm), they are sensitive to dust grains up to mm sizes, which are found do be distributed to much larger radii than the cm sized grains in nearby resolved disks. Figure 4.6 shows the measured sizes for resolved disks at 856 μm from Mann et al. (2014). This plot shows that the maximum sizes measured for disks declines as disks are closer to θ^1 Ori C. The maximum disk size closest to θ^1 Ori C is 154 AU, which is still beyond where we expect the cm-sized dust grains to be located within the disk. Therefore, since these disk sizes are not truncated to below $\sim$40 AU (the inner regions where cm-sized grains are found), we do not expect the cm-mass distribution to be truncated as the mm-mass distribution is. For disks in Auriga-Cal close to the early B star LkHα 101, however,

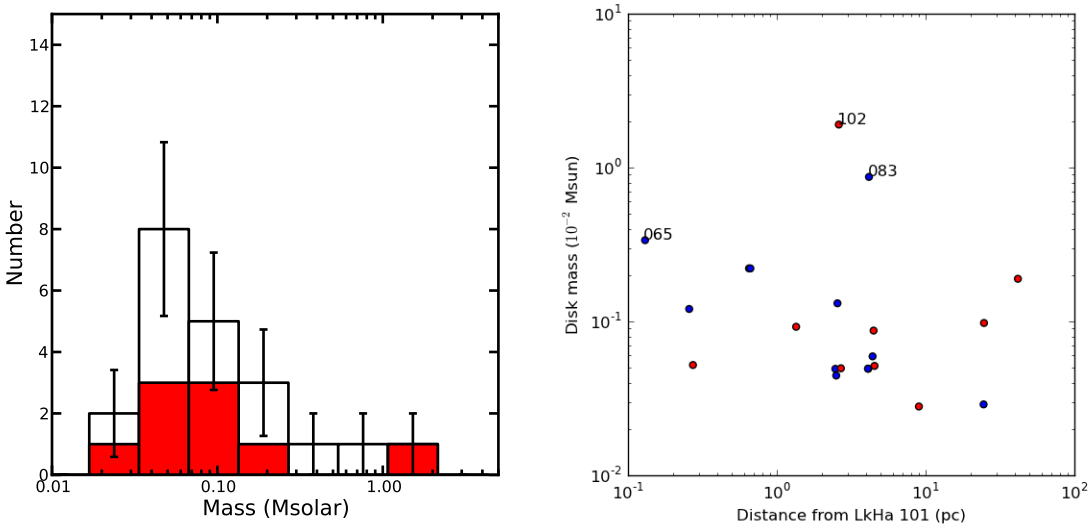

Figure 4.5 Disk mass distribution measured from 1.3 cm fluxes (left) assuming a dust temperature of 20 K and spectral slope $\alpha = 3$ from optically thin emission implying $\beta \sim 1$ (see text). The red bars mark the masses calculated from 1.3 cm fluxes decontaminated from free-free emission detected at 3 cm. Also shown is the disk mass versus the distance from LkHα 101 (left) indicating that cm grains are unaffected by proximity to the early B star. Blue points represent 1.3 cm fluxes that do not have free-free emission removed, due to no detection at 3 cm. Red points correspond to YSOs that have detections at 3 cm and therefore masses calculated from 1.3 cm fluxes that have been decontaminated from free-free emission.

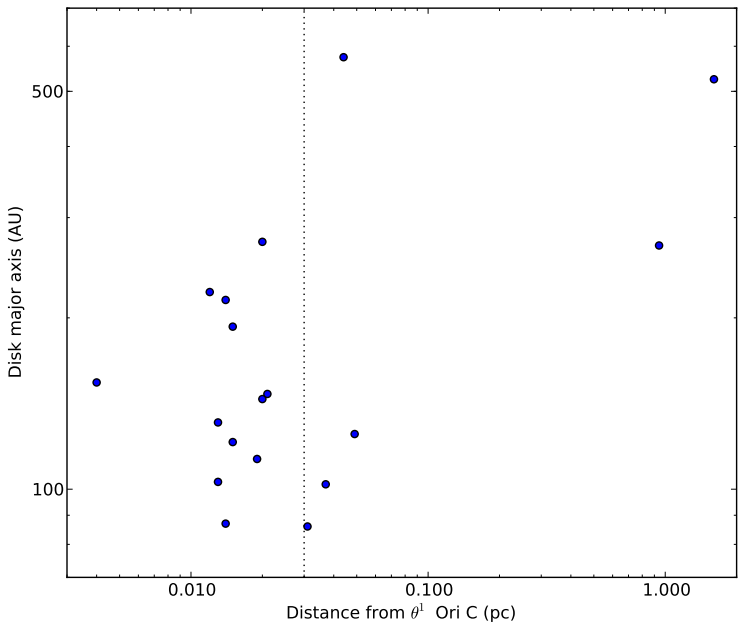

Figure 4.6 Disk sizes in the ONC with data from Mann et al. (2014) compared to their distance from θ^1 Ori C. Mann et al. show that disk masses measured in the submm are truncated for disks close to θ^1 Ori C. Specifically, disks have a range of masses, however within 0.03 pc (dotted line) the maximum of that range declines with proximity to θ^1 Ori C. Here we show that the disk geometrical size is similarly truncated within 0.03 pc. Closest to θ^1 Ori C this maximum size is truncated to 154 AU. This size scale is still within the outer regions of the disk and the erosion does not reach the inner regions where cm sized dust grains are found to be located. Therefore, we do not expect such a truncation of disk masses measured in the cm regardless of whether proximity to the early B star LkHα 101 similarly erodes the outer regions of disks (which is currently unknown).

YSO	$\alpha_{\rm cm}$
13	0.8963
16	0.2599
106	2.0542
108	2.5905
128	3.3260

Table 4.3 Spectral slopes measured between 0.7 cm and 1.3 cm for all YSOs detected ($> 5\sigma$) at both wavelengths

we cannot determine whether or not the radiation field from LkHα 101 is similarly eroding disks as we do not expect such erosion to reach the inner regions of the disk where the cm-sized dust grains are located.

4.3.3 Dust grain size distribution

For the mass calculation in Section 4.3.2, we assumed a standard opacity law that assumes a power-law spectral slope of β=1, typical for protoplanetary disks. This is the emission profile that is shown on the SEDs in Figure 4.7 for YSOs with detections at 1.3 cm. In this section, we use the subset of the 5 disks that are detected at 0.7 cm to measure directly their global spectral slope between 0.7 cm and 1.3 cm. Of the 13 YSOs observed at 0.7 cm. The spectral slopes between 0.7 cm and 1.3 cm, $\alpha_{\rm cm}$, are listed in Table 4.3. The spectral slope relative to the assumed profile of Equation 4.2 can be seen qualitatively in the SEDs of Figure 4.7.

YSOs 106, 108, and 128 have measured $\alpha_{\rm cm}$ consistent with what has been measured for other disks in the cm, such as CQ Tau ($\alpha_{\rm cm}$ = 2.6) and DoAr 25 ($\alpha_{\rm cm}$ = 2.8). For optically thin dust emission where $\alpha_{\rm cm} = 2 + \beta$, these values of $\alpha_{\rm cm}$ imply β in the range of 0-1, signifying grain growth to cm sizes. Therefore, in the disks around YSOs 106, 108, and 128, we infer the growth of cm-sized pebbles and therefore evidence of the earliest stages of planet formation.

Fortuitously, YSOs 108 and 128 were also observed with the Submillimeter Array (SMA) at 1.3 mm (PI Peterson). These are observations that are straightforward to compare to the VLA observations since they are also interferometric data and therefore also have large scale emission (such as that from the nascent cloud) spatially filtered out. Single dish fluxes, such as those from SCUBA-2 (Chapter 3) in contrast would include more large scale emission. The SMA fluxes (Tyler Bourke, private communication) are shown on the SEDs in Figure 4.7 and are consistent with the spectral slope $\alpha_{\rm cm}$ calculated here. This similarity suggests that this grain size distribution continues from mm to the cm, although this possibility cannot

be verified without at least a second flux in the mm regime to calculate $\alpha_{\rm mm}$ independently.

YSOs 13 and 16 have much shallower spectral slopes (0.9 and 0.3). These are more consistent with free-free emission. These YSOs are in the more northern regions of the cloud, with significantly less star formation than the southern region of the cloud (which contains 75% of the star formation in Auriga-Cal). It would be worthwhile to investigate whether or not there are different conditions in the more northern regions of the cloud, such as more variability of free-free emission for younger sources, which could account for this difference in $\alpha_{\rm cm}$.

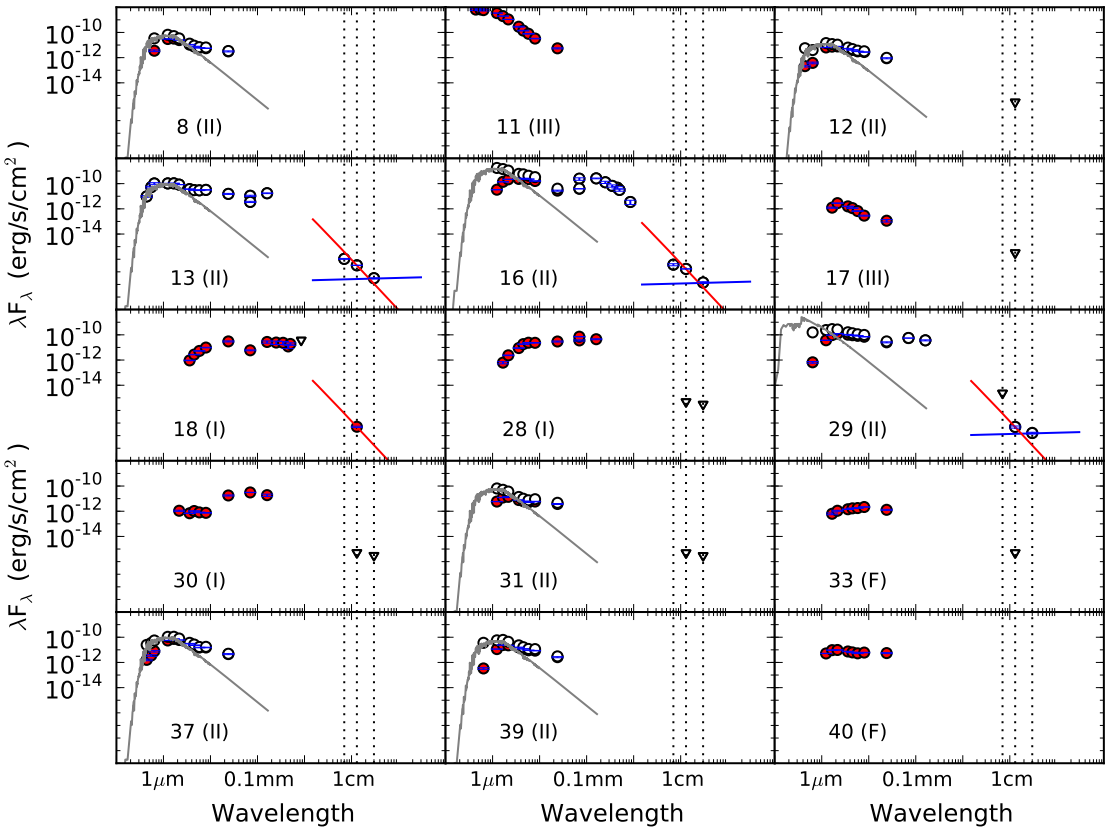

Figure 4.7 SEDs of YSOs observed with the VLA. The *Spitzer* ID for each YSO is shown in the lower left corner (with *Spitzer* determined SED Class in parentheses). Red circles show observed fluxes from other works (optical, 2MASS, *Spitzer*, *Herschel*, SCUBA-2) and this work are shown. Vertical dotted lines mark measurements from this work. For YSOs identified as Class IIs, a sample K7 stellar spectrum, normalized to the shortest near infrared flux, is plotted in grey. For these YSOs, an A_V value is estimated by matching the resultant de-reddened fluxes (overlaid white circles) to the K7 stellar spectrum. For YSOs with 3 cm detections, a blue line tracing the extrapolated emission is shown. Red lines show the dust thermal emission profile with masses calculated from 1.3 cm fluxes, assuming 20 K dust and $\beta = 1$ for optically thin emission. This profile is consistent with the subset of 0.7 cm measurements, with the exception of YSOs 13 and 16, which show slightly shallower profiles.

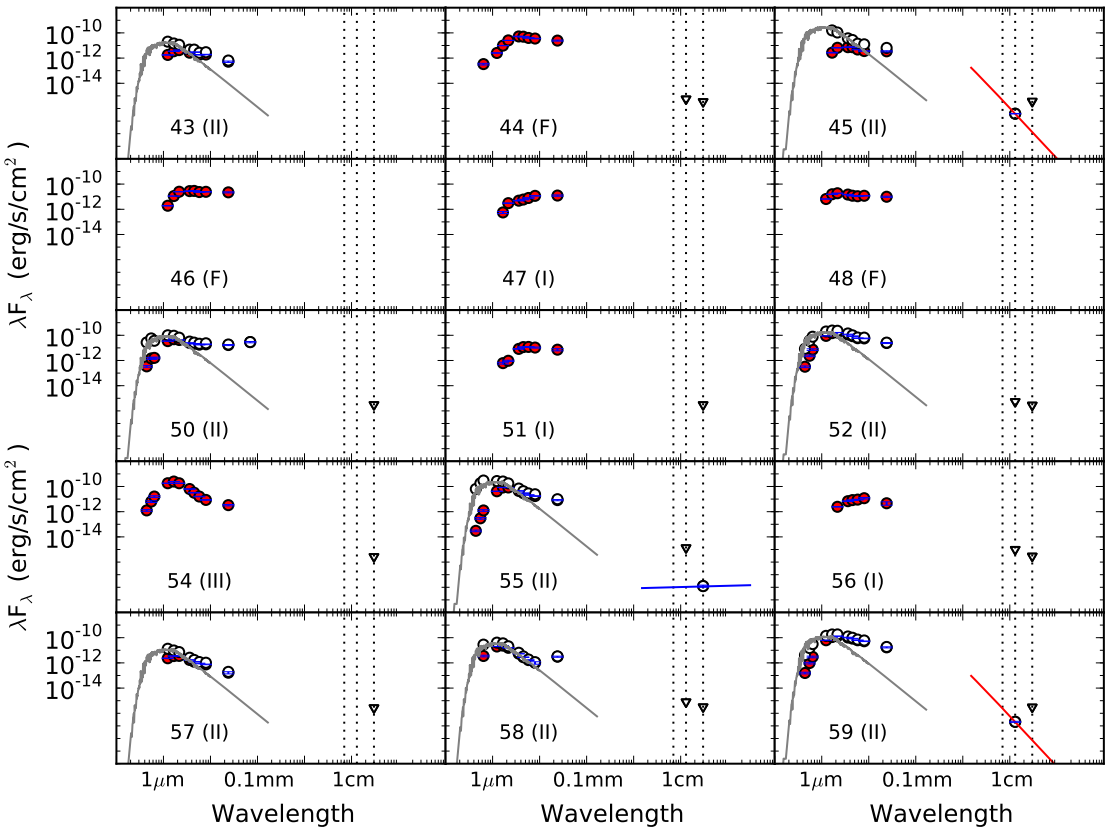

Figure 4.7 *continued*

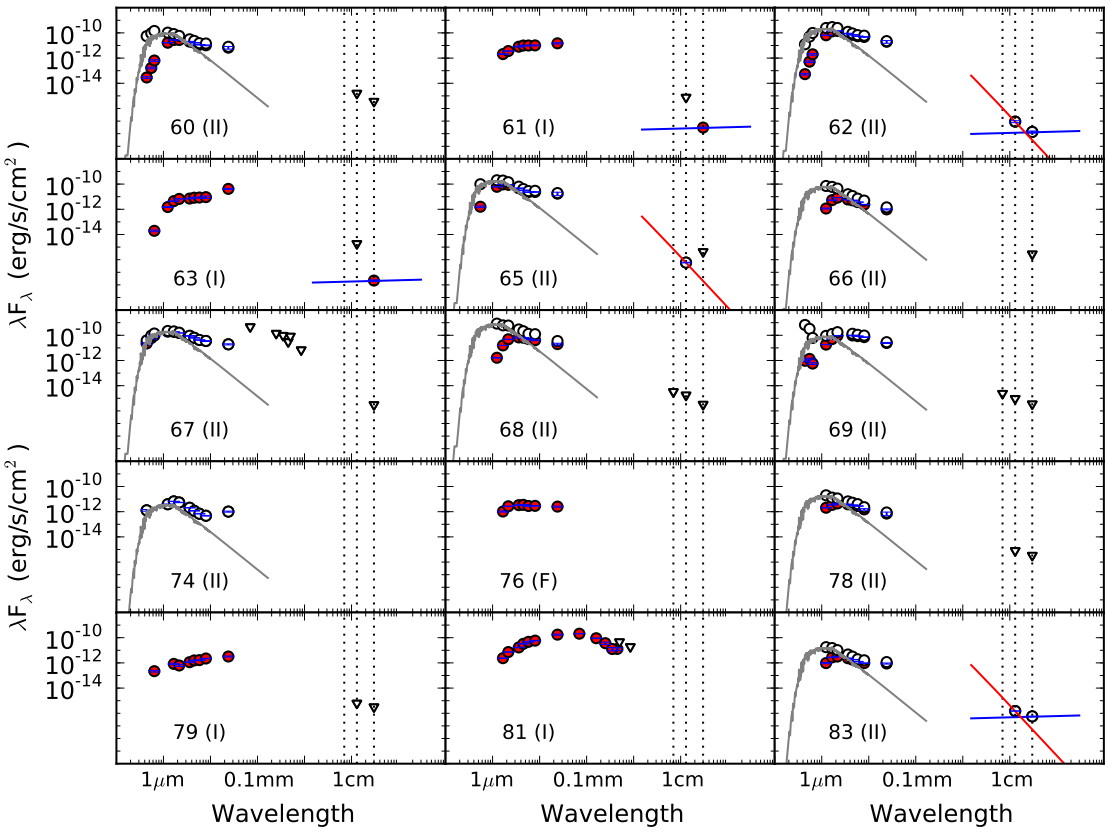

Figure 4.7 *continued*

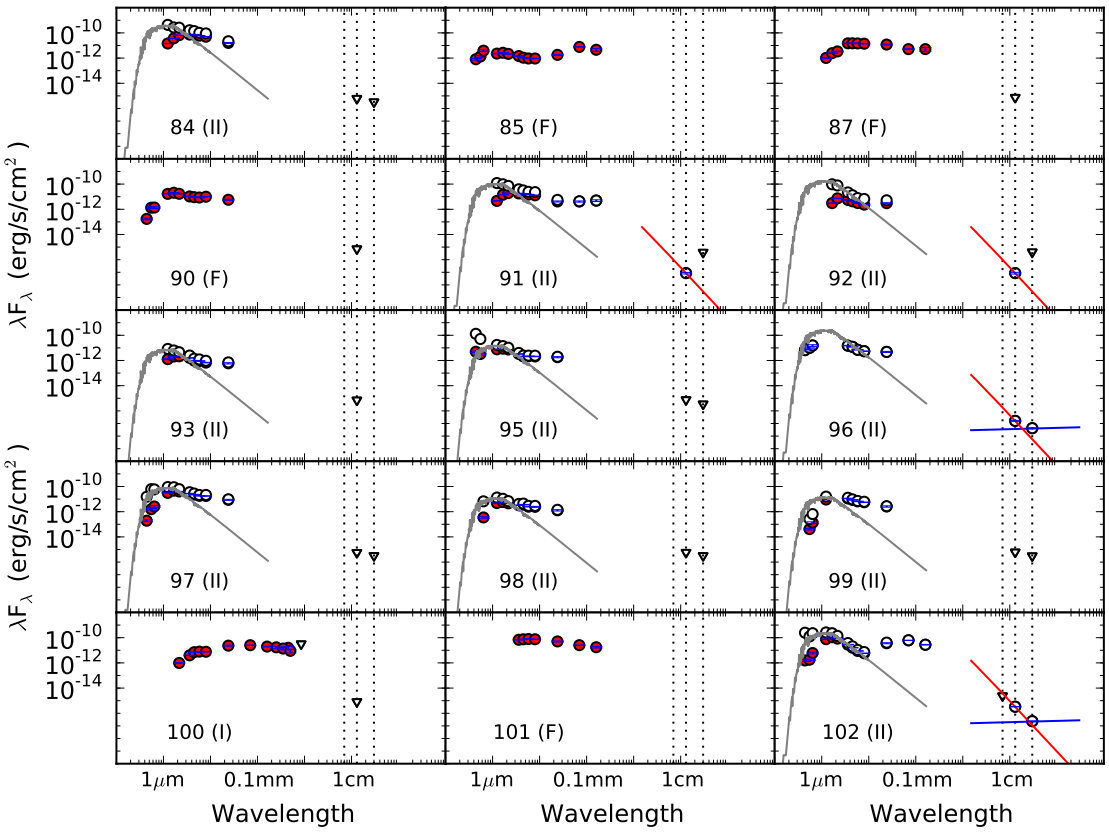

Figure 4.7 *continued*

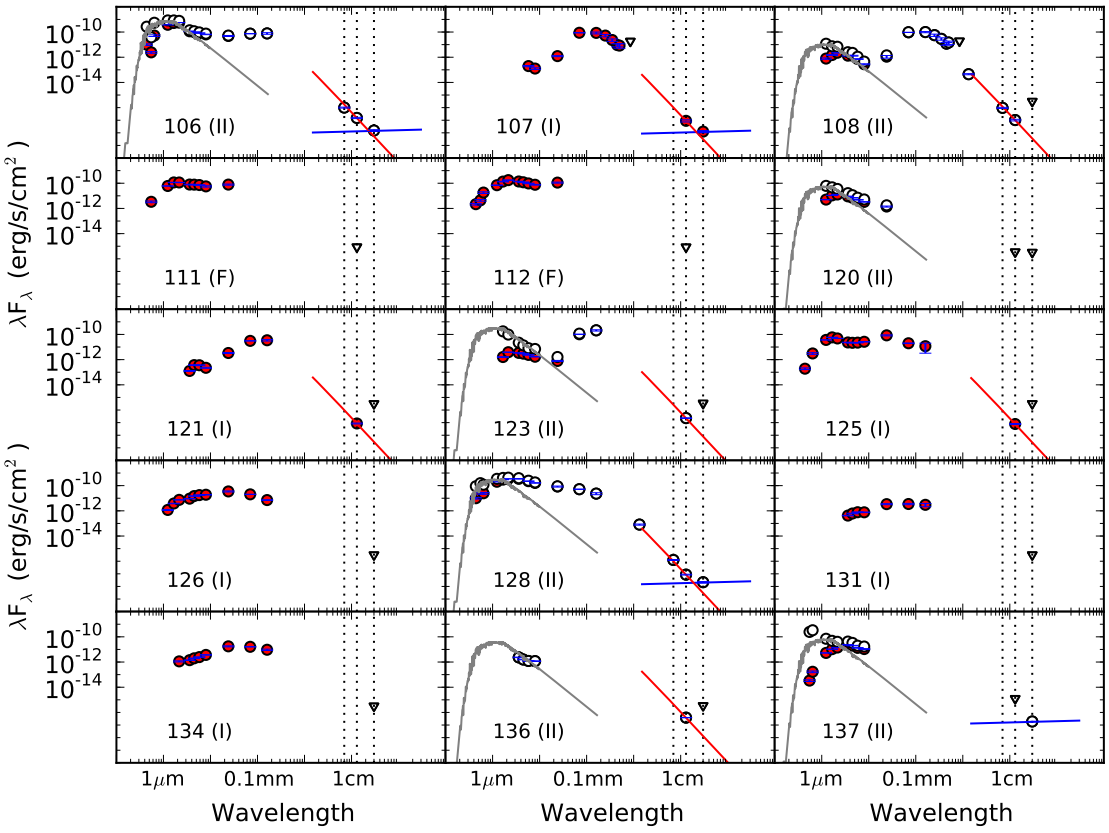

Figure 4.7 *continued*

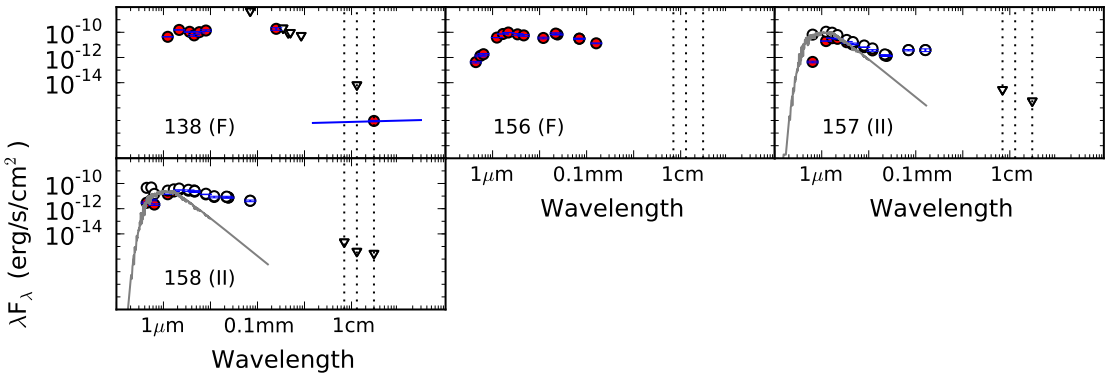

Figure 4.7 *continued*

4.4 Conclusions and Summary

In this work, we observe YSOs at 0.7 cm, 1.3 cm, and 3 cm to measure the dust thermal emission and characterize the cm-grain populations of the disks and their implications for planet formation potential in Auriga-Cal.

Observations at 3 cm are used to measure the free-free emission from ionization by young stars, as it is expected to dominate over thermal emission from dust at wavelengths longer than 2 cm. The 3 cm flux is extrapolated to 1.3 cm and 0.7 cm to determine the contribution of free-free emission to the total flux observed at these wavelengths. We find the contamination of free-free emission for disks with detections at both 1.3 cm and 3 cm to range from 15% to 71% with the faintest disks being the most susceptible to contamination.

We present the first mass distribution measured at cm wavelengths from the 1.3 cm fluxes and find it to have a similar shape to mass distributions measured for other clouds, although extending to slightly higher masses. This higher range implies that more mass may be locked up in cm-sized grains than expected should disks in Auriga-Cal have a similar mm disk mass distribution as other clouds, however, this has not been measured. A comparison of the cm mass distribution and the mm mass distribution would elucidate how mass is distributed between cm-sized and mm-sized pebbles.

We directly measure $\alpha_{\rm cm}$ for a subset of Class II disks. Of the five disks with detections at both 0.7 cm and 1.3 cm, three have $\alpha_{\rm cm}$ of 2–3, similar to that measured for individual disks by the Disks@EVLA group. The other two disks have very flat $\alpha_{\rm cm}$ of 0.3-0.9, more similar to what is expected for free-free emission. These should be investigated more carefully to verify the shallow slope and determine whether or not it is due to free-free emission.

The results here suggest that the planet formation potential in Auriga-Cal is similar to that for disks in other cloud environments. The detection of disks at cm wavelengths implies the presence of cm-sized grains, the building blocks for planet formation. There is no indication that the grain growth is inhibited in these disks either by the environment of the early B-star or by the bulk material in the cloud. The process responsible for the difference in how high density material is assembled in the cloud for star formation does not have an effect at the size scales of YSOs.

To confirm this the similarity of disks in Auriga-Cal to those in other clouds requires a comparison of the mm emission from disks in Auriga-Cal to disk populations that are similarly studied in other clouds. Such a study requires interferometric observations given the farther distance of Auriga-Cal compared to other Gould Belt clouds. Spatial filtering is necessary due to the younger age and therefore confusion with large scale emission from the cloud itself. As more protoplanetary disks are studied in the cm wavelength regime (made possible by the recent upgrades and expansions to the VLA) and more results come

out from other VLA disk surveys (such as Disks@EVLA and surveys of edge-on disks), we will be able to consider the properties of disks in Auriga-Cal in the context of other disk populations.

Chapter 5

Conclusions

This thesis employed a multiwavelength approach to study young stellar objects and their circumstellar disk properties to investigate the star and planet formation potential in the Auriga-Cal molecular cloud. Auriga-Cal is a stark demonstration of how the total mass of the molecular cloud is not an indicator of the star formation within it. In comparison to the Orion A molecular cloud, which is at a similar distance, the two clouds have a similar morphology, size, and total mass. The star formation in each cloud, however, is remarkably different due to the fraction of material concentrated at high column density with Auriga-Cal having 10× less mass at high column density.

When these thesis projects began, very little was known about Auriga-Cal as it had been only just identified as one contiguous cloud by Lada et al. (2009). It is important to note that the work presented here comprises the bulk of analysis on the YSO population in this cloud. This investigation includes the identification and characterization of the YSO population at infrared wavelengths to ascertain the state of ongoing star formation in the cloud; a consideration of the YSOs visible at submm wavelengths and measurement of their temperatures and circumstellar masses; and a first examination of the protoplanetary disks to assess the planet formation potential in the cloud environment.

The infrared census of YSOs with *Spitzer* quantifies that Auriga-Cal is forming 16–20× fewer stars than Orion A. We identify the grouping of YSOs in the cloud and determine that its southern end contains over 75% of its ongoing star formation. We classify YSOs by their SEDs and find a high fraction of Class I/Fs relative to all YSOs in comparison to other nearby Gould Belt clouds. This result supports the idea that Auriga-Cal is relatively young compared to these other clouds, given the short lifetime of the physical stage associated with this SED class.

The submm census of YSOs with the JCMT (which is sensitive to younger, earlier Class YSOs) reveals that the low number of star-forming objects in Auriga-Cal relative to Orion

A, first measured with *Spitzer* observations, extends to younger objects sampled in the submm. This similarity suggests that the relative star formation rate in the two clouds has not changed in their recent history - that is, there is not a significant population of YSOs in the earliest stages of star formation in Auriga-Cal to help bridge the gap in number of YSOs produced in Auriga-Cal relative to Orion A. We also measure the mass distribution of protostars and candidate protostars in Auriga-Cal, as the submm observations are sensitive to the optically thin dust emission and therefore total mass, incorporating the *Herschel* observations by Harvey et al. (2013).

Despite the JCMT's impressive 15 m dish size and therefore increased resolution compared to *Herschel*, its measurements are still limited by the spatial resolution of it being a single-dish observatory. Auriga-Cal and Orion A are the most distant clouds in the JCMT Gould Belt Survey ($\sim$450 pc) and this distance makes the study of YSOs more difficult in two predominant ways. First, since Auriga-Cal is one of the furthest clouds in a flux-limited survey, we are sensitive to the brightest material in the cloud whereas the more nearby clouds surveyed are more complete to material with fainter absolute flux levels. For the circumstellar mass distribution, this restriction means we are limited to the YSOs that host the brightest, i.e., the greatest amount of circumstellar material. This restriction also means that most of the protostars we detected are early Class protostars (i.e., up to Class I) with only a few Class II objects and no Class III objects. Secondly, the further distance means that more physical volume is included within the same angular beam size. Consequently, it is more difficult to isolate YSOs from intervening or neighbouring cloud material. These two factors are further complicated in conjunction, as younger YSOs tend to be more coincident with natal filaments of the cloud than are older objects, such as Class IIs and IIIs. Therefore, our sensitivity to only the youngest objects is further limited by their coincidence with the brightest "background" cloud emission.

The difficulty in probing YSOs at $\sim$500 pc demonstrates the importance of interferometric observations of the YSOs in Auriga-Cal. The spatial resolution attainable with interferometry is required to isolate YSOs from other nearby YSOs as well as larger-scale cloud emission. Therefore, to study the circumstellar disks themselves, we used the VLA interferometer.

The microwave observations with the VLA were taken as a first look analysis of the circumstellar disk population in Auriga-Cal to determine whether or not it appeared similar to young disks in other star-forming regions. Specifically, we sought to determine the amount of material available for planet formation by means of a survey targeted at the thermal dust emission at cm wavelengths. Such observations are sensitive to dust "pebbles" with $\sim$ cm sizes.

Auriga-Cal presents a nearby new archetype filamentary GMC, and therefore it repre-

sents an opportunity to learn *why* the Orion A cloud has been compressed to such high densities and produced such bounty whereas Auriga-Cal has not. Studying Auriga-Cal as an archetype of this process is particularly important since clouds like it further away would not necessarily be identifiable as GMCs, as they are nominally distinguishable by their rich star formation. Future work to investigate the root causes of these differences will require targeting of the cloud material itself to study the filament of Auriga-Cal and determine global conditions in the cloud and/or external factors compared to Orion A.

Outstanding questions remain regarding the disk population in Auriga-Cal, namely what is its complete census of disk masses at mm wavelengths? This would be directly comparable to mm censuses of other clouds, specifically Taurus, Ophiuchus, and Orion A. The JCMT observations presented here introduce a first look in the submm/mm regimes but we were severely limited by resolution in isolating disks given Auriga-Cal's distance. Such a census requires interferometry. A mm census of the disks including observations in proximity to and distanced from LkHα 101 would also examine whether or not this B-star erodes disks, and therefore explore the limits of UV environments that can truncate disks, as observed in the ONC. The outer regions of disks are probed in this wavelength regime given that it is the mm dust grains that are distributed to large radii, not the cm sized grains. The comparison of mm measurements of disks to the cm measurements presented here would allow consideration of relative pile up or dearth of grains in Auriga-Cal's disk population. Currently, there are several examples of a few individual disks showcasing both of the situations. The next step is to consider large samples of disks at various stages to learn about the evolution of dust growth in disks and explore how quickly large grains develop.

Bibliography

Alcalá, J. M. et al. 2008, Astrophysical Journal, 676, 427

Alexander, R. D., Clarke, C. J., & Pringle, J. E. 2006, Monthly Notices of the RAS, 369, 229

Allen, L. E. et al. 2004, Astrophysical Journal, Supplement Series, 154, 363

André, P. 1994, Spectral Classification of Embedded Stars, ed. Garguad, M., Amils, R., Cernicharo Quintanilla, J., Cleaves II, H. J., Irvine, W. M., Pinti, D. L., & Viso, M. (Springer Berlin Heidelberg)

André, P. et al. 2010, Astronomy and Astrophysics, 518, L102

Andrews, S. M. & Williams, J. P. 2005, Astrophysical Journal, 631, 1134

— 2007, Astrophysical Journal, 671, 1800

Andrews, S. M., Wilner, D. J., Espaillat, C., Hughes, A. M., Dullemond, C. P., McClure, M. K., Qi, C., & Brown, J. M. 2011, Astrophysical Journal, 732, 42

Artymowicz, P. & Lubow, S. H. 1994, Astrophysical Journal, 421, 651

Banzatti, A., Testi, L., Isella, A., Natta, A., Neri, R., & Wilner, D. J. 2011, Astronomy and Astrophysics, 525, A12

Beckwith, S. V. W. & Sargent, A. I. 1991, Astrophysical Journal, 381, 250

Beckwith, S. V. W., Sargent, A. I., Chini, R. S., & Guesten, R. 1990, Astronomical Journal, 99, 924

Berry, D. S., Reinhold, K., Jenness, T., & Economou, F. 2007, in Astronomical Society of the Pacific Conference Series, Vol. 376, Astronomical Data Analysis Software and Systems XVI, ed. R. A. Shaw, F. Hill, & D. J. Bell, 425

Broekhoven-Fiene, H. et al. 2014, Astrophysical Journal, 786, 37

Brown, J. M. et al. 2007, Astrophysical Journal, Letters to the Editor, 664, L107

Buckle, J. V. et al. 2015, Monthly Notices of the RAS, 449, 2472

Calvet, N., D'Alessio, P., Hartmann, L., Wilner, D., Walsh, A., & Sitko, M. 2002, Astrophysical Journal, 568, 1008

Cartwright, A. & Whitworth, A. P. 2004, Monthly Notices of the RAS, 348, 589

Chapin, E. L., Berry, D. S., Gibb, A. G., Jenness, T., Scott, D., Tilanus, R. P. J., Economou, F., & Holland, W. S. 2013, Monthly Notices of the RAS, 430, 2545

Cieza, L. et al. 2007, Astrophysical Journal, 667, 308

Cieza, L. A. et al. 2010, Astrophysical Journal, 712, 925

Cieza, L. A., Schreiber, M. R., Romero, G. A., Williams, J. P., Rebassa-Mansergas, A., & Merín, B. 2012, Astrophysical Journal, 750, 157

Cutri, R. M. et al. 2003, 2MASS All Sky Catalog of point sources., ed. Cutri, R. M., Skrutskie, M. F., van Dyk, S., Beichman, C. A., Carpenter, J. M., Chester, T., Cambresy, L., Evans, T., Fowler, J., Gizis, J., Howard, E., Huchra, J., Jarrett, T., Kopan, E. L., Kirkpatrick, J. D., Light, R. M., Marsh, K. A., McCallon, H., Schneider, S., Stiening, R., Sykes, M., Weinberg, M., Wheaton, W. A., Wheelock, S., & Zacarias, N.

D'Alessio, P., Calvet, N., Hartmann, L., Lizano, S., & Cantó, J. 1999, Astrophysical Journal, 527, 893

Dempsey, J. T. et al. 2013, Monthly Notices of the RAS, 430, 2534

Dobashi, K., Uehara, H., Kandori, R., Sakurai, T., Kaiden, M., Umemoto, T., & Sato, F. 2005, Publications of the ASJ, 57, 1

Drabek, E. et al. 2012, Monthly Notices of the RAS, 426, 23

Draine, B. T. 2006, Astrophysical Journal, 636, 1114

Dullemond, C. P., Hollenbach, D., Kamp, I., & D'Alessio, P. 2007, Protostars and Planets V, 555

Dunham, M. M. et al. 2013, Astronomical Journal, 145, 94

Evans, N. J. et al. 2009, Astrophysical Journal, Supplement Series, 181, 321

Evans, II, N. J. et al. 2003, Publications of the ASP, 115, 965

Evans, II, N. J. et al. 2007

Fazio, G. G. et al. 2004, Astrophysical Journal, Supplement Series, 154, 10

Felli, M., Taylor, G. B., Catarzi, M., Churchwell, E., & Kurtz, S. 1993, Astronomy and Astrophysics, Supplement Series, 101, 127

Friesen, R. K., Johnstone, D., Naylor, D. A., & Davis, G. R. 2005, Monthly Notices of the RAS, 361, 460

Goldsmith, P. F., Bergin, E. A., & Lis, D. C. 1997, Astrophysical Journal, 491, 615

Greene, T. P., Wilking, B. A., Andre, P., Young, E. T., & Lada, C. J. 1994, Astrophysical Journal, 434, 614

Guilloteau, S., Dutrey, A., Piétu, V., & Boehler, Y. 2011, Astronomy and Astrophysics, 529, A105

Gutermuth, R. A., Megeath, S. T., Myers, P. C., Allen, L. E., Pipher, J. L., & Fazio, G. G. 2009, Astrophysical Journal, Supplement Series, 184, 18

Harvey, P., Merín, B., Huard, T. L., Rebull, L. M., Chapman, N., Evans, II, N. J., & Myers, P. C. 2007, Astrophysical Journal, 663, 1149

Harvey, P. M. et al. 2006, Astrophysical Journal, 644, 307

— 2013, Astrophysical Journal, 764, 133

— 2008, Astrophysical Journal, 680, 495

Herbig, G. H., Andrews, S. M., & Dahm, S. E. 2004, Astronomical Journal, 128, 1233

Holland, W. S. et al. 2013, Monthly Notices of the RAS, 430, 2513

Hughes, A. M. et al. 2010, Astronomical Journal, 140, 887

Hunter, T. R. 1998, Publications of the ASP, 110, 634

Isella, A. 2006, PhD thesis, Universita degli Studi di Milano

Jenness, T., Currie, M. J., Tilanus, R. P. J., Cavanagh, B., Berry, D. S., Leech, J., & Rizzi, L. 2015, Monthly Notices of the RAS, 453, 73

Jørgensen, J. K. et al. 2006, Astrophysical Journal, 645, 1246

Kackley, R., Scott, D., Chapin, E., & Friberg, P. 2010, in Society of Photo-Optical Instrumentation Engineers (SPIE) Conference Series, Vol. 7740, Society of Photo-Optical Instrumentation Engineers (SPIE) Conference Series, 1

Kenyon, S. J. & Hartmann, L. 1987, Astrophysical Journal, 323, 714

Kirk, J. M. et al. 2009, Astrophysical Journal, Supplement Series, 185, 198

Koenig, X. P., Leisawitz, D. T., Benford, D. J., Rebull, L. M., Padgett, D. L., & Assef, R. J. 2012, Astrophysical Journal, 744, 130

Lada, C. J. 1987, in IAU Symposium, Vol. 115, Star Forming Regions, ed. M. Peimbert & J. Jugaku, 1–17

Lada, C. J., Lombardi, M., & Alves, J. F. 2009, Astrophysical Journal, 703, 52

Lynds, B. T. 1962, Astrophysical Journal, Supplement Series, 7, 1

Mairs, S. et al. 2015, Monthly Notices of the RAS, 454, 2557

Mann, R. K., Andrews, S. M., Eisner, J. A., Williams, J. P., Meyer, M. R., Di Francesco, J., Carpenter, J. M., & Johnstone, D. 2015, Astrophysical Journal, 802, 77

Mann, R. K. et al. 2014, Astrophysical Journal, 784, 82

Mann, R. K. & Williams, J. P. 2009a, Astrophysical Journal, Letters to the Editor, 699, L55

— 2009b, Astrophysical Journal, Letters to the Editor, 694, L36

— 2010, Astrophysical Journal, 725, 430

Masiunas, L. C., Gutermuth, R. A., Pipher, J. L., Megeath, S. T., Myers, P. C., Allen, L. E., Kirk, H. M., & Fazio, G. G. 2012, Astrophysical Journal, 752, 127

Megeath, S. T. et al. 2012, Astronomical Journal, 144, 192

Melis, C. et al. 2011, Astrophysical Journal, Letters to the Editor, 739, L7

Men'shchikov, A., André, P., Didelon, P., Motte, F., Hennemann, M., & Schneider, N. 2012, Astronomy and Astrophysics, 542, A81

Merín, B. et al. 2008, Astrophysical Journal, Supplement Series, 177, 551

Myers, P. C. & Ladd, E. F. 1993, Astrophysical Journal, Letters to the Editor, 413, L47

Natta, A., Testi, L., Neri, R., Shepherd, D. S., & Wilner, D. J. 2004, Astronomy and Astrophysics, 416, 179

Oliveira, I. et al. 2009, Astrophysical Journal, 691, 672

Pascucci, I., Gorti, U., & Hollenbach, D. 2012, Astrophysical Journal, Letters to the Editor, 751, L42

Pattle, K. et al. 2015, Monthly Notices of the RAS, 450, 1094

Pérez, L. M. et al. 2012, Astrophysical Journal, Letters to the Editor, 760, L17

— 2015, Astrophysical Journal, 813, 41

Peterson, D. E. et al. 2011, Astrophysical Journal, Supplement Series, 194, 43

Pollack, J. B., Hubickyj, O., Bodenheimer, P., Lissauer, J. J., Podolak, M., & Greenzweig, Y. 1996, Icarus, 124, 62

Rebull, L. M. et al. 2007, Astrophysical Journal, Supplement Series, 171, 447

Rieke, G. H. et al. 2004, Astrophysical Journal, Supplement Series, 154, 25

Robitaille, T. & Bressert, E. 2012, APLpy: Astronomical Plotting Library in Python, Astrophysics Source Code Library

Robitaille, T. P., Whitney, B. A., Indebetouw, R., Wood, K., & Denzmore, P. 2006, Astrophysical Journal, Supplement Series, 167, 256

Rodmann, J., Henning, T., Chandler, C. J., Mundy, L. G., & Wilner, D. J. 2006, Astronomy and Astrophysics, 446, 211

Sadavoy, S. I. et al. 2014, Astrophysical Journal, Letters to the Editor, 787, L18

— 2013, Astrophysical Journal, 767, 126

Shu, F. H., Adams, F. C., & Lizano, S. 1987, Annual Review of Astronomy and Astrophysics, 25, 23

Sicilia-Aguilar, A., Henning, T., & Hartmann, L. W. 2010, Astrophysical Journal, 710, 597

Strom, K. M., Strom, S. E., Edwards, S., Cabrit, S., & Skrutskie, M. F. 1989, Astronomical Journal, 97, 1451

Surace, J. A. et al. 2004, VizieR Online Data Catalog, 2255, 0

Tazzari, M. et al. 2016, Astronomy and Astrophysics, 588, A53

Testi, L., Natta, A., Shepherd, D. S., & Wilner, D. J. 2003, Astronomy and Astrophysics, 403, 323

Ungerechts, H. & Thaddeus, P. 1987, Astrophysical Journal, Supplement Series, 63, 645

Ward-Thompson, D. et al. 2007, Publications of the ASP, 119, 855

Weidenschilling, S. J. 1977, Astrophysics and Space Science, 51, 153

Weingartner, J. C. & Draine, B. T. 2001, Astrophysical Journal, 548, 296

Werner, M. W. et al. 2004, Astrophysical Journal, Supplement Series, 154, 1

Williams, J. P. & Best, W. M. J. 2014, Astrophysical Journal, 788, 59

Williams, J. P. & Cieza, L. A. 2011, Annual Review of Astronomy and Astrophysics, 49, 67

Wolk, S. J., Winston, E., Bourke, T. L., Gutermuth, R., Megeath, S. T., Spitzbart, B. D., & Osten, R. 2010, Astrophysical Journal, 715, 671

Wright, E. L. et al. 2010, Astronomical Journal, 140, 1868

Young, C. H., Shirley, Y. L., Evans, II, N. J., & Rawlings, J. M. C. 2003, Astrophysical Journal, Supplement Series, 145, 111

Young, K. E. et al. 2005, Astrophysical Journal, 628, 283

Zapata, L. A., Rodríguez, L. F., Kurtz, S. E., & O'Dell, C. R. 2004, Astronomical Journal, 127, 2252